Measurement and applications of singlet order lifetime through the use of pulsed-field gradients

Giulia Melchiorre

2023

Graduate School of Chemistry
University of Southampton
orcid.org/0009-0004-6544-2448

University of Southampton

Abstract

In this thesis, two fundamental concepts of nuclear magnetic resonance (NMR) were studied and combined in order to develop new solutions to practical problems. These concepts were: the use of pulsed magnetic field gradients for imaging and diffusion measurements, and the relaxation properties of a spin system. Chapter 2 describes how three-dimensional, diffusion-sensitising gradients were used in NMR experiments carried out on a system where long-lived singlet state was populated, allowing relaxation decay constants of the order of minutes to be achieved; this resulted in a new pulse sequence dubbed SADTI (Singlet-Assisted Diffusion Tensor Imaging) used in experiments where the structural characterization of model systems was possible by tracking diffusion of singlet-bearing molecules in 3D for a time that is currently not achievable using routine diffusion NMR and magnetic resonance imaging (MRI) techniques. Chapter 3 presents the successful application of selective magnetic field gradients to reduce the duration of singlet order decay constant measurement, from 2.5 hours to less than 8 minutes. Finally, chapter 4 describes the first stages of the application of SADTI pulse sequence to real samples: these consisted of human tissue cultivated on porous polycaprolactone scaffolds; the goal of this study was to verify if SADTI can help in monitoring cell growth on artificial supports, by detecting changes in the diffusion

pattern of a molecular probe of choice in which the specimen is immersed. These changes would reflect structural variations occurred within the cultivated scaffold, due to the cells infiltrating the pores and thus modifying the degree of restriction molecular diffusion is subject to. In order to provide the theoretical foundations to these studies, the concept and use of pulsed gradients in imaging and diffusion NMR, the description and measurement of molecular diffusion in free and restricted conditions, and the basic theory behind relaxation properties of the spin systems used, are presented in Chapter 1.

University of Southampton

Declaration of authorship

I declare that this thesis and the work presented in it is my own and has been generated by me as the result of my own original research.

I confirm that:

1. This work was done wholly or mainly while in candidature for a research degree at this University;

2. Where any part of this thesis has previously been submitted for a degree or any other qualification at this University or any other institution, this has been clearly stated;

3. Where I have consulted the published work of others, this is always clearly attributed;

4. Where I have quoted from the work of others, the source is always given. With the exception of such quotations, this thesis is entirely my own work;

5. I have acknowledged all main sources of help;

6. Where the thesis is based on work done by myself jointly with others, I have made clear exactly what was done by others and what I have contributed myself;

7. Parts of this work have been published as: *Phys. Chem. Chem. Phys., 2021, 23, 9851.*

University of Southampton

Acknowledgements

I wish to express my deep gratitude to the University of Southampton for offering me the opportunity to complete this research. A special thanks to my supervisor Dr. Giuseppe Pileio for sharing his knowledge and stimulating me with discussions, informal chats and some very constructive disagreements; a big thank you to Prof. Marco Geppi from the University of Pisa, for introducing me to NMR and for allowing me to go abroad and learn some more; thanks to all the members of the research group that I met through these four years: Aliki Moysiadi, Monique Tourell, Francesco Giustiniano, Andy Hall, Topaz Cartlidge and Thomas Robertson for the technical support and for creating such a friendly and relaxed work environment; Sundeep Ratore and Ciara Nelder for teaching me so much on how to communicate my knowledge, and anyone in the academic environment who had a nice word for me when I was so insecure about it. A special thanks to Alan Glass for patiently supporting me during the construction of the degassing equipment I used to prepare my samples.

I also wish to express my profound gratitude to Mrs Kate Parry, Dr. Karen Marshall Prof. Nick Evans and Prof. John Dawson for the training and the feedback received at the Institute of Developmental Sciences (University of Southampton) where they very generously shared their knowledge in microbiology and tissue cultivation.

Finally, I wish to thank everyone who supported me in this difficult journey through their friendship: Maria, Ludovica, Sheila, Victoria, Sofia, Annachiara and all my friends in Southampton and in Italy. Thanks to my family. Thanks to my sister Francesca. Thanks to Ian. Thanks to Letizia and the work we have done.

University of Southampton

Table of Contents

Introduction 9

1. Theoretical background 14

1.1. Basics of NMR 14

1.2. An ensemble of ½-spins pairs 16

1.3. Pulsed magnetic field gradients 24

1.3.1. Magnetic field gradients to study molecular diffusion 27

1.3.2. Magnetic field gradients for selective excitation 30

1.4. Molecular diffusion in NMR 36

1.4.1. What is diffusion 36

1.4.2. Anisotropy of diffusion 44

1.4.2.1. The diffusion tensor 44

1.4.2.2. The diffusion regimes 49

1.4.2.3. Anomalous diffusion 53

1.4.3. Diffusion NMR techniques 55

1.4.3.1. Measurement of the diffusion coefficient: PGSE and PGSTE 58

1.4.3.2. Measurement of the diffusion tensor: DTI technique 61

1.5. Long-lived singlet spin order 66

1.5.1. Relaxation of transverse and longitudinal magnetisation 66

1.5.2. Relaxation of singlet order 74

1.5.3. Singlet state population 77

1.5.4. Ts measurement 81

2. Diffusion tensor measurement on model systems 82

2.1. Material and methods 84

2.1.1. Plastic inserts 84

2.1.2. Molecular probe 85

2.1.3. Sample assembling and preparation 86

2.2. Experiments 88

2.2.1. T_1 measurement 88
2.2.2. Singlet-assisted DTI experiments 88
2.2.2.1. The diff-M2S2M pulse sequence 88
2.2.2.2. Data acquisition 90
2.2.2.3. Data processing 92
2.2.2.4. Error calculation 94
2.2.2.5. Worked example 95
2.3. Results 97
2.3.1. Relaxation times 97
2.3.2. Diffusion tensor calculation 100
2.4. Conclusions 102
3. Single-scan *Ts* measurement 104
3.1. Material and methods 107
3.1.1. Samples 107
3.1.2. Shaped pulse optimisation 109
3.1.3. Pulse sequence 112
3.2. Results and discussion 120
3.3 Conclusions 133
4. Towards SADTI application to tissue engineering 134
4.1 Materials and Method 144
4.1.1. Molecular probe 144
4.1.2. 3D structures 144
4.1.3. Tissue culture 146
4.1.3.1. 2D cell culture 147
4.1.3.2. 3D culture on scaffolds 149
4.1.4. Sample assembly and preparation 152
4.1.4.1. Sample holder 152
4.1.4.2. Solution degassing and transfer to sample holder 155
4.1.5. Experiments 159
4.2. Results and discussion 160
4.2.1. Cell culture 160

4.2.2. Sample degassing 165
4.2.3. Diffusion tensor measurement on scaffolds 168
4.3 Conclusions 172
5. Conclusions 176
6. Bibliography 181

University of Southampton

Introduction

This work describes the outcomes of a study aimed at combining long-lived singlet spin order preparation with diffusion NMR and MRI procedures (such as diffusion tensor imaging, DTI) to infer structural properties of samples currently out of the scope of most traditional imaging techniques. Singlet order has been increasingly investigated in the past two decades as a convenient way to store information for a time much longer than what longitudinal magnetisation allows to [1,2,3]. Previously, a pulse sequence was developed in the present group to populate singlet state for a system of coupled protons in nearly-equivalent conditions [4]; later on, the same pulse sequence was combined with diffusion gradients, allowing to probe diffusion for a time up to 5 minutes in a technique dubbed SAD NMR (singlet-assisted diffusion NMR) [5]). The goal of the present study was to expand the scope of SAD NMR by applying the same pulse sequence through a different procedure where the diffusion gradient is applied along multiple directions to probe molecular displacement in three dimensions, and DTI data processing is used. The first two chapters of this work describe the development of such methodology (dubbed SADTI, singlet-assisted diffusion tensor imaging) and its application to 3D structures to verify that it is possible to infer structural features through

measurements of diffusion anisotropy and the calculation of the diffusion tensor. Model systems of known internal architecture were used to optimise the experimental procedure and the results are presented in Chapter 2; the methodology was then applied to polycaprolactone (PCL) scaffolds, manufactured to support the growth of live cells in the ground-breaking field of tissue regeneration. These were chosen as systems that would highly benefit from 3D non-invasive characterisation. Indeed, tissue engineering is currently challenged by the need of inspecting 3D cultures in a non-destructive fashion, in order to monitor the stages of tissue development [6]. The decision of applying SADTI to these systems was justified by the fact that phenomena relevant to tissue engineering such as cell growth, cell migration, scaffold population and degradation, result in gradual change of the structural properties of the specimen; if the cell-populated scaffold is immersed in a solution of a selected molecular probe, these changes can be detected through the effect they have on the molecular diffusion patterns, and evaluated through diffusion anisotropy. In order to monitor the structural changes over time, the technique needs to provide a reliable characterisation of the scaffold in its initial conditions; therefore, if the scaffold's pore size is of the order of hundreds of micrometres, molecular diffusion needs to be probed for a time sufficient to explore such distance; the optimal pore-size for scaffolds intended for tissue regeneration has been

reported to be between 100 and $500\ \mu m$ [7] therefore making commonly used molecular probes such as water, unable to report on structural features at this scale; long-lived singlet order represents a valuable resource to track diffusion in three dimensions on such systems, because its longer lifetime translates into a longer distance along which molecules can be probed, as stated by the Einstein equation

$$d_{rms} = \sqrt{2\Delta D} \tag{1}$$

where d_{rms} is the root-mean-square displacement in metres, D is the self-diffusion coefficient (a scalar value that quantifies the diffusion of a molecule in a solution of the same species, $m^2 s^{-1}$) and Δ is the time interval (s).

Cell migration and proliferation on the scaffold result in changes of pore interconnectivity which will alter the shape and the size of the cavities in which singlet-bearing guest molecules can diffuse; if longer distances can be probed, such changes can be detected, as conditions for restricted motion can be created even in samples with porous size of hundreds of micrometres. The development of the procedure to carry out SADTI experiments on 3D cell cultures is described in Chapter 4. During this study, scaffolds made of biocompatible polycaprolactone (PCL) with cavities of $300\ \mu m$ cross section were purchased and seeded with human mesenchymal stem cells. Cells were fixed after 6 days and the specimen was

immersed in a solution of a chemical species designed to access singlet state; the solution was also previously degassed through an airtight setup designed and built in-house, to remove paramagnetic oxygen which would decrease singlet decay constant; diffusion tensor measurement was carried out to compare diffusion anisotropy in populated and un-populated scaffolds.

The powerful tool represented by magnetic field gradients was also exploited in the context of space-selective excitation pulses, for another application developed in the present work and described in Chapter 3: pulsed field gradients, shaped radio-frequency pulses and singlet order preparation were combined to validate a faster procedure for T_s measurement, which can take hours when a relaxation time of the order of hundreds of seconds is expected. The purpose was to verify that is possible to significantly reduce the duration of such measurement by substituting the list of separated acquisitions (each one with a different variable delay, analogously to what is done when measuring T_1), with a series of subsequent excitations on different portions of the sample, followed by one single acquisition. As will be thoroughly discussed in Chapter 3, the spectrum resulting from this procedure displays a profile of the sample where the intensity is a function of the position rather than the chemical shift. Each slice reports on a different fraction of the sample, were signal was allowed to decay for a different time depending when, during the experiment,

that slice was selectively excited. In this context, the effect of molecular motion caused by thermal convection was also investigated; in fact, this showed to interfere with the separation of subsequent slices, since molecules appeared to cross the sample longitudinally therefore contributing to the signal of a different slice, far from where they were originally excited. This reflected on the resolution of the spectrum and the practical solution adopted to bypass the issue are described.

The theoretical foundation for diffusion NMR and DTI, long-lived singlet spin order and the use of magnetic field gradients combined with selective radio-frequency pulses is provided in Chapter 1.

University of Southampton

1. Theoretical background

1.1. Basics of NMR

NMR is based on the interaction between a radio frequency pulse and a system consisting of an ensemble of spins placed in a static magnetic field. In a simplified but effective description of this system, the spins of nuclei with gyromagnetic ratio γ are said to *precess* around the direction of the static magnetic field B_0, with angular frequency ω_0 given by

$$\omega_0 = -\gamma B_0 \tag{2}$$

where ω_0 is known as Larmor frequency.

The energy of each single spin (considered as isolated from the others) is described by the Zeeman Hamiltonian, $\hat{H}_Z$

$$\hat{H}_Z = \omega_0 \hat{I}_z \tag{3}$$

where $\hat{I}_z$ is the z-component of the angular momentum operator. The precession frequency of a nucleus determines its chemical-shift, i.e. the position in the NMR spectrum where a signal appears and from which that nucleus can be identified.

The angular momentum resulting from the ensemble of precessing spins is represented as a vector called Magnetisation (M). If a reference frame is considered (LAB frame) with its z-axis parallel to the static magnetic field B_0, the perpendicular x-y plane can be identified as the plane where the RF pulses are sent and where the NMR signal is collected through the detector. Before any RF pulse is applied, the resultant magnetisation is aligned with the magnetic field along the z-axis and identified with the term longitudinal magnetisation M_z; a RF pulse acts on each single spin and ultimately on their resultant M such that the magnetisation itself precesses around the direction of the pulse; a 90-degree RF pulse along the y-axis causes M to precess around this direction, resulting on the x-y plane after a 90-degree flip (transverse magnetisation M_{xy}). Transverse magnetisation's free precession on the x-y plane induces a current that can be acquired as NMR signal by the detector.

The angle formed by each spin with the x-axis is the spin phase ϕ. When the spins experience the same phase, they are said to be polarised along a certain direction; this makes the magnetisation, and therefore the NMR signal, reach its maximum to then gradually decay over time as the spins lose phase coherence. Figure 2.1 shows a schematic representation of these events, where each spin is represented as a vector and the resultant magnetisation is tilted on the x-y plane by a RF pulse and detected on the same plane while losing intensity as the spins lose phase coherence. This is at

the origin of the characteristic decay in time of any NMR signal (FID: free induction decay). The reasons of this decay, its implications and features are at the core of the present work and will be the subject of the next paragraphs.

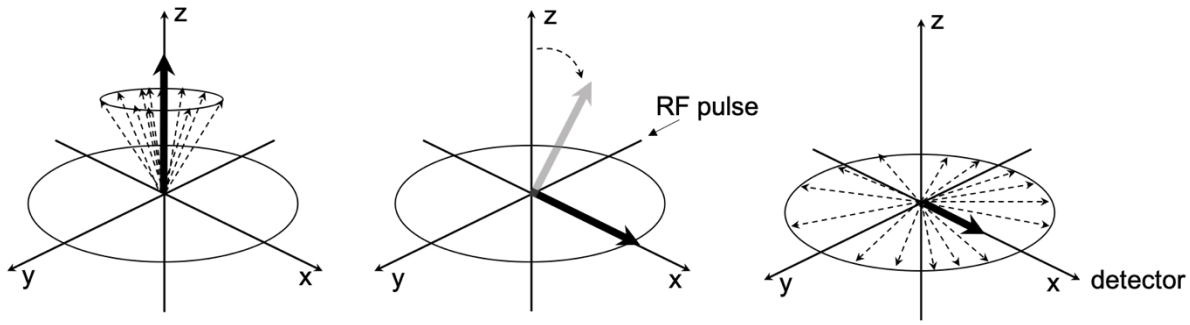

Figure 2.1 A simple 90-degree pulse in an NMR experiment. The resultant of all the spins in the ensemble is represented as a vector aligned with the external magnetic field (left); a 90-degree pulse along the y-axis of the laboratory frame brings the resultant along the x-axis where a detector is placed (centre); the resultant magnetisation induces a current (NMR signal) while spins lose coherence (right).

1.2. An ensemble of ½-spins pairs

If a system of spin-1/2 pairs is considered instead, the energy of each pair is also described by a Zeeman Hamiltonian, which in addition to the interaction of each spin with the static magnetic field B_0, also includes the reciprocal effect the nuclei have on one another. In solution, this effect is mediated by the electrons holding the molecule together. These are weakly magnetised by the protons and generate a local

magnetic field through which each nucleus in the pair can sense the presence of the other. This indirect interaction is called J-coupling and results in the spectral line of each nucleus of the pair to split in two signals, whose distance in Hertz quantifies the interaction and is referred to as the J-coupling constant of the pair.

Both J-coupling and Zeeman interaction are time-independent and so-called *coherent* interactions, as they are both experienced by each member of the ensemble to the same extent regardless of their position in the sample.

As stated in equation (2), if the two nuclei in the pair experience a different magnetic field, their precession frequency is different. In isotropic liquids, when the difference in chemical shift experienced by two spins is much higher than their J-coupling constant, they are said to form a pair of weakly-coupled spins [8]. The Hamiltonian describing the energy of this system is

$$\widehat{H}_0 = \omega_1^0 \hat{I}_{1z} + \omega_2^0 \hat{I}_{2z} + 2\pi J_{12} \hat{I}_{1z} \hat{I}_{2z} \quad (4)$$

where the indexes 1 and 2 refer to each spin in the pair, and J_{12} is their coupling constant. The eigenfunctions of this Hamiltonian form the basis that can be used to write any possible state $|\psi\rangle$ of this system. In the case of a pair of weakly-coupled spins, the eigenfunctions of the Hamiltonian are the so-called Zeeman product

states: $|\alpha\alpha\rangle$, $|\alpha\beta\rangle$, $|\beta\beta\rangle$, $|\beta\alpha\rangle$, where α and β are the two possible eigenstates for a single isolated spin-1/2.

It can therefore be written

$$|\psi\rangle_{pair} = c_{\alpha\alpha}|\alpha\alpha\rangle + c_{\alpha\beta}|\alpha\beta\rangle + c_{\beta\alpha}|\beta\alpha\rangle + c_{\beta\beta}|\beta\beta\rangle \quad (5)$$

where $c_{\alpha\alpha}, c_{\alpha\beta}, c_{\beta\alpha}, c_{\beta\beta}$ are numerical coefficients that weigh the contribution of each eigenfunction to the state $|\psi\rangle_{pair}$.

Although each pair of the ensemble exists in a superposition of these four states, it is common to refer to each state as *populated* by the members of the ensemble. In fact, the term "population" refers to a specific coefficient in the expansion of a mathematical tool called density operator $\hat{\rho}$, used to describe the dynamics of an ensemble. The density operator is defined as follows:

$$\hat{\rho} = \overline{|\psi\rangle\langle\psi|} \quad (6)$$

where $|\psi\rangle$ and $\langle\psi|$ are the ket and the bra for the state of a single element of the ensemble, and the product is then averaged over the entire ensemble. In the case of an ensemble of spin-1/2 pairs, it is $|\psi\rangle = |\psi\rangle_{pair}$ and its ket is defined as equation (5). If $\hat{\rho}$ for this ensemble is calculated as stated in equation (6), a linear combination of 16 elements results:

$$\hat{\rho} = \overline{|\psi\rangle\langle\psi|} = \overline{c_{\alpha\alpha}c_{\alpha\alpha}^*}\ |\alpha\alpha\rangle\langle\alpha\alpha| + \cdots + \overline{c_{\beta\alpha}c_{\alpha\beta}^*}\ |\beta\alpha\rangle\langle\alpha\beta| \quad (7)$$

The term $|\alpha\alpha\rangle\langle\alpha\alpha|$ is the *population operator* for the state $|\alpha\alpha\rangle$; its coefficient, $\overline{c_{\alpha\alpha}c_{\alpha\alpha}^*}$ quantifies the population of the state $|\alpha\alpha\rangle$. The same argument holds for the coefficients $\overline{c_{\alpha\beta}c_{\alpha\beta}^*}$, $\overline{c_{\beta\alpha}c_{\beta\alpha}^*}$ and $\overline{c_{\beta\beta}c_{\beta\beta}^*}$ which quantify the population of the states $|\alpha\beta\rangle$, $|\beta\alpha\rangle$ and $|\beta\beta\rangle$ respectively.

The density operator can also be expressed in its matrix form. In fact, the product $\overline{|\psi\rangle\langle\psi|}$ can also be carried out by noting that the ket $|\psi\rangle$ is uniquely identified by the vector of its linear coefficients in equation (5). Therefore, it is possible to write:

$$|\psi\rangle\langle\psi| = \begin{pmatrix} c_{\alpha\alpha} \\ c_{\alpha\beta} \\ c_{\beta\alpha} \\ c_{\beta\beta} \end{pmatrix} (c_{\alpha\alpha}{}^*, \quad c_{\alpha\beta}{}^*, \quad c_{\beta\alpha}{}^*, \quad c_{\beta\beta}{}^*) \quad (8)$$

where the product is a quadratic product and results in a matrix of 16 elements. If the average is considered, the density matrix can be finally obtained:

$$\hat{\rho} = \overline{|\psi\rangle\langle\psi|} = \begin{pmatrix} \overline{c_{\alpha\alpha}c_{\alpha\alpha}^*} & \overline{c_{\alpha\alpha}c_{\alpha\beta}^*} & \overline{c_{\alpha\alpha}c_{\beta\alpha}^*} & \overline{c_{\alpha\alpha}c_{\beta\beta}^*} \\ \overline{c_{\alpha\beta}c_{\alpha\alpha}^*} & \overline{c_{\alpha\beta}c_{\alpha\beta}^*} & \overline{c_{\alpha\beta}c_{\beta\alpha}^*} & \overline{c_{\alpha\beta}c_{\beta\beta}^*} \\ \overline{c_{\beta\alpha}c_{\alpha\alpha}^*} & \overline{c_{\beta\alpha}c_{\alpha\beta}^*} & \overline{c_{\beta\alpha}c_{\beta\alpha}^*} & \overline{c_{\beta\alpha}c_{\beta\beta}^*} \\ \overline{c_{\beta\beta}c_{\alpha\alpha}^*} & \overline{c_{\beta\beta}c_{\alpha\beta}^*} & \overline{c_{\beta\beta}c_{\beta\alpha}^*} & \overline{c_{\beta\beta}c_{\beta\beta}^*} \end{pmatrix} \quad (9)$$

In this notation, the populations of the eigenstates are located in the diagonal. Each element of the density matrix consists of one of the coefficients in equation (5) multiplied by the complex conjugate of the same or a different coefficient. This product is then averaged out considering all pairs in the ensemble, each existing in a different state $|\psi\rangle_{pair}$. The populations quantify the weight that, on average, each of the four eigenstates available have in the linear combination $|\psi\rangle_{pair}$, considering the whole ensemble of spin pairs.

The off-diagonal elements are called *coherences* and quantify the probability that each spin of the pair undergoes a transition from state $|\alpha\rangle$ to state $|\beta\rangle$ (and vice-versa).

Any NMR experiment represents a sequence of events whose effect on the spin system can be calculated through the density matrix and translates into the change of populations and coherences values, as each event acts on the coefficients of each $|\psi\rangle_{pair}$. The NMR pulse sequence is therefore a time-dependent process that can be designed to create specific coherences and change the populations according to the experiment's goals. Indeed, the shape of the density matrix can be predicted through the resolution of the Liouville Von Newmann equation:

$$\frac{d\hat{\rho}}{dt} = -i\,\hat{\boldsymbol{H}}\hat{\rho} \qquad (10)$$

where $\widehat{\boldsymbol{H}} = [\widehat{H}, \hat{\rho}]$ is called commutator superoperator, as it acts on the operator $\hat{\rho}$ to return the commutator between the density operator itself and the coherent Hamiltonian, i.e. the Hamiltonian resulting from all the coherent interactions that affect the system, such as the Zeeman interaction, the J-coupling and the chemical shift.

Coherent interactions dominate the evolution of the system during the pulse sequence. However, at the end of the experiment and during signal acquisition, the dynamics of the system is dominated by spin-spin interactions that are different in strength and direction throughout the sample and fluctuate in time due to molecular motion. Equilibrium is ultimately reached through these interactions and energy exchanges which modify population and coherences created during the pulse sequence, similarly to the effect of radiofrequency pulses applied during the experiment. However, this phenomenon, generally called *relaxation,* is intrinsically different from the pulse sequence events, as the energy in the spin system is exchanged in a random and disorganised way and through different mechanisms, therefore requiring a different mathematical tool. The return to equilibrium through relaxation is described through a so-called *incoherent* Hamiltonian.

The total spin Hamiltonian can be expressed as the sum of a coherent and an incoherent part:

$$\hat{H}(t) = \hat{H}_0 + \hat{H}_1(t) \tag{11}$$

where $\hat{H}_1(t)$ is the time-dependent incoherent Hamiltonian and $\hat{H}_0$ is the coherent Hamiltonian. It is convenient to express the total Hamiltonian in the interaction frame of the dominant coherent interaction, which is usually the Zeeman interaction. In such frame, the total Hamiltonian is equal to $\hat{H}_1(t)$, and it is possible to write

$$\tilde{H}(t) = \tilde{H}_1(t) \tag{12}$$

where the tilde indicates that both terms have been rotated and expressed in the Zeeman interaction frame. The same rotation can be applied to equation (10), and by using equation (12) on the right-hand side, the Liouville Von Neumann equation can be re-written in the Zeeman interaction frame as

$$\frac{d\tilde{\rho}}{dt} = -i\,\tilde{\boldsymbol{H}}_{\boldsymbol{1}}\tilde{\rho} \tag{13}$$

Equation (13) presents the same form of equation (10), with the operator in bold being the commutator superoperator such that $\tilde{\boldsymbol{H}}_{\boldsymbol{1}} = \left[\tilde{H}, \tilde{\rho}\right]$ and where $\tilde{\rho}$ and the incoherent Hamiltonian $\tilde{H}_1$ have both been expressed in the interaction frame.

Equation (13) can be further transformed to obtain the following

$$\frac{d\tilde{\rho}}{dt} = -\int_0^{\infty} d\tau \ \langle \tilde{\boldsymbol{H}}_{\mathbf{1}}(t)\, \tilde{\boldsymbol{H}}_{\mathbf{1}}(t+\tau)\rangle \, \langle \tilde{\rho}(t)\rangle \tag{14}$$

where the brackets indicate an averaged value due to the fact that the interactions described by $\tilde{\boldsymbol{H}}_{\mathbf{1}}$ change randomly with time. Equation (14) is often written in its more concise form as

$$\frac{d\tilde{\rho}}{dt} = \hat{\boldsymbol{\Gamma}}\,\tilde{\rho} \tag{15}$$

where the integral in equation (14) has been replaced by $\hat{\boldsymbol{\Gamma}}$ called relaxation superoperator. The physical meaning of the equation above is that the relaxation superoperator acts on the density matrix to return its rate of change over time, i.e. its relaxation rate, a numerical constant that quantifies how fast the populations and coherences created during the experiment are lost due to incoherent interactions established in the system during the return to equilibrium.

Equation (15) and equation (10) can be considered together when describing the evolution of population and coherences during the entire NMR experiment, including relaxation:

$$\frac{d\hat{\rho}}{dt} = -i\left(\hat{\boldsymbol{H}} + \hat{\boldsymbol{\Gamma}}\right)\hat{\rho} \tag{16}$$

The equation above states that population and coherences change over time due to coherent interactions as described by the superoperator $\widehat{\boldsymbol{H}}$ and due to incoherent interactions described by the relaxation superoperator $\widehat{\boldsymbol{\Gamma}}$. Equation (16) allows to predict how the experimental conditions will affect populations and coherences, and how the system will behave under the effect of the relaxation mechanisms active in it. As will be thoroughly discussed in 1.4, this knowledge can be used to design NMR experiments where a specific spin system is selected and manipulated *ad hoc* and whose relaxation properties are exploited to extract desired information from the NMR signal. Prior to that, another way to manipulate the experimental conditions, suitable for the purposes of the present work, will be discussed.

1.3. Pulsed magnetic field gradients

Although often discussed as a specific magnetic resonance technique, the use of pulsed field gradients is actually an essential component of almost any modern NMR experiment. In fact, besides being at the heart of MRI scans, magnetic field gradients are found in many NMR pulse sequences with different purposes, due to their crucial effect on the phase of the spins and their coherences.

As previously mentioned, the spins in a sample precess with their Larmor frequency expressed by equation (2) when placed in a static magnetic field B_0. As a RF pulse is applied, coherences are created and can be quantified as off-diagonal elements in the density matrix; consequently, the spins in the ensemble acquire a phase coherence and a detectable transverse magnetisation M_{xy} is created, resulting from all the spins in the ensemble precessing with the same phase ϕ on the x-y plane. For a certain time, the magnetisation is free to precess on the x-y plane, and will gradually decay according to the relaxation constant characteristic of the system, if no other event occurs. In fact, it is possible to further perturb the spin phases in order to make the final signal informative of specific properties of the system. This is achieved through the use of magnetic field gradient pulses, which temporally and spatially modify the intensity of the magnetic field B_0 perceived by the spins in the sample.

If the magnetic field B_g produced by the gradient of intensity g varies along the z-axis according to

$$B_g = gz \tag{17}$$

where z is the distance in metres from the origin of the axis (taken at the centre of the gradient coil) and g is expressed in $\mathrm{T\,m^{-1}}$ or $\mathrm{G\,m^{-1}}$, the Larmor frequency of each spin becomes a function of the position:

$$\omega_0 = \gamma\left(B_0 + B_g\right) = \gamma(B_0 + gz) \tag{18}$$

where γ is the gyromagnetic ratio and B_0 is the static magnetic field. After that the gradient is applied, the spins start precessing at different frequency and their phase also depends on their position along the z-axis:

$$\phi(z) = \gamma\ (B_0 + gz)\ \delta \tag{19}$$

where δ is the duration (in seconds) of the gradient pulse.

This property of making spins phase and precession frequency functions of space, has resulted in magnetic field gradients to be widely exploited for different purposes in NMR. Two uses of magnetic field gradient pulses relevant to this work are described in the following paragraphs.

1.3.1. Magnetic field gradients to study molecular diffusion

Equation (18) states that in the presence of a static magnetic field B_0 and a magnetic field gradient of intensity g applied along the z-axis, spins precession frequency becomes a function of the position and the following can be written

$$\omega_1(\mathrm{z}) = \omega_0 + \gamma g \mathrm{z} \tag{20}$$

Equation (20) states that, if z represents the position in the sample, each spin will precesses with a different frequency $\omega(\mathrm{z})$ when the gradient g is applied along the z-axis. Before any relaxation mechanism can cause a loss of coherence, a distribution of precession frequencies along the z-axis is artificially created; if the gradient is applied immediately after a 90-degree RF pulse, the coherence created by the RF pulse is lost, with the ultimate effect of reducing or destroying the transverse magnetisation and the intensity of the detectable signal. Differently from the loss of signal due to relaxation mechanisms, however, the loss of magnetisation caused by a magnetic field gradient is reversible. In fact, if an equal but opposite in sign gradient is applied immediately after the first one, each spin's precession frequency is decreased of the same amount it was previously increased, with the effect of re-focusing the spins and re-establishing the transverse magnetisation previously de-phased:

$$\omega_2(\mathrm{z}) = \omega_0 - \gamma g \mathrm{z} \tag{21}$$

In such circumstances, the first gradient is called de-phasing gradient while the second is the re-phasing gradient. The effect of such a couple of gradients on the final signal is null in principle, assuming that the position z of each spin did not change in between the two gradients. Figure 1.2 graphically shows the application of such coupled gradient pulses in an NMR sequence and its effect on an ensemble of spins with phase ϕ.

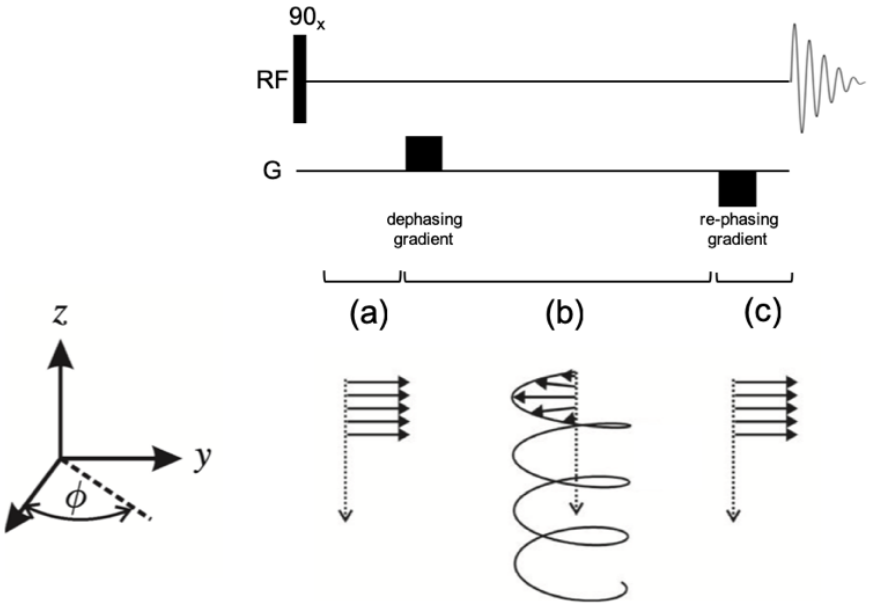

Figure 1.2 Effect of two identical and opposite gradient pulses on an ensemble of spins: **a)** a 90-degree pulse creates coherences on the xy-plane; **b)** the first pulsed gradient de-phases each spin creating a phase distribution along the gradient direction; **c)** the second pulsed gradient re-phases each spin and phase coherence is fully recovered

However, molecular motion in solution makes it generally very unlikely for the spins to retain their position during the time interval between the two gradient pulses. As a consequence, a re-phasing gradient applied after a few seconds from the first de-phasing gradient will not be able to compensate for the loss of phase coherence caused by the latter. This ultimately results in a loss of magnetisation and therefore a loss of signal intensity [9]. This loss of signal can be correlated to the entity of molecular displacement happened in between the gradient pulses, and can therefore provide information about the physical mechanisms responsible for molecular motion in solution such as diffusion. A signal acquired in these conditions can be defined diffusion-sensitised as its intensity gives insights on how fast molecules displace due to their diffusive properties. Before describing how diffusion can be effectively studied through NMR, another application of magnetic field gradients relevant to the present work will be presented.

1.3.2. Magnetic field gradients for selective excitation

Spatial selectivity is another advantage offered by pulsed gradients applied during an NMR pulse sequence. In order to target a confined portion of the sample with the designed sequence of events, the interplay of a gradient pulse and a simultaneous shaped RF pulse is exploited. As previously shown by equation (18), spins in different positions along the z-axis are characterised by different values of the Larmor frequency, when a gradient is applied. If two different sections of the sample are considered, it is possible to write:

$$\omega_1 = \gamma g z_1 \tag{22}$$

$$\omega_2 = \gamma g z_2 \tag{23}$$

if the distance between two regions $\Delta z = (z_2 - z_1)$ is taken, we can write

$$(\omega_2 - \omega_1) = \gamma g (z_2 - z_1) \tag{24}$$

and, consequently

$$\Delta z = \frac{\Delta \omega}{\gamma g} \tag{25}$$

This simple relationship connects the bandwidth $\Delta\omega$ in the distribution of frequencies created by the gradient, with a spatially delimitated region of the sample. This connection allows gradients to label a section Δz of the ensemble and target it with the excitation RF pulse. In fact, a radio-frequency pulse can be shaped to only excite a specific range of frequencies $\Delta\omega$, which in the presence of a simultaneous gradient pulse g will result in the region Δz to be targeted by the pulse, according to equation (25).

Generally speaking, power and duration of a RF pulse are linked through the relationship (valid in a frame rotating at the Larmor frequency in the presence of the static B_0 only)

$$\theta = \gamma B_1 \tau \tag{26}$$

where γ is the gyromagnetic ratio of the irradiated nucleus, B_1 is the intensity of the RF (in terms of its oscillating magnetic field's amplitude), τ is the duration of the pulse and θ is the resulting flip angle of the magnetization. Duration τ is, in turn, related to the range of frequencies $\Delta\omega$ that is excited by the pulse itself, because the function describing the intensity of the pulse in the frequency domain is the Fourier transform (FT) of the function describing the intensity in the time domain. Due to

the properties of FT, shorter pulses (smaller τ) correspond to wider windows of excited frequencies (larger $\Delta\omega$) and *vice versa*. 90-degree pulses found in many NMR pulse sequences are usually intended to excite large range of frequencies in order to include in the spectrum all the nuclei of the same kind in all their different chemical environments; therefore, these pulses are usually very short (a few μs). Since all the frequencies need to be excited, the pulse is non-selective and it is not required for its excitation profile (i.e. its function in the frequency domain) to be particularly accurate in defining the limits of $\Delta\omega$. For this purpose, short pulses that in the time domain display a rectangular profile are commonly used (Figure 1.3), as their FT has rounded edges or often includes frequencies outside the main region, and it is therefore suitable when a broader range of frequencies has to be excited.

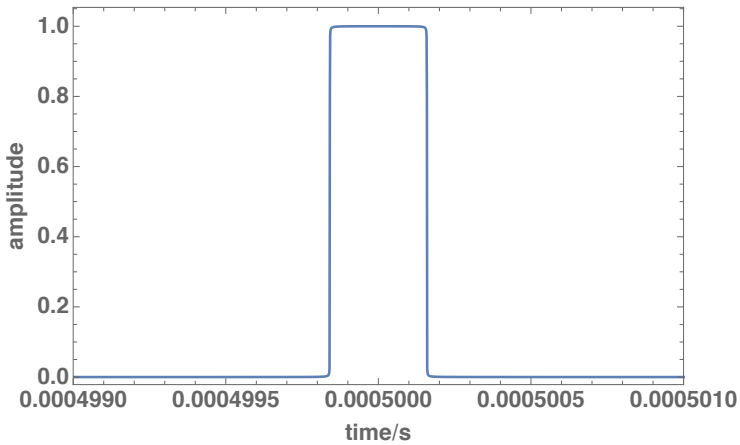

Figure 1.3. Short rectangular pulse in the time domain used to excite the entire range of Larmor frequencies in the sample. The scale of time axis has been enlarged to appreciate the shape of the profile.

Figure 1.4 shows the excitation profile resulting from the FT of the pulse in Figure 1.3. The window of excited frequencies extends for 20 kHz around the reference but a much broader range of frequencies is actually included. This profile is mathematically described by a *Sinc* function, defined in equation (27) and displayed in Figure 1.5.

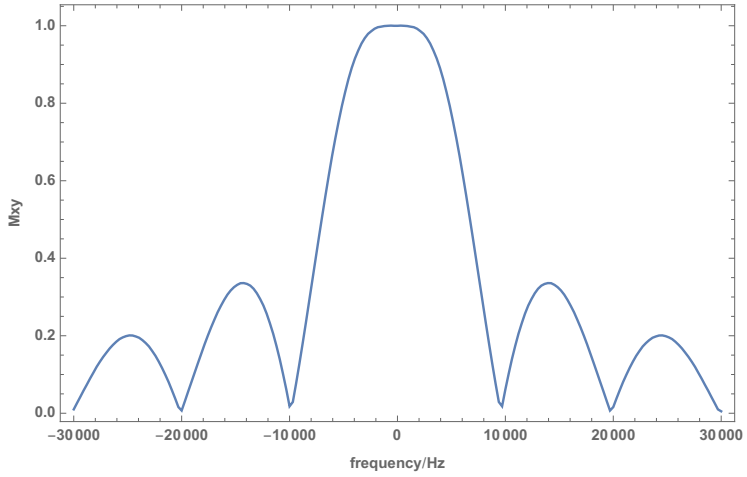

Figure 1.4 Excitation profile of a Sinc3 pulse

$$Sinc(x) = \begin{cases} 1 & if\ x = 0 \\ \dfrac{Sin(x)}{x} & if\ x \neq 0 \end{cases} \quad (27)$$

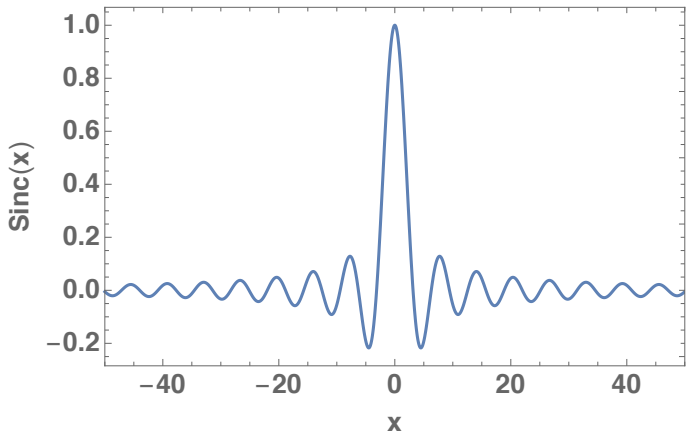

Figure 1.5 Sinc(x) function

Conversely, if *Sinc(x)* is chosen as the function describing the pulse in the time domain, its Fourier transform will generate an excitation profile shaped like in Figure 1.3, where now the sharp edges allow the pulse to address a precisely selected range of Larmor frequencies. This is the strategy used for selective excitation where, as expressed by equation (25), it is possible to make a specific section of spins Δz in the sample undergo the desired evolution, if the strength of the gradient g is applied according to the selected range $\Delta\omega$. Often the thickness of the section is firstly decided, then a suitable gradient strength is set (considering the undesired eddy currents this might generate and the necessary recovery time) and the desired $\Delta\omega$ is consequently calculated.

This strategy is at the core of the study described in Chapter 3, where pulsed field gradients were also applied during acquisition, in order to make the signal position-dependent and to obtain a magnitude-mode spectrum where intensity is a function of the location within the coil region. This approach, routinely used in imaging techniques, was incorporated in the measurement of long relaxation time constants, with the aim of realising a multi-stage experiment and significantly reduce its duration, as will be extensively described in Chapter 3.

University of Southampton

1.4. Molecular diffusion in NMR

As previously seen in 1.3.1, the study of molecular diffusion through NMR experiments is one of the most used application of gradient pulses, besides being a central concept for the purposes of this work. It is therefore worth giving a definition of diffusion and of the mathematical tools that support its rigorous description, before discussing how NMR techniques can be exploited to study diffusion.

1.4.1. What is diffusion

Translational diffusion can be defined as the random thermal motion of molecules, and it is at the heart of any process that involves migration of chemical species. To avoid any ambiguity, a distinction between mutual diffusion and self-diffusion can be made. The term 'mutual diffusion' refers to molecular displacement that results in a macroscopic oriented flux of mass in the presence of a concentration inhomogeneity; it arises from a gradient of chemical potential and brings the system to thermodynamic equilibrium.

Differently, 'self-diffusion' does not need any inhomogeneity to happen, it occurs in liquids at thermal equilibrium and, in the absence of spatial constraints, it results in a mass displacement with no specific orientation. For simplicity, from now on the

term "diffusion" will be used specifically referring to "self-diffusion", if not otherwise specified.

As many other physical phenomena, diffusion can be treated either from a microscopic or a macroscopic point of view. Macroscopic approach treats diffusing molecules as a continuum and is based on Fick's second law. Microscopic approach treats molecules as an ensemble of random walkers and describes the dynamics considering particles position or velocity as functions of time.

When considering a sufficiently long time, the microscopic approach leads to the same result as the macroscopic one: a single number, the diffusion coefficient *D*, that accounts for the effects of all the particles:

$$D = \lim_{t\to\infty} \frac{1}{6t} \langle [r_i(t) - r_i(0)]^2 \rangle \quad (28)$$

where $r_i(t)$ is the position of the particle i at the time t and the angled brackets indicate the average over the ensemble. Both mutual diffusion and self-diffusion can be quantified with such a coefficient and although they represent two phenomena occurring in different circumstances, their coefficients share the same unit ($m^2 s^{-1}$).

At a microscopic level, molecular motion occurs on a timescale far shorter than the timescale accessible with most experimental techniques, which instead are sensitive

to macroscopic behaviour. Therefore, the phenomenological description based on Fick's second law represents a good mathematical framework to experimental measurements, while the molecular-level description is more suitable when numerical techniques are used.

The classical description of diffusion shares its fundamental idea with other kinds of irreversible transportation such as heat conductivity and electric conductivity, where some form of inhomogeneity drives a net mass flux J. It is not possible to know where a certain particle will be at a given time, but it is possible to say that a finite fraction of molecules will cross a certain section at a given time, as a result of a concentration gradient. This is expressed by Fick's first law [10]

$$\mathbf{J} = -D\,\nabla C \tag{29}$$

which can be expanded as

$$\begin{pmatrix} J_x \\ J_y \\ J_z \end{pmatrix} = -D_M \begin{pmatrix} \dfrac{\partial C}{\partial x} \\ \dfrac{\partial C}{\partial y} \\ \dfrac{\partial C}{\partial z} \end{pmatrix} \tag{30}$$

where D_M is the mutual diffusion coefficient. Since mass is conserved, it is possible to write

$$\frac{\partial C}{\partial t} = -\left(\frac{\partial J_x}{\partial x} + \frac{\partial J_y}{\partial y} + \frac{\partial J_z}{\partial z}\right) = -\nabla \mathbf{J} \tag{31}$$

Substituting the definition of the mass flux **J** from (29) in (31) we obtain

$$\frac{\partial C}{\partial t} = \nabla\,(D_M\,\nabla C) \tag{32}$$

which is Fick's second law, also known as the 'diffusion equation' [10].

In the case of self-diffusion, there is no concentration gradient but an analogous equation can be written in terms of a flux of probability density **J**

$$\begin{pmatrix} J_x \\ J_y \\ J_z \end{pmatrix} = -D \begin{pmatrix} \frac{\partial P}{\partial x} \\ \frac{\partial P}{\partial y} \\ \frac{\partial P}{\partial z} \end{pmatrix} = -D\,\nabla P \tag{33}$$

where P is the Probability density function or diffusion propagator, that expresses the probability to find a molecule in a certain position and at a given time. From the continuity theorem we have that

$$\frac{\partial P}{\partial t} = -\left(\frac{\partial J_x}{\partial x} + \frac{\partial J_y}{\partial y} + \frac{\partial J_z}{\partial z}\right) = -\nabla \mathbf{J} \tag{34}$$

and substituting the definition of **J** from (33) in (34) we obtain

$$\frac{\partial P}{\partial t} = \nabla\,(D\,\nabla P) \tag{35}$$

which is the Fick's second law for the probability density function.

It is important to notice that, although the equation above was derived by analogy with the classical Fick's equation for mutual diffusion, the same result is obtained when using elementary model of random walk.

If, for the sake of simplicity, we limit the description to one dimension, what happens along z can be written as

$$\frac{\partial P(z,t)}{\partial t} = D\,\frac{\partial^2 P(z,t)}{\partial z^2} \tag{36}$$

The diffusion propagator $P(z,t)$ can be found by solving this partial differential equation. It is possible to rewrite $P(z,t)$ in terms of its Fourier transform FT, since it results

$$P(z,t) = \frac{1}{\sqrt{2\pi}}\int \tilde{P}(k,t)\,e^{ikz}dk \tag{37}$$

Thus, it is possible to reformulate (36) as

$$\frac{\partial}{\partial t}\frac{1}{\sqrt{2\pi}}\int \tilde{P}(k,t)\, e^{ikz} dk = D\,\frac{\partial^2}{\partial z^2}\frac{1}{\sqrt{2\pi}}\int \tilde{P}(k,t)\, e^{ikz} dk \tag{38}$$

considering that, on the right-hand side of the equation above, the exponential is the only function of z, solving the second derivative leads to

$$\frac{\partial}{\partial t}\frac{1}{\sqrt{2\pi}}\int \tilde{P}(k,t)\, e^{ikz} dk = -Dk^2\frac{1}{\sqrt{2\pi}}\int \tilde{P}(k,t)\, e^{ikz} dk \tag{39}$$

We are allowed to rewrite the differential equation (36) in terms of $\tilde{P}(k,t)$

$$\frac{\partial}{\partial t}\tilde{P}(k,t) = -Dk^2\,\tilde{P}(k,t) \tag{40}$$

this is possible because the set of coefficients $\tilde{P}(k,t)$ to write a certain $P(z,t)$ is unique, therefore the solution to (36) is unique both in terms of $P(z,t)$ and in terms of its Fourier transform $\tilde{P}(k,t)$. In this form, the solution is easily found as

$$\tilde{P}(k,t_0+\Delta) = \tilde{P}(k,t_0)\, e^{-k^2 D(t_0+\Delta)} \tag{41}$$

with

$$\tilde{P}(k,t_0) = \frac{1}{\sqrt{2\pi}}\int P(z,t_0)\, e^{-ikz} dz \tag{42}$$

To go back to our $P(z,t)$ we just replace (41) and (42) in (37). If the time $t = t_0 + \Delta$ is considered, we obtain

$$P(z,t) = \frac{1}{2\pi} \int \int P(z', t_0)\, e^{-ikz'}\, e^{-k^2 D(t_0+\Delta)}\, e^{ikz}\, dz'\, dk \tag{43}$$

The probability density to find a molecule in a certain position at time $t_0 = 0$ can be taken equal to

$$P(z', 0) = \delta(z' - z_0) \tag{44}$$

where $\delta(z' - z_0)$ is the Delta function, whose value is ∞ when $z' = z_0$ and 0 otherwise. For the properties of the Delta function, we can therefore write

$$\int P(z', 0)\, e^{-ikz'}\, dz' = \int \delta(z' - z_0)\, e^{-ikz'} dz' = e^{-ikz_0} \tag{45}$$

and introducing this result in (43) we finally obtain

$$P(z, \Delta) = \frac{1}{2\pi} \int e^{ik(z-z_0)}\, e^{-k^2 D\Delta}\, dk \tag{46}$$

whose solution is the Gaussian function

$$P(z_0, z, \Delta) = \frac{1}{\sqrt{(2\pi\sigma^2)}}\, e^{-\frac{(z-z_0)^2}{2\sigma^2}} \tag{47}$$

where the variance σ^2 is proportional to the total time interval considered Δ

$$\sigma^2 = 2D\Delta \tag{48}$$

and the standard deviation σ defines the diffusion length

$$\sigma = \sqrt{2D\Delta} \tag{49}$$

which is also referred to as Einstein length or *root-mean-square displacement* (d_{rms}).

By replacing this value into the P density function calculated in (47) we obtain

$$P(Z, \Delta) = \frac{1}{\sqrt{4\pi D\Delta}}\, e^{-\frac{Z^2}{4D\Delta}} \tag{50}$$

It is important to notice that (50) does not depend on the initial position z_0 but only on the displacement $Z = z - z_0$. In fact, this result is valid for self-diffusion where no concentration gradient is present and therefore the probability of finding a particle in position z after a time interval Δ does not depend on its initial position z_0. This result was obtained assuming a free, unrestricted molecular motion.

As will be discussed further in this chapter, the analytical shape of the diffusion propagator derived above can be combined with the shape of the NMR signal. The result is the mathematical tool necessary to derive information about diffusion from NMR experiments (see paragraph 1.4.3).

1.4.2. Anisotropy of diffusion

1.4.2.1. The diffusion tensor

In paragraph 1.4.1. diffusion was introduced as a scalar coefficient and an expression was derived for the probability density function to describe molecular displacement through such coefficient, if a random-walk model is assumed. However, a description that better fits the circumstances in a real system should allow the inclusion of an orientation-dependence of D.

Equation (33) states that the probability density flux **J** is a vector parallel to the gradient of the probability density function P, with an opposite sign. In fact, in this expression, the diffusion coefficient D appears to be responsible for the flux intensity only. In real systems, however, it is more likely for the flux to be more

strongly influenced by diffusion. This is better expressed by using a diffusion second-rank tensor, rather than a simple scalar factor:

$$\mathbf{J} = -\mathbf{D}\,\nabla P \tag{51}$$

which corresponds to

$$\begin{pmatrix} J_x \\ J_y \\ J_z \end{pmatrix} = -\begin{pmatrix} D_{xx} & D_{xy} & D_{xz} \\ D_{yx} & D_{yy} & D_{yz} \\ D_{zx} & D_{zy} & D_{zz} \end{pmatrix} \begin{pmatrix} \dfrac{\partial P}{\partial x} \\ \dfrac{\partial P}{\partial y} \\ \dfrac{\partial P}{\partial z} \end{pmatrix} \tag{52}$$

The decision of representing diffusion with a $3x3$ matrix has several advantages; firstly, the use of a tensor accounts for the fact that diffusion in three dimensions might appear to be different depending on the direction of measurement. Generally speaking, this orientation-dependence of a physical quantity is called *anisotropy*. Fick's second law then becomes

$$\frac{\partial P}{\partial t} = \nabla\,\mathbf{D}\,\nabla P \tag{53}$$

the resolution of which leads to an analogous but practically more useful form of the probability density function P in three dimensions

$$P(\mathbf{R}, \Delta) = \frac{1}{\sqrt{|\mathbf{D}|(4\pi\Delta)^3}} e^{-\frac{\mathbf{R^T D^{-1} R}}{4\Delta}} \quad (54)$$

to describe the stochastic molecular displacement in anisotropic conditions [10].

When occurring within the cavities of a complex structure, diffusion can be spatially *anisotropic*, i.e. a different value of the scalar coefficient D is obtained when measured along different directions. Anisotropy of diffusion is a direct consequence of the structural features of the system in which diffusion occurs, and therefore it represents a source of information on the system itself, analogously to solid state NMR which relies on chemical shift anisotropy to gain information on a molecular structure. In this section, the idea of exploiting diffusion anisotropy will be developed, together with the key concepts behind the most common experimental strategies.

Another important advantage of describing diffusion with a rank-two tensor is its direct mathematical link with an ellipsoid whose principal axes are oriented like the tensor's eigenvectors and have a length proportional to the corresponding eigenvalues. As previously mentioned in 1.3.1, NMR can be used to investigate diffusion through the use of magnetic field gradients. An inevitable consequence is that the information obtained is inherently influenced by the reciprocal orientation

of the sample with the direction of measurement. In other words, since these gradients are defined in a reference frame (so-called LAB-frame), the measured values change depending upon the choice of such a reference. Indeed, the main advantage of a rank-2 tensor to describe diffusion is the possibility to exploit its properties to extract information that is invariant under the change of reference frame [11]. The simplest way to obtain such information from NMR experiments is to measure diffusion along three different orthogonal directions in order to determine the trace of the tensor

$$\frac{1}{3}\,\mathrm{Tr}(\mathbf{D}^{\mathrm{LAB}}) = \frac{1}{3}\left(D_{xx}^{\mathrm{LAB}} + D_{yy}^{\mathrm{LAB}} + D_{zz}^{\mathrm{LAB}}\right) \tag{55}$$

This quantity is rotationally invariant and it represents the average value of diffusion along the three directions. In the presence of a non-uniform distribution of spatial confinements, this number is different in each point and it carries information on the texture of the structure the molecule is diffusing within.

As will be discussed in the next paragraph, a more sophisticated way to characterise a system is to measure diffusion along at least six different directions to derive all the six independent components of the tensor in the LAB-frame. In this case, the orientation-dependence of the tensor's elements can be exploited to infer the

position or the alignment of the system relatively to the reference frame. This positional information is found in the non-zero off-diagonal elements, whose value do not describe any physical phenomenon of diffusion (Figure 1.6 a.).

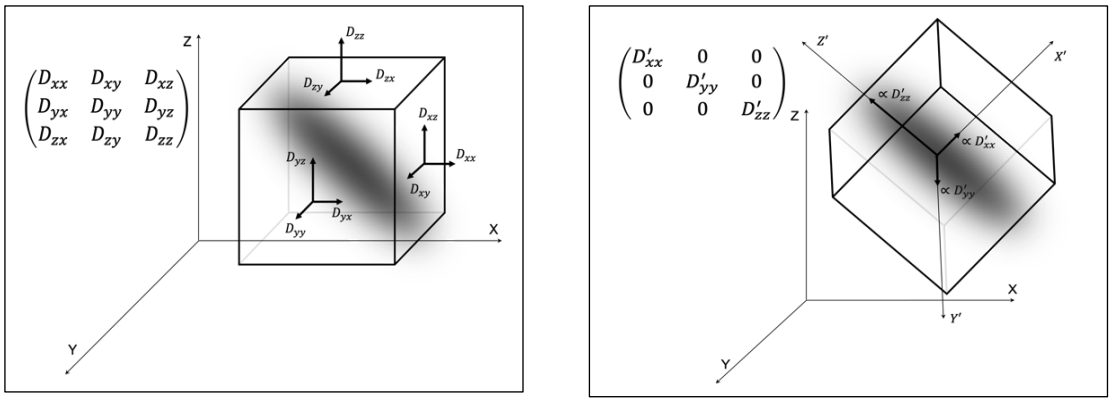

a. b.

Figure 1.6. Random-walk molecular displacement described through a rank-2 tensor: **a.** anisotropic diffusion is represented by a non-diagonal tensor; off-diagonal elements tell about the orientation of the system in the LAB-frame but do not quantify diffusion; **b.** diagonalization makes off-diagonal elements equal to zero and reveals information on diffusion contained in the tensor's eigenvalues only.

Once obtained, the tensor needs to be diagonalized (if not already diagonal by chance). In this step, the positional information is transferred to the eigenvectors from the off-diagonal elements, which in fact become equal to zero. The eigenvalues represent the actual physical quantities measured, and reflect the absolute shape of diffusion which in turn is determined by the structure being investigated. Similar to

the trace, the reliability of the three eigenvalues is ensured by their rotationally invariance (Fig. 1.6 b.).

1.4.2.2. The diffusion regimes

The probability density functions calculated in (50) and (54) were obtained assuming a free and unrestricted diffusion. As a consequence, when these models are used to fit experimental data obtained from molecules diffusing through a more complex structure, the result might not be consistent with the inherent diffusive properties of the chemical species. In fact, deviations from the limiting case of unrestricted diffusion represent the fundamental source of information about the structure. It is actually possible to identify different scenarios, depending on how far from the unrestricted regime they fall. As previously mentioned, the "characteristic diffusion length" can be obtained from the Gaussian shape of the probability density function, and corresponds to the standard deviation $\sigma = \sqrt{2D\Delta}$, called root mean squared displacement (d_{rms}). This indicates the distance a molecule moves (during the time Δ and considering its self-diffusion coefficient D) on average and assuming a free, random motion.

Many materials of interest for diffusion NMR are characterised by cavities, pores and channels whose diameter's order of magnitude is known. Once a certain molecular probe is chosen, knowing the free diffusion coefficient from literature and the maximum value of Δ that is compatible with the experimental conditions, it is possible to calculate the maximum d_{rms} displacement the molecules will move during time Δ. By comparing this value with the characteristic diameter a of the cavity, different cases can be distinguished. These are reported in Figure 1.7, together with the expected shape of the diffusion tensor in the LAB-frame.

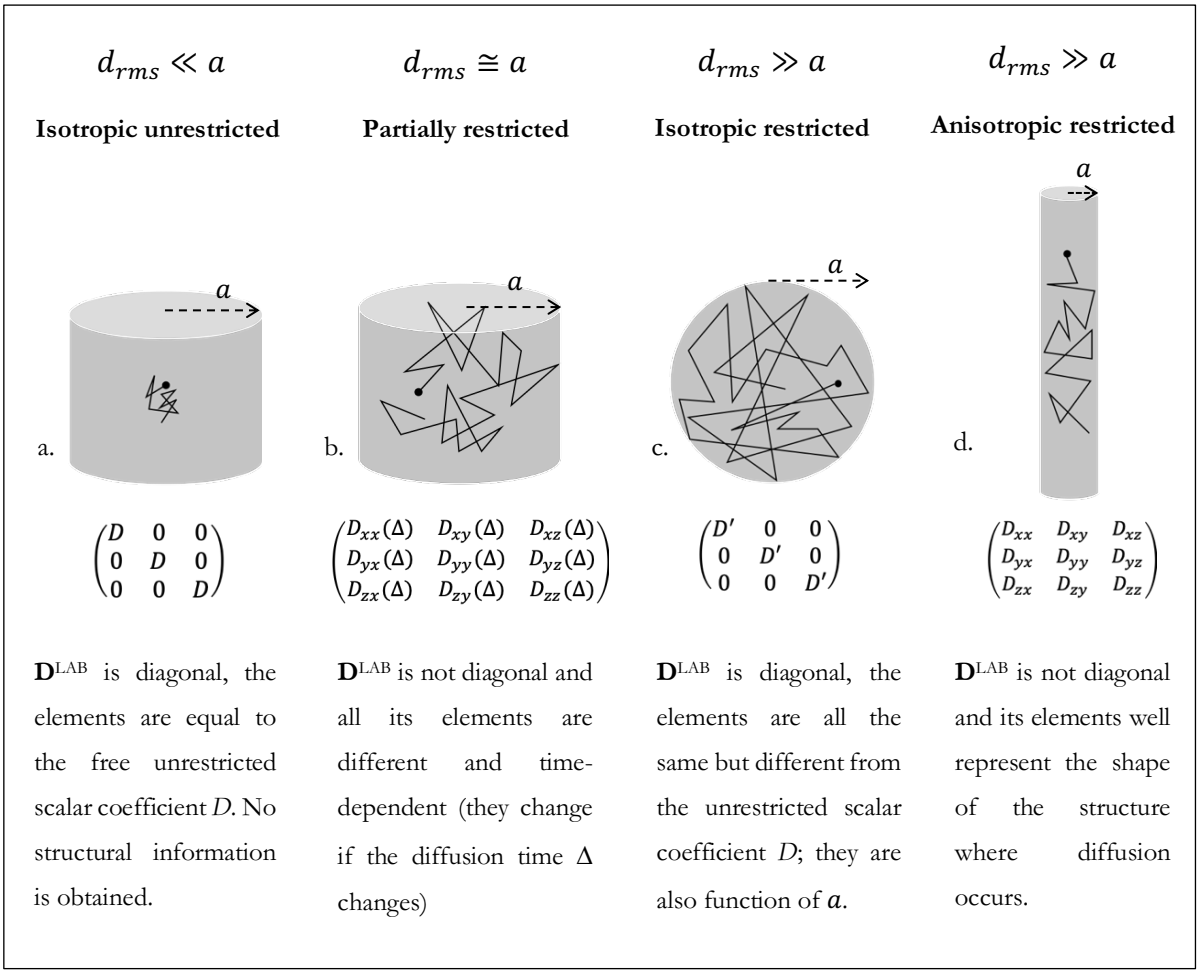

Figure 1.7. Classification of diffusion regimes based on the comparison of molecular root mean square displacement d_{rms} with the characteristic length a of the cavity in which molecules diffuse. All scenarios presented in the picture assume normal (Fickian) diffusion that can be described with a Gaussian model.

The diffusion regime determines the outcome of the experiment. When no barriers influence the random molecular motion (Figure 1.7 a.), the measured diffusion tensor is diagonal and only representative of the inherent properties of the molecule.

No information can be inferred about the environment since this does not affect diffusion in any detectable way. If the d_{rms} is long enough for a good fraction of molecules to experience the spatial constraints (Figure 1.7 b.), the diffusion tensor might report on the surroundings; however, the result is still too susceptible to the time the molecules are observed for, and the tensor is a function of Δ. If the constraints are evenly distributed in space, as it happens in a spherical cavity (Figure 1.7 c.) and molecules have enough time to experience this symmetry, the tensor does not reflect their inherent diffusing properties but it does reflect the spatial homogeneity of the structure: diffusion appears isotropic and the tensor is diagonal. The situation in Figure 1.7 d. represents the most informative: the tensor is not diagonal and the d_{rms} is long enough for most of the molecules to experience the boundaries. The tensor is representative of the structure and its diagonalization leads to information on its shape and orientation in the LAB-frame. The strategies to experimentally determine the diffusion tensor will be discussed later in this chapter, following the more basic techniques developed to obtain the diffusion scalar coefficient form NMR experiments.

1.4.2.3. Anomalous diffusion

It is important to notice that all the scenarios presented in Figure 1.7 assume that diffusion can be described as Gaussian with good approximation, which is true for a system that displays a certain degree of complexity but is not considered a "complex system" in that it does not present properties that are associated with complex systems such as: interactions between its parts, non-linearity of its properties and a level of self-organisation which is intrinsically difficult to model [12]. Indeed, molecular diffusion can occur in physical systems that display these properties, for which the model offered by Fick's law and the Gaussian propagator is not suitable. The concept of anomalous diffusion was introduced to study such cases, and has been observed in numerous systems including amorphous semiconductors, molecular motion within intracellular environment, transportation of particles through biological membranes, chemical migration in structured environments such as gels [13]. Anomalous diffusion has also been successfully applied to infer structural information through diffusion measurement in heterogeneous systems characterised by a high degree of disorder and structural transitions [14]. In these conditions, diffusion deviates from Fick's law in that the square root of d_{rms} does not vary linearly with time as stated by Equation (1). Instead, d_{rms} and time are related through the power law

$$\sqrt{d_{rms}} = 2D_{\alpha}t^{\alpha}$$

(56)

where D_{α} is a generalised diffusion coefficient and α is referred to as the anomalous diffusion exponent [14]. Depending on the system, α can be > 1 (superdiffusion) or < 1 (subdiffusion), while the case with is $\alpha = 1$ is the Fickian or normal diffusion. Subdiffusion can be observed when molecules diffusing within a highly heterogeneous medium are trapped and caged into geometrically restricted zones [14] and diffusion is characterised by a spectrum of stopping times; on the other hand, transition to super diffusion can be observed if the distance moved by a molecule increases abruptly, for example due to transport mechanisms within the system such as those occurring through permeable biological membranes; due to the limited complexity of the systems investigated in the present work, the Gaussian model was assumed as a good approximation.

1.4.3. Diffusion NMR techniques

Among all the techniques that can be used to quantify diffusion, NMR probably represents the most convenient: it is non-invasive, and the diffusing species of interest often contain NMR-sensitive nuclei. NMR is an inherently quantum mechanical subject, while, as previously discussed, the translational motion of molecules is conveniently described with classical mechanics. For this reason, the derivation of the link between its theoretical description and the experimental procedure is of particular methodological interest.

In general, the signal detected at the end of an NMR pulse sequence is complex and its amplitude will be proportional to its real component:

$$e^{i\phi} = \cos\phi + i\sin\phi \tag{57}$$

For an ensemble of spins in a static magnetic field B_0 parallel to the z-axis of the LAB-frame, the overall signal can be expressed as the integral over the ensemble

$$s(t) = \int M(z)\, e^{i\phi(z,t)}\, dz \tag{58}$$

from which it can be seen how signal intensity depends on the amount of magnetisation M created, the length considered in the integration, and the amount of phase coherence created.

As previously mentioned, if a gradient pulse g of duration δ is applied along the z-axis after the first 90-degree RF pulse, the Larmor frequency and spin phase both become functions of the position along gradient's direction. If Z is the distance from an arbitrarily chosen point $z_0 = 0$, the amount of spin "dephasing" in this space interval can be quantified as follows

$$\Delta\phi(z,t) = \gamma\delta g Z \tag{59}$$

The phase difference created along the z-axis by the gradient, reflects on the complex signal in equation (57) which then becomes [9]

$$e^{i\Delta\phi(z,t)} = e^{i\gamma\delta g Z} \tag{60}$$

As discussed in section 1.3.1, the application of two gradient pulses of same intensity and opposite sign, separated by a time interval Δ, results in an attenuation of the signal caused by molecular displacement, occurring during the time Δ. It is now possible to see how an expression for the diffusion-sensitised NMR signal can be

obtained to derive diffusion properties. In fact, the signal obtained from a diffusion NMR experiment will be the combination of the transverse magnetisation created with a phase shift caused by the pulsed gradients, and the propagator describing molecular displacement derived in 1.4.1. (equation (47)). The signal S can therefore be expressed as

$$s = \int P(z, \Delta)\, e^{i\Delta\phi(z,t)} dz$$

$$= \frac{1}{\sqrt{4\pi D\Delta}} \int e^{-\frac{Z^2}{4D\Delta}}\, e^{i\gamma\delta g Z}\, dZ \qquad (61)$$

Equation (61) shows that the final signal is obtained as a superposition of signals where each phase term $e^{i\gamma\delta gZ}$ is weighted by the probability density $P(Z, \Delta)$ of finding a spin in position Z after the time Δ. If no gradient is applied, i.e. $g = 0$, the term $e^{i\gamma\delta gZ}$ becomes 1 and the signal is simply the integral of a Gaussian function, which is 1. In real experiments, with no gradient applied, a signal intensity is obtained $\neq 1$ and we can indicate this non-attenuated signal with s_0. As a consequence, the ratio s/s_0 quantifies the attenuation when a couple of opposite gradient pulses is used.

The solution to the integral in equation (61) is

$$s = s_0 \, e^{-\gamma^2 g^2 \delta^2 D \Delta} \tag{62}$$

generally known as Stejskal & Tanner equation. This equation can be used to fit NMR data and derive the diffusion coefficient D when other experimental parameters are fixed. It is important to notice that equation (62) is only valid on the assumption that the $\delta \ll \Delta$ (narrow gradient limit) and when the gradient g is applied along the z-axis of the LAB-frame. In such conditions, equation (62) can be used to fit experimental data and to obtain the diffusion coefficient along that direction, which in case of isotropic diffusion (case a. in Figure 1.7), is equal to the value that would be obtained by using any other gradient direction. The most commonly used pulse sequences to obtain such data are briefly described in the next section.

1.4.3.1. Measurement of the diffusion coefficient: PGSE and PGSTE

Equation (62) is routinely used to fit data obtained in diffusion NMR experiments. Traditionally, such experiments are based on two main pulse sequences where the

interplay of the two pulsed gradients is exploited: pulsed-gradient spin echo (PGSE) and pulsed-gradient stimulated spin echo (PGSTE).

PGSE is represented in Figure 1.8; it is based on the application of a 90-degree RF pulse that creates transverse magnetization, followed by a delay during which the first pulsed gradient encodes the position of the spins. Then, a 180-degree RF pulse is applied to refocus the magnetization that lost spin coherence on the x-y plane during the delay (usually referred to as relaxation with T_2^*). This transverse magnetisation undergoes the effect of a second pulsed gradient that decodes the position of the spins. The echo is then acquired and an attenuated signal is obtained. By repeating the experiment with different gradient intensities, a series of attenuated signals can be acquired and fitted with equation (62) to calculate the diffusion coefficient D.

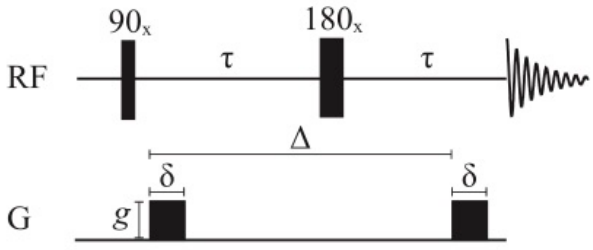

Figure 1.8 The PGSE pulse sequence. In this representation, the gradient of intensity *g* and duration δ was applied with a rectangular function shape; Δ is the diffusion time that separates the two gradient pulses and τ is the echo time.

PGSTE pulse sequence is shown in Figure 1.9 and it consists of a modified version of the PGSE to store information on longitudinal magnetisation rather than on transverse magnetisation. After a 90-degree pulse that creates coherence along the y-axis, the first pulsed field gradient de-phases the spins encoding their position. Differently from the PGSE, however, the first gradient pulse is immediately followed by a second 90-degree pulse, to store the magnetization along the z-axis. This way, diffusion is observed for a time Δ during which spin relaxation determines the decay with constant T_1 rather than T_2. As T_1 is usually longer than T_2, PGSTE pulse sequence allows to set a diffusion time Δ greater than the maximum possible with PGSE and to explore diffusion on longer distances. At the end of Δ, magnetisation is brought back on the x-y plane by another 90-degree pulse, the second gradient pulse decodes the position of the spins. Attenuated signals acquired through these experiments can be then fitted using equation (62).

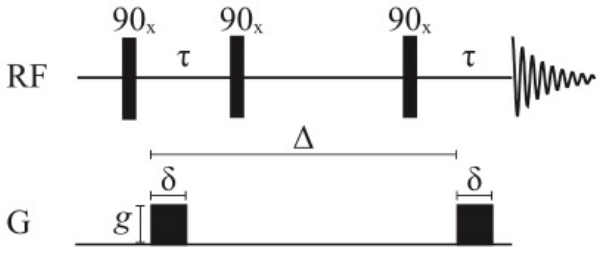

Figure 1.9. The PGSTE pulse sequence. In this representation, the gradient of intensity g and duration δ was applied with a step function shape; Δ is the diffusion time that separates the two gradient pulses and τ is the echo time.

Equation (62) allows to obtain the real diffusion coefficient of a species if the experiments above are carried out in unrestricted or partially restricted regimes, i.e. when diffusion is the same in all directions, or can be considered to be so with good approximation. When diffusion takes place in restricted conditions, PGSE and PGSTE pulse sequences, together with Equation (62) can only lead to an *apparent* diffusion coefficient, often referred to as ADC. This value can be informative of local changes in the environment where diffusion is occurring, but it only provides information along the specific direction of the gradient used.

As discussed in 1.4.2., when diffusion displays a different value depending on the direction of observation, it is better described by a rank-2 tensor. The next section describes how the NMR experiments described above can be adapted to this case.

1.4.3.2. Measurement of the diffusion tensor: DTI technique

Diffusion tensor imaging (DTI) is a technique widely used in biomedical field to determine the shape, orientation and connectivity of long fibres, in particular axons in brain tissue [15, 16]. DTI is based on the measurement of a diffusion tensor for each voxel, and the creation of images using the corresponding ellipsoids as a

contrast; the principal axis corresponding to the largest eigenvalue is assumed to be the main direction of diffusion within that voxel [11]. In human brain, grey and white matter are characterised by axon fibres whose average diameter is the order of $10\ \mu m$ [16] forming a complex framework of cell walls and membranes that hinder the random self-diffusion of water. However, while in grey matter these structures do not show a preferred orientation, in white matter the bundles of fibres and membranes appear to be aligned along certain orientations. Therefore, when characterising brain tissue with the measurement of the diffusion tensor using water as a molecular probe, the results usually correspond to the case c and d of Figure 1.7 for grey and white matter respectively [16]. If a relaxation time T_1 of ~ 1 second and a diffusion coefficient of $2 \times 10^{-9}\ m^2 s^{-1}$ at $25\ °\mathrm{C}$ are assumed for water, Equation (1) shows that it is possible to track diffusion for a length of $60\ \mu m$. Due to the average diameter of white matter fibres, the conditions are such that diffusion will be restricted during the measurement. If a diffusion tensor is obtained for each voxel in the field of view, the principal axes of the corresponding ellipsoids can be used to derive the direction of diffusion and therefore of the fibres. In order to experimentally derive the six independent components of the diffusion tensor, PGSTE pulse sequence is applied multiple times using at least six different gradient directions. These data need to be fitted by a version of equation (62) which accounts

for the use of a gradient in a direction of space different from the z-axis. A more general equation can be obtained by solving equation (61) where the propagator shown in equation (54) is used instead, and the integration is carried out over the three directions of space [9]. If the narrow gradient approximation holds, the result is

$$s = s_0 e^{-\gamma^2 \delta^2 \Delta \, \boldsymbol{g}^T \boldsymbol{D} \boldsymbol{g}} \tag{63}$$

where the gradient $\boldsymbol{g}$ is now a vector and diffusion is represented by the 3×3 matrix **D.** In the logarithmic form, we can rewrite equation (63) as

$$\ln s/s_0 = -\gamma^2 \delta^2 \Delta (g_x^2 D_{xx} + g_y^2 D_{yy} + g_z^2 D_{zz} + 2 g_x g_y D_{xy} + 2 g_x g_z D_{xz} + 2 g_y g_z D_{yz}) \tag{64}$$

In equation (64), the components of the symmetric diffusion tensor are the only unknown values. If at least six $\ln s/s_0$ values are experimentally obtained, the elements of the diffusion tensor can be calculated using multivariate linear fitting of the resulting system. Being an imaging technique, DTI involves the acquisition of a big amount of data, aiming to calculate the diffusion tensor elements for each voxel of the image. The diagonalization of each tensor leads to the eigenvalues and

eigenvectors that shape the profile of diffusion in that voxel, from which the orientation of the fibre can be inferred and displayed as an ellipsoid (Figure 1.10).

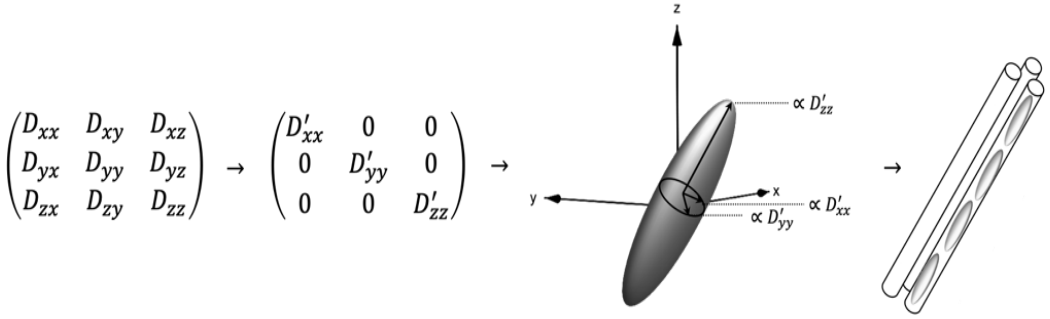

Figure 1.10 DTI data processing to reveal fibre's orientation. A diagonalized diffusion tensor and its corresponding ellipsoid is obtained for every voxel. The principal axes of the ellipsoids allow to track the preferred direction of diffusing molecules.

The data acquired with DTI procedure can be processed and analysed in many different ways and a great effort has been made to develop new methods to extract any useful information. A particular quantity relevant to this work is the fractional anisotropy (FA), a scalar, dimensionless normalised value calculated as a combination of the tensor's eigenvalues

$$\mathrm{FA} = \sqrt{1 - \frac{D'_{xx}D'_{yy} + D'_{xx}D'_{zz} + D'_{yy}D'_{zz}}{(D'_{xx})^2 + \left(D'_{yy}\right)^2 + (D'_{zz})^2}} \qquad (65)$$

FA can be used to evaluate the presence of a preferred direction of diffusion with a single number. Maps of this quantity can be realised, analogously to what is done with the trace of the diffusion tensor previously mentioned.

DTI represents a fortunate technique to characterise various types of structures in the biomedical field. One of the aims of the present work was to verify if it is possible to extend its scope by combining it with a modified PGSTE pulse sequence, developed by this group and designed to populate long-lived singlet spin state to achieve a longer diffusion time Δ. In the next paragraph, basic concepts regarding the singlet state and its properties, are presented.

University of Southampton

1.5. Long-lived singlet spin order

1.5.1. Relaxation of transverse and longitudinal magnetisation

As discussed in section 1.1 and 1.2, for any given spin system such as a single, isolated spin-1/2 or an isolated pair of coupled spins-1/2, the Hamiltonian can be written considering the interactions the system experience. The eigenfunctions of such Hamiltonian form a basis that can be used to write any possible state $|\psi\rangle$ of the system. For a pair of weakly-coupled spins-1/2 the eigenfunctions of the Hamiltonian (equation (4)) are the so-called Zeeman product states $|\alpha\alpha\rangle$, $|\alpha\beta\rangle$, $|\beta\beta\rangle$, $|\beta\alpha\rangle$. Figure 1.11 a. represents an NMR sample in the LAB-frame, where an ensemble of weakly-coupled spin-1/2 pairs in solution experience an external static magnetic field B_0 along the z-axis.

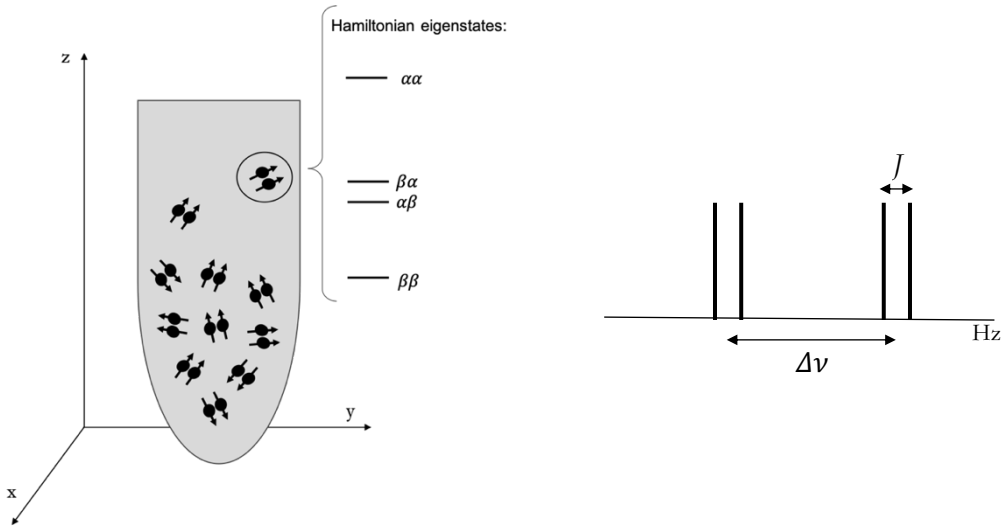

a. b.

Figure 1.11 a. The eigenstates of each pair of weakly-coupled spins-1/2 are the four Zeeman product states $|\alpha\alpha\rangle$, $|\alpha\beta\rangle$, $|\beta\beta\rangle$, $|\beta\alpha\rangle$; **b.** an ensemble of weakly-coupled spin pairs-1/2 generates four peaks from the four coherences -1 that appear in the density matrix of the system.

Figure 1.11 b. shows the NMR spectrum of such a system. The four peaks observed can be justified if the density operator introduced in section 1.2 and reported below, is considered.

$$\hat{\rho} = \overline{|\psi\rangle\langle\psi|} = \overline{c_{\alpha\alpha}c_{\alpha\alpha}^{*}}\ |\alpha\alpha\rangle\langle\alpha\alpha| + \cdots + \overline{c_{\beta\alpha}c_{\alpha\beta}^{*}}\ |\beta\alpha\rangle\langle\alpha\beta| \quad (66)$$

The expression above shows how the density operator is a combination of projection operators such as $|\beta\alpha\rangle\langle\alpha\alpha|$, each multiplied by a complex coefficient. It

is possible to show that some of these operators have a peculiar effect when applied on the Zeeman product states. If the operator $|\beta\alpha\rangle\langle\alpha\alpha|$ is considered, its effect on the eigenstate $|\alpha\alpha\rangle$ can be calculated as:

$$|\beta\alpha\rangle\langle\alpha\alpha| \;\; |\alpha\alpha\rangle = |\beta\alpha\rangle \; \langle\alpha\alpha|\alpha\alpha\rangle = |\beta\alpha\rangle \tag{67}$$

as the Zeeman product states form an orthonormal basis and therefore $\langle\alpha\alpha|\alpha\alpha\rangle = 1$. Equation (67) shows that the coherence $|\beta\alpha\rangle\langle\alpha\alpha|$ is in fact an operator that acts on the state $|\alpha\alpha\rangle$ to transform it into the state $|\beta\alpha\rangle$ where one of the two spins of the pair has changed its state from α to β while the other has retained its state α. The coefficient of this term, $\overline{c_{\beta\alpha}c^*_{\alpha\alpha}}$, is referred to as coherence of order -1, to indicate the transition $\alpha \rightarrow \beta$ induced by the corresponding operator. In general, the coherences -1 of a spin system are the only ones responsible for producing a signal. The detectable magnetisation, called transverse magnetisation M_{xy}, is the direct result of coherences -1 and the source of the signal detected on the x-y plane.

The density matrix of the system considered in Figure 1.11, contains four elements like $\overline{c_{\beta\alpha}c^*_{\alpha\alpha}}$, i.e. coefficients of operators that cause a transition $\alpha \rightarrow \beta$ in the spin pair. The four peaks observable in the spectrum of Figure 1.11 b. are the results of these four coherences -1.

If the term $|\beta\beta\rangle\langle\alpha\alpha|$ is considered instead, and applied to the Zeeman eigenstate $|\alpha\alpha\rangle$, the following results

$$|\beta\beta\rangle\langle\alpha\alpha|\ |\alpha\alpha\rangle = |\beta\beta\rangle\ \langle\alpha\alpha|\alpha\alpha\rangle = |\beta\beta\rangle \tag{68}$$

in this instance, both spins in the pair undergo a transition $\alpha \rightarrow \beta$ under the effect of the operator $|\beta\beta\rangle\langle\alpha\alpha|$. The corresponding coefficient $\overline{c_{\beta\beta}c_{\alpha\alpha}^{*}}$ is said to be a coherence of order -2, to indicate that two transitions are induced. Differently from coherences of order -1, coherences -2 do not result in detectable signal and, if created during the pulse sequence, are not observable in the spectrum. Nevertheless, incoherent interactions (referred to as "relaxation mechanisms" in section 1.2), affect all coherences and populations created, and cause them to exist for a limited time once that the system is left to return to equilibrium. The duration of coherences -1 and the resulting transverse magnetisation M_{xy} is crucial in NMR experiments, as it corresponds to a gradual loss of the signal acquired. Since both populations and coherences are combinations of the same set of coefficients, any RF pulse that affects coherences also affects populations and vice-versa. When coherences are created, populations are modified.

Populations are directly correlated to longitudinal magnetisation M_z. Specifically, M_z is determined by the difference between the population of the eigenstate at highest energy and the population of the eigenstate at lowest energy. The difference between populations of two spin energy levels is known as *spin order*, and when the difference is between the outer two spin energy levels we call this *longitudinal order*. Since populations and coherences are intrinsically correlated, the lifetime of populations created during the pulse sequence, and therefore of M_z, is crucial to the final acquired signal, too. The rate of decay for M_z and M_{xy} caused by relaxation mechanisms can be quantified through the use of the relaxation superoperator $\hat{\Gamma}$ introduced in section 1.2. In fact, a different operator $\hat{\Gamma}_\Lambda$ can be written for every mechanism Λ that contributes to the relaxation of any term in $\hat{\rho}$.

If $R^\Lambda_{M_{xy}}$ is the rate at which M_{xy} decays due to the mechanism Λ, it is possible to write

$$R^\Lambda_{M_{xy}} = \left(M_{xy}|\hat{\Gamma}_\Lambda|M_{xy}\right) \tag{69}$$

with the operation $(A|B)$ defined as follows

$$(A|B) = Tr\{A^+B\} \tag{70}$$

The inverse of the resulting value is called relaxation decay time constant, and for M_{xy} it is generally known as T_2.

$$\frac{1}{R^{\Lambda}_{M_{xy}}} = T_2^{\Lambda} \tag{71}$$

where T_2^{Λ} quantifies the contribution of the interaction Λ to the decay of transverse magnetisation. Similarly, it is possible to calculate the contribution of the mechanism Λ to the relaxation of longitudinal magnetisation M_z as

$$R^{\Lambda}_{M_z} = \left(M_z|\hat{\Gamma}_{\Lambda}|M_z\right) \tag{72}$$

The decay rates for different mechanisms are additive and contribute to the final relaxation properties of the system; however, depending on the system considered, some interactions can be more effective than other in the processes that lead to the magnetisation decay. In an NMR experiment carried out on a sample of spin-1/2 pairs in solution, the main interaction responsible for the loss of populations and coherences (and therefore of M_z and M_{xy}) is an intra-pair interaction called dipole-dipole coupling (ipDD). This results from the nuclei sensing each other's presence due to the local magnetic field they generate, without mediation from the surrounding electrons. If the rate of decay is calculated for the interaction $\Lambda =$

ipDD, it is possible to show that, for small molecules in non-viscous solvents and high magnetic field, is $R_{M_{xy}}^{\mathrm{ipDD}} = R_{M_z}^{\mathrm{ipDD}}$ i.e. both longitudinal and transverse magnetisation are affected to the same extent by the intra-pair dipolar coupling.

Similarly to M_{xy} decay rate, it is also possible to write M_z relaxation decay time constant as

$$\frac{1}{R_{M_z}^{\Lambda}} = T_1^{\Lambda} \tag{73}$$

As ipDD is the main relaxation mechanism that affect T_1 in isotropic, low viscosity liquids, the extent of T_1 is crucial to many NMR experiments that rely on the time available for information storage. From an experimental point of view, T_1 can be measured using inversion recovery or saturation recovery pulse sequences. For the purposes of the present work, saturation recovery pulse sequence was used and is schematically displayed in Figure 1.12

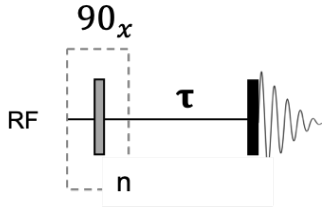

Fig. 1.12 Saturation recovery pulse sequence for T_1 measurement

At the beginning of the T_1 measurement through saturation recovery, a strong series of n 90-degree pulses destroys any magnetization on the z-axis. The system is then left free to evolve for a variable delay τ during which longitudinal magnetization recovers. A second 90-degree pulse brings the magnetization on the xy-plane where it can be measured. The same experiment is repeated with a variable number of increasing delays and the magnetization is plotted as a function of τ and fitted with equation (74) to determine the value of T_1. Fitting parameter M_{eq} corresponds to the magnetization measured with the maximum delay, which is set at 5 times the expected $T_1$to make sure the magnetization on the z-axis had fully recovered.

$$M_z(\tau) = M_{eq}\left(1 - e^{-\tau/T_1}\right) \tag{74}$$

As discussed in 1.3, when NMR experiments are carried out to investigate other physical properties of the system, information can be stored on the magnetisation created, and the NMR signal can be sensitised to the property of interest. This makes relaxation decay a limitation to the time a property can be observed for. A strategy to overcome this limitation, crucial to the present work, is described in the following section.

1.5.2. Relaxation of singlet order

So far, an ensemble of weakly-coupled spin-1/2 pairs was considered. If each pair of the ensemble is made of chemically (and, therefore, magnetically) equivalent spins instead, the description of the system presents some interesting differences. The spins in such pairs still sense each other through the electrons holding the molecule together, therefore they have a J-coupling constant; however, due to the fact that their chemical surrounding is identical, they also experience the same chemical shift. This causes the Hamiltonian of the system to be different from the weakly-coupled spin pair; as a consequence, the Zeeman product states are not eigenstates anymore; instead, the eigenstates of the new Hamiltonian form a basis of a *singlet* and three *triplet states*

$$|S_0\rangle = \frac{1}{\sqrt{2}}(|\alpha\beta\rangle - |\beta\alpha\rangle)$$

$$|T_1\rangle = |\alpha\alpha\rangle$$

$$|T_0\rangle = \frac{1}{\sqrt{2}}(|\alpha\beta\rangle + |\beta\alpha\rangle)$$

$$|T_{-1}\rangle = |\beta\beta\rangle \qquad (75)$$

The spectroscopy of such system involves the three triplets only, as the singlet state $|S_0\rangle$ has total spin $I = 0$ and it is therefore non-magnetic. The triplet manifold presents two coherences -1 which result in two peaks in the spectrum, corresponding to the transitions $|T_0\rangle \rightarrow |T_1\rangle$ and $|T_1\rangle \rightarrow |T_{-1}\rangle$. In isotropic liquids, however, the three states are separated by the same distance in energy, therefore the two transitions result in a single peak (Figure 1.13 c).

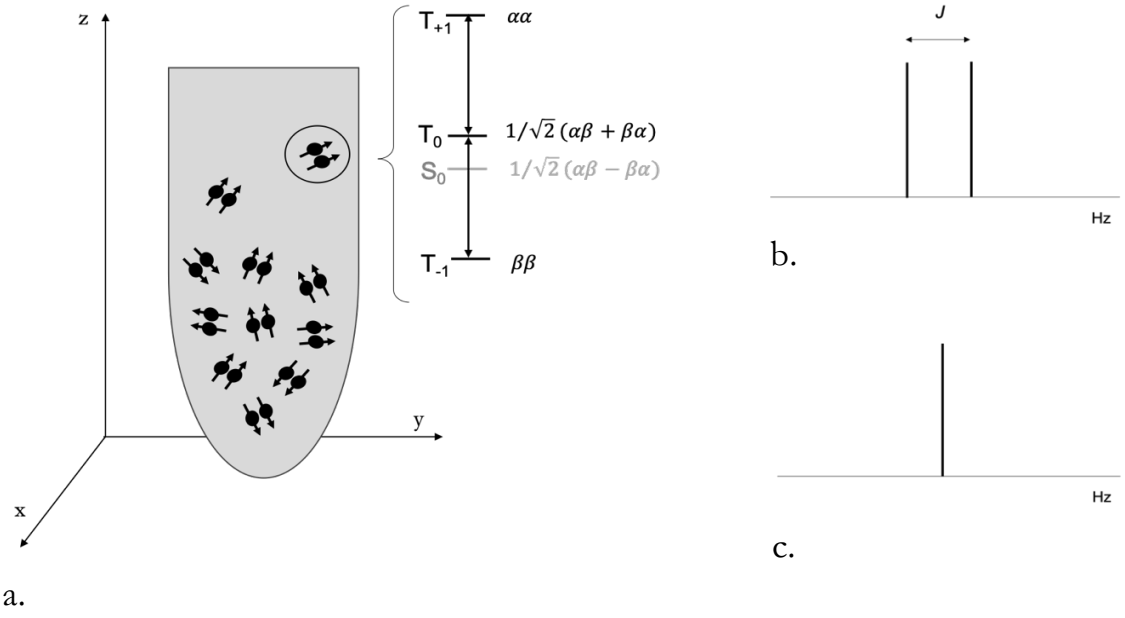

Figure 1.13 a. The eigenstates of each pair of magnetically equivalent spins-1/2 are three triplet states and an NMR-silent singlet state; **b.** an ensemble of magnetically equivalent spin-1/2 pairs generates two peaks from the two coherences -1 in the triplet manifold; **c.** in isotropic liquids, the dipole-dipole coupling contribution to the Hamiltonian vanishes and the two peak coincide.

Although the singlet state $|S_0\rangle$ cannot be involved in the transitions that cause coherences -1 and therefore a signal, the coefficients in the density matrix of this system can still be manipulated through RF pulses to create populations and non-detectable coherences. In particular, the population $|S_0\rangle\langle S_0|$ can be created and the difference with the population of the states in the triplet manifold, i.e. $|T_M\rangle\langle T_M|$ with $M = -1, 0, 1$, can be calculated and it is known as *singlet order,* S. As any other element of the density matrix, singlet order has a limited duration, due to the various mechanisms that cause the system to reach thermal equilibrium after being perturbed.

It is possible to calculate the contribution of ipDD mechanism to the rate of decay of singlet order by calculating

$$R_S^{\mathrm{ipDD}} = \left(\mathrm{S}|\hat{\Gamma}_{\mathrm{ipDD}}|\mathrm{S}\right) \tag{76}$$

as previously done for M_z and M_{xy}. Interestingly, this result is zero, meaning that intra-pair dipolar coupling does not affect the lifetime of singlet order. Different mechanisms cause singlet order to decay towards equilibrium, and a relaxation constant T_s can be calculated for other mechanisms, and experimentally obtained as will be discussed later .

The immunity of singlet order from ipDD relaxation mechanism offers the opportunity to store information for a longer time than what possible with M_z. The strategy is to create singlet order and exploit its longer lifetime to observe the property of interest. Then, singlet order needs to be converted into detectable magnetisation so that the signal can reveal what happened to the system while the silent state was populated.

1.5.3. Singlet state population

Preparation of singlet order is achieved through a carefully designed RF pulse sequence, but starts with the design of the appropriate spin system. In fact, an ensemble of equivalent spin-1/2 pairs is not a suitable option, as the population of singlet state through coherent radio-frequency manipulation would require individual access to the spins of the pair, which are indistinguishable [17]. An alternative is to use a condition of nearly-equivalence, where the difference in chemical shift of the two spins in the pair is very small but different from zero. In particular, for a system of coupled spins-1/2 whose chemical shift difference is much smaller than their J-coupling constant (in isotropic liquids [8]), the Singlet and Triplets states are, with good approximation, eigenstates of the Hamiltonian and can

therefore be populated through RF pulses. Such system can be obtained through the synthesis of a molecule where the two spin-1/2 are surrounded by a nearly-equivalent chemical environment.

For a pair of nearly-equivalent spins-1/2, singlet order preparation and acquisition can be achieved through the two-blocks pulse sequence showed in Figure 1.14.

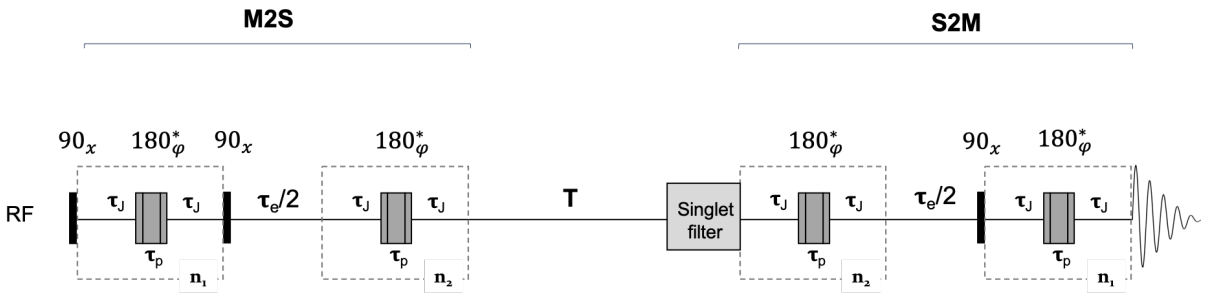

Figure 1.14 M2S2M pulse sequence used to create singlet order and measure its relaxation decay constant T_s (details in the text).

This pulse sequence has been named M2S2M as it is made of two blocks that convert magnetisation into singlet and successively back to detectable magnetisation. The M2S block converts longitudinal magnetisation into singlet order through two J-synchronised echo trains: a first train of n_1 echoes is applied to prepare coherences between $|S_0\rangle$ and $|T_{\pm 1}\rangle$; the next 90-degree pulse, followed by a delay $\tau_e/2$, converts

those coherences into a coherence between $|S_0\rangle$ and $|T_0\rangle$; then, the second train of echoes of duration $n_2 = n_1/2$, finally converts this coherence into a population difference, which is the desired singlet order S. M2S by-products are filtered out and singlet order is selected, then converted back into detectable transverse magnetisation by the S2M block, which corresponds to the M2S reversed in time. The parameters n_1, n_2 and the echo-time τ_e, must be optimised to ensure the effectiveness of the procedure for the specific chemical shift difference in the spin system and the specific solvent used. Pulse sequence in Figure 1.15 called J-synchronised echo, JSE, is composed by a single echo train and it is used for the optimisation of such parameters.

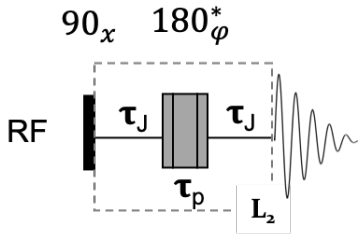

Figure 1.15 JSE pulse sequence used to optimise parameters required in single order preparation

During a JSE, a 90-degree pulse creates transverse magnetization, which corresponds to coherences between the triplet states $|T_{-1}\rangle$ and $|T_{+1}\rangle$; then a train

of spin echoes prepares coherences between $|S_0\rangle$ and $|T_0\rangle$. The imperfections of the result are minimised by the use of a composite 180-degree pulse and phase cycling. The pulse sequence is repeated for an array of the delay time τ_{J}, whose optimal value is then used to calculate echo time τ_e using the following relationship

$$\tau_e = \tau_p + 2\tau_{\mathrm{J}} = \frac{1}{2\sqrt{(\mathrm{J}^2 + \Delta\nu^2)}} \tag{77}$$

A second experiment is then carried out for an array of L_2, the number of echoes in the train. An estimate of its theoretical value is possible from the relationship

$$\mathrm{L}_2 = \frac{\pi J}{2\Delta\nu} \tag{78}$$

where $\Delta\nu$ is the difference in chemical shift of the two nearly-equivalent coupled spins and J is their coupling constant. The number of echoes in the M2S2M pulse sequence, $n_1$corresponds to $L_2/2$ where L_2 has been optimised through the JSE described above.

University of Southampton

1.5.4. T_s measurement

To measure singlet relaxation constant, an experiment analogous to the T_1 measurement described in 1.5.1. needs to be performed. M2S2M pulse sequence showed in Figure 1.14 is also used to measure singlet-order relaxation time constant T_s, by creating an array of increasing values for the time interval T, placed in between the two blocks. After a 90-degree pulse, the M2S block converts transverse magnetization into singlet order: a first train of *J*-synchronised echoes is applied to prepare coherences between $|S_0\rangle$ and $|T_{\pm 1}\rangle$; where L_2 is the value optimised with the JSE; The acquired signals are plotted against the T values and fitted with the following equation

$$M_z(\mathrm{T}) = M_{eq}\, e^{-\mathrm{T}/T_s} \tag{79}$$

Experimentally, it has been shown that singlet order can be orders of magnitude longer than the most common T_1values [2,3] Specific pulse sequences have been developed in this research group to populate singlet state in a system of two coupled spin-1/2 nuclei [18]; the resulting singlet order has shown to have relaxation decay constant of 10 minutes for protons [19], and up to hours for pairs of carbons in suitable conditions [20, 21].

University of Southampton

2. Diffusion tensor measurement on model systems

As previously discussed, a molecular species diffusing in its liquid solvent can be used as a probe exploring the 3D features of a structure in diffusion NMR experiments; any obstruction to molecular random motion influences the experimental outcome and it makes the NMR spectrum informative on the structure under investigation. This information, however, is stored in the created spin order, which in turn is subject to relaxation decay. In diffusion experiments, time is directly correlated to the distance molecules travel while under observation; this correlation can be expressed by the root-mean-square displacement introduced in section 1.4.1., $d_{rms} = \sqrt{2D\Delta}$. The duration Δ can be set according to the goal of the experiment, i.e. the spatial length that needs to be explored to characterise a structure. However, Δ is subject to an upper limit due to the limited life of the spin order. As a consequence, the internal architecture of many solid systems cannot be investigated through diffusion techniques, as the dimensions of the cavities is such that relaxation occurs far before molecules can experience any confinement. In this scenario, diffusion would appear to be isotropic and the NMR signal cannot provide any structural insight. Currently, the threshold of routine diffusion NMR is a probed

distance of $10 - 100\ \mu m$, corresponding to a timescale of the order of seconds, for common molecular probes [16].

In 1.5. the possibility to work with singlet spin order was described, as this can survive significantly longer than the average T_1 used in routine NMR experiments. The relaxation times achieved in recent experiments carried out in this research group have paved the way to the investigation of structures with a system of wider cavities that cannot be described by conventional diffusion NMR techniques [5]. In a recent study published by this group, singlet-assisted diffusion *q*-space experiments were carried out and provided the first evidence for the effectiveness of theoretical models used to describe molecular displacement within a specific geometry [5,22]; in that instance, unprecedented length of 2 mm was probed through a modified PGSTE pulse sequence in a technique dubbed SAD NMR (singlet-assisted NMR); in another study, the same pulse sequence was used to successfully estimate structural parameters such as tortuosity in a system of macroscopic cavities [23]; furthermore, selective singlet-tagging for the imaging of macroscopic diffusion was also implemented [19] showing the versatility of this resource.

A further step was to combine SAD NMR with diffusion tensor imaging (DTI) methodology and data processing to probe the structure of a sample in three dimensions, exploiting the longer Δ achievable thanks to the singlet relaxation

properties. Two samples were prepared to investigate diffusion in different environments. Each sample consisted of a custom-made plastic structure with cylindrical channels with a different alignment. The structures were then immersed in a solution of the molecular probe of choice to fill the channels and allow molecular diffusion to occur within them. Singlet-assisted diffusion experiments were carried out to determine the average diffusion tensor, whose eigenvalues correctly reflected the particular inclination of the channels in both systems. Experimental details and results are reported in this chapter as a successful application of singlet order combined with three-dimensional diffusion NMR experiments for the calculation of a diffusion tensor.

2.1. Material and methods

2.1.1. Plastic inserts

The two structures under investigation were designed in house and CNC machined using Polyoxymethylene (POM). This material was selected as chemical compatible, solvent resistant and easy to machine.

A number of channels of 1 mm cross section were drilled into a solid cylinder of POM with an outer diameter of 7.65 mm and height of 20 mm. In one of the them

(00D), channels were drilled parallel to the cylinder's longitudinal axis, whereas on the other (30D) they were tilted forming a 30-degree angle with the longitudinal axis. All details of both structures are summarized in Figure 2.1.

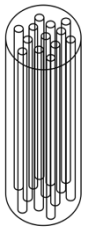

00D	
No. of channels	13
Angle θ with longitudinal axis	0
Channel diameter	1 mm
Channels Volume	204 mm^3
Free volume	36 mm^3

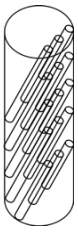

30D	
No. of channels	15
Angle θ with longitudinal axis	30
Channel diameter	1 mm
Channels Volume	127 mm^3
Free volume	36 mm^3

Figure 2.1 3D structures used as model systems to study diffusion in restricted conditions

2.1.2. Molecular probe

A suitable molecular system, 1-(ethyl-d_5)4-(propyl-d_7)(Z)-but-2-enedioate (from now on, EPM) was synthesized in house to fulfil the criteria required to support long-lived singlet order mentioned in the previous chapter. This molecular probe is characterized by a pair of coupled protons in a very symmetric environment, for them to be nearly magnetically equivalent.

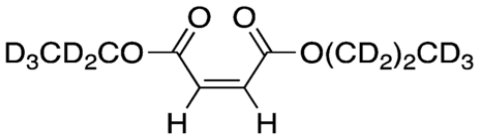

Figure 2.2 Structure of 1-(ethyl-d_5)4-(propyl-d_7)(Z)-but-2-enedioate (EPM)

2.1.3. Sample assembling and preparation

Each structure was placed in a 10 mm thick wall LPV NMR tube, together with 350 μL of a solution 0.5 M of EPM in acetone-d_6 99.96%. The bottom of the glass tubes was flattened and the total amount of solution was optimized to minimize the volume in which diffusion would have given an isotropic contribution. The sample containing the 00D structure was labelled Sample I and the sample with the 30D structure was labelled Sample II. Singlet spin order is very sensitive to paramagnetic oxygen which can dramatically reduce the relaxation constant T_S [24] For this reason, 10 cycles of freeze-pump-thaw were carried out on both samples, leaving the tube under low vacuum. In this degassing procedure, the tube containing the sample is immersed in liquid nitrogen and the atmosphere above the frozen liquid is vacuumed through the J-Young valve; the valve is then closed and the sample is let thaw at room temperature to allow oxygen to re-equilibrate the pressure in the tube, thus

escaping the solution; this is repeated multiple times to ensure the removal of the dissolved oxygen. This procedure was preferred to gas purging, in which the NMR tube is maintained open with inert gas bubbling from a capillary placed at the bottom of the solution [25]. This choice was motivated by the type of sample, consisting of a solid insert occupying most of the volume, with the solution only filling the channels and thus not allowing room for an effective purging through a capillary.

After the degassing, axial and sagittal MRI scans of the final samples were acquired to verify that the solution was evenly distributed within the channels (Figures 2.3 a. and b.).

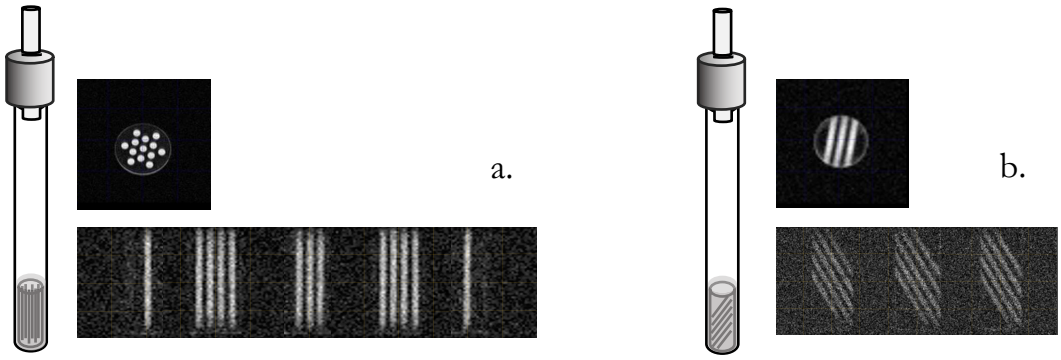

Figures 2.3 Drawings of samples I (a.) and II (b.) with respective MRI axial and sagittal images showing the channels filled with the probe solution.

University of Southampton

2.2. Experiments

2.2.1. T_1 measurement

T_1 value is among the basic parameters required to characterise a certain spin system. Specifically, the duration of T_1 is important in those pulse sequences where a pre-delay (or repetition time) is necessary for the magnetization to fully recover before the next experiment is started. Measurements of T_1 were carried out on both samples using Saturation Recovery pulse sequence described in 1.5.1, using saturation recovery experiment shown in Figure 1.12.

2.2.2. Singlet-assisted DTI experiments

2.2.2.1. The diff-M2S2M pulse sequence

Singlet order preparation was carried out using the pulse sequence in Figure 1.14 which had been modified to allow for diffusion measurement. This pulse sequence was previously developed in the group and applied for singlet-assisted measurement of diffusion along one direction (SAD NMR). According to what described 1.3.1, in order to sensitise the acquired signal to molecular displacement, two gradients of duration δ and separated by the diffusion time Δ, were applied along a specific

direction. The resulting pulse sequence is shown in Figure 2.4. The two blocks M2S and S2M separated by a delay T and a singlet filter, work exactly as in T_s measurement, but changes are introduced to store positional information.

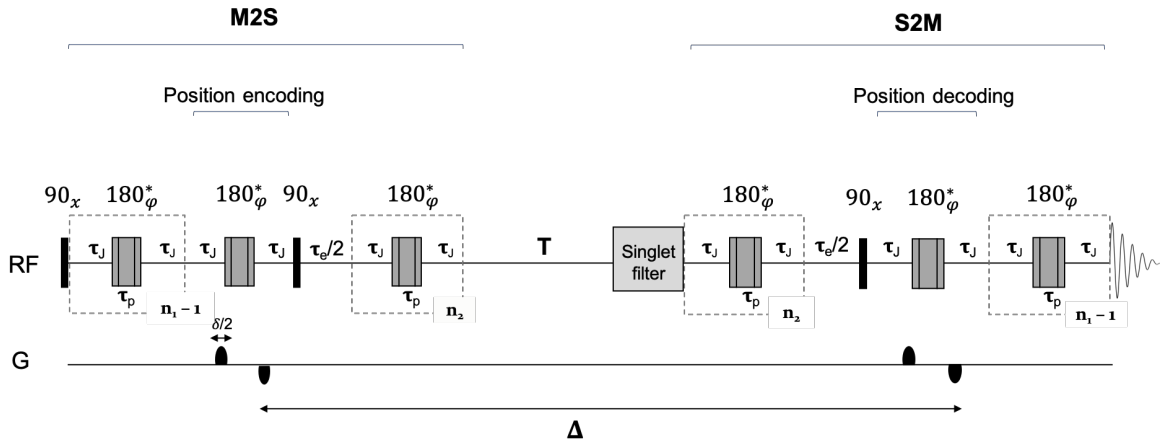

Figure 2.4 diff-M2S2M pulse sequence used to measure diffusion storing information on singlet spin order

One of the echoes of the first train was moved forward and became part of position encoding: the 180-degree composite pulse was placed in between the two opposite field gradient pulses of duration $\delta/2$. This is equivalent to a single gradient pulse of duration δ and it minimises the eddy currents created by magnetic field variation when a gradient is applied.

The rest of the sequence corresponds to the M2S2M, with the second block symmetric to the first one to convert singlet order into detectable magnetisation. A second couple of gradients decodes spins position after the time Δ, during which molecules diffused. Further experimental details are described below.

2.2.2.2. Data acquisition

The pulse sequence in Figure 2.4 was applied following the DTI experimental procedure for the measurement of one average diffusion tensor, resulting in a technique dubbed SADTI (singlet assisted diffusion tensor imaging). In order to observe the evolution of diffusion regime and observe the time-dependence of the diffusion profile (from unrestricted conditions to restricted conditions), 4 values of Δ were chosen to perform SADTI experiments: 1.5, 30, 120 and 240 sec; for each of those, one single diffusion tensor was derived for the whole sample. For a given Δ, the same experiment was repeated six times with a different gradient direction in order to calculate the six independent components of the diffusion tensor (see 1.4.3.2). Without any prior knowledge about the orientation of the tensor, the choice of the gradient directions was consistent with the idea of fully characterise diffusion, evenly in the three dimensions of space. To do this, the arrangement proposed by

Jones et al. [26] based on the analogy with the displacement of charges on a sphere to minimise electrostatic repulsion, was used Figure 2.5.

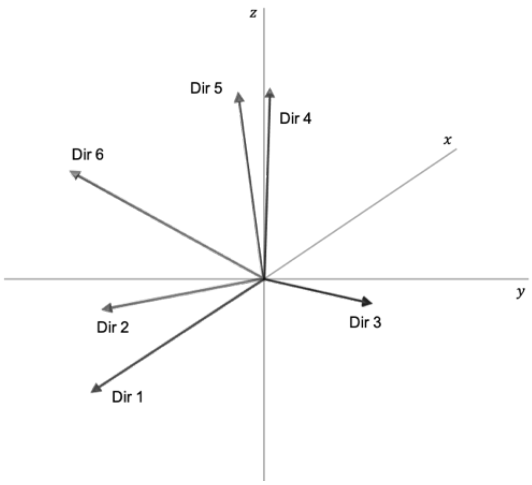

Figure 2.5 Directions of the gradients used to determine the 6 independent components of the tensor. Gradient vectors are distributed in space as 6 electric charges on a sphere need to be arranged to minimise repulsion [26].

The six gradient directions displayed in Figure 2.5 were all compositions of gradients along x, y and z-axis of the LAB-frame, obtained through a 3-axis gradient system and a Bruker MICWB40 micro-imaging probe equipped with a 1H/13C 10 mm resonator. The gradient intensity was expressed as percentage of the maximum gradient this system was able to deliver along each direction (1.5 T m^{-1}). For each direction, the intensity was gradually increased 8 times from a minimum to a maximum percentage, therefore collecting 8 acquired signals for each direction. The minimum gradient intensity was 1% in all the experiments, while the maximum

percentage was adjusted according to the Δ value (Tab. 1). This procedure was followed to increase the accuracy of the multivariate linear fitting of the data, as discussed in 1.4.3.2. The number of scans was also optimised depending on the diffusion time, in order to have a good signal-to-noise ratio when the experimental conditions led to a strong signal attenuation.

Table 1 Details of SADTI experiments for each diffusion time Δ used

Δ (s)	min gradient %	max gradient %	n° steps	n° scans
1.5	1	60	8	2
30	1	14	8	4
120	1	6.5	8	8
240	1	4.7	8	16

2.2.2.3. Data processing

For each gradient direction, a set of 8 attenuated signals was acquired, with an increasing attenuation due to the increasing gradient intensity. Each set was plotted and fitted with equation (63). For a given Δ, therefore, six equations were obtained and the resulting linear system was fitted to obtain the six elements of the diffusion

tensor. Figure 2.6 shows the example of one of the curves for Δ = 1.5 sec, relative to the gradient along the x-axis (Dir 1 in Figure 2.5).

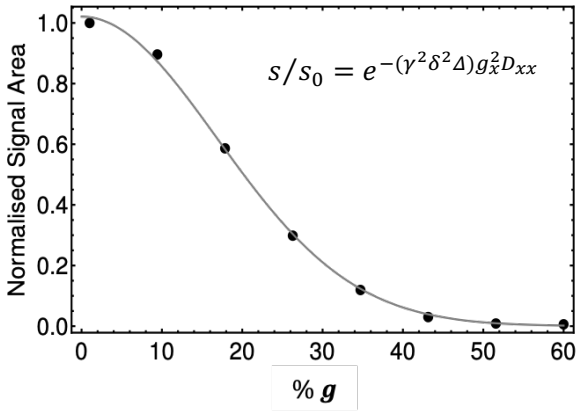

Figure 2.6 Example of experimental points obtained for $\Delta = 1.5$ sec and gradient direction = Dir 1. The fitting function was presented in equation (63) and the product $\mathbf{g}^T\mathbf{D}\mathbf{g}$ reduced to $g_x^2 D_{xx}$ because the gradient is exactly along the x-axis.

As discussed earlier, each gradient was delivered by producing its three components separately. The necessity of gradually increase each of these components to produce a resultant increasing gradient, made them subject to some errors and for this reason a calibration was needed. Gradient calibration was done assuming a perfectly unrestricted diffusion regime when using a Δ of 1.5 sec. As a consequence, the six curves obtained with this diffusion time were fitted using equation (63) expecting unrestricted diffusion and therefore the same scalar value of D along each direction.

Deviations from the expected result were used as a reference to correct the gradients until the D value was the same for all six directions.

For each diffusion time used, a diffusion tensor was calculated and diagonalized; its eigenvalues and eigenvectors were then used as lengths and directions of the corresponding ellipsoid. The value of FA was also calculated, together with the angle θ between the longest principal axis of the ellipsoid and the z-axis of the LAB-frame.

2.2.2.4. Error calculation

To calculate the error on all the values that were derived, a Monte Carlo approach implemented in a custom-made Mathematica notebook, was used. The procedure runs as follows:

1. The standard deviation on each of the six independent diffusion coefficients is extracted from the fitting routine (NonlinearModelFit routine in Mathematica);

2. A new diffusion tensor is built by randomly choosing a value for each of its six components which belong to the normal distribution centered at the parameter's best-fit value and whose standard deviation comes from point 1;

3. The new diffusion tensor is diagonalised and eigenvalues and eigenvectors stored in separate arrays;
4. The fractional anisotropy and the angle between the eigenvector corresponding to the larger eigenvalue and the z-laboratory axis is calculated and stored in separate arrays (any other quantity of interest can be derived in the same way);

5. Points 1-4 are repeated a number of time (N = 50,000);

6. The average and standard deviation of the arrays containing the N sets of eigenvalues, eigenvectors, fractional anisotropies and angles is finally computed. This returns the mean value of these parameters together with their estimated errors.

2.2.2.5. Worked example

A real case of work is summarised below as an example of the entire procedure.

University of Southampton

Acquisition

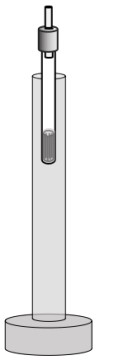

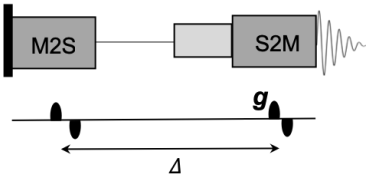

$\Delta = 1.5\ sec$

$g = 8\ intensities \times 6\ dirs$

SAMPLE I

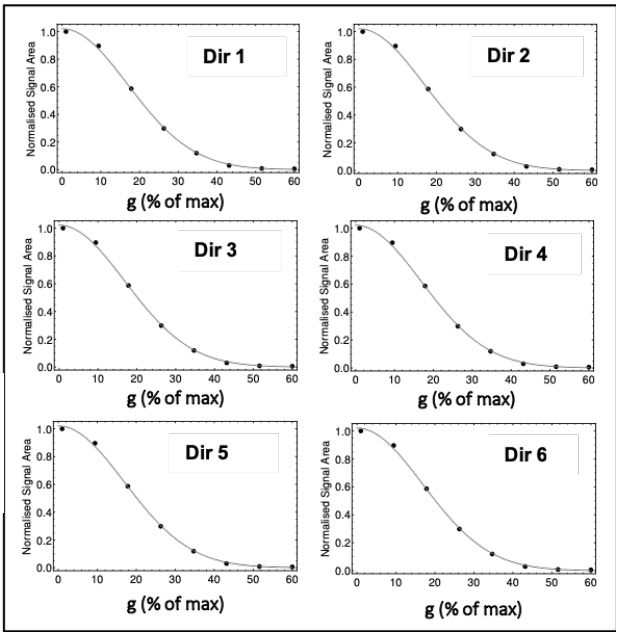

Processing

Each curve is fitted with equation (63) obtaining a combination of the elements of **D**

$$S/S_0 = e^{-(\gamma^2\delta^2\Delta)\mathbf{g}^{\mathbf{T}}\mathbf{D}\,\mathbf{g}}$$

The six equations lead to a linear system that is fitted by the computing system to obtain the diffusion tensor

$$\begin{pmatrix} 1.6\times10^{-9} & -3.4\times10^{-11} & -9.7\times10^{-12} \\ -3.4\times10^{-11} & 1.7\times10^{-9} & 1.5\times10^{-11} \\ -9.7\times10^{-12} & 1.5\times10^{-11} & 1.7\times10^{-9} \end{pmatrix}$$

The tensor is diagonalized and diffusion along eigenvector's directions is quantified by its eigenvalues

$$\begin{pmatrix} 1.55\times10^{-9} & 0 & 0 \\ 0 & 1.66\times10^{-9} & 0 \\ 0 & 0 & 1.77\times10^{-9} \end{pmatrix}$$

Eigenvalues and eigenvectors allow to infer the profile of diffusion and to express it numerically (FA) and graphically (diffusion ellipsoid)

Fractional Anisotropy

$$\mathbf{FA} = \sqrt{1 - \frac{\lambda_1\lambda_2 + \lambda_1\lambda_3 + \lambda_2\lambda_3}{(\lambda_1)^2 + (\lambda_2)^2 + (\lambda_3)^2}} = \mathbf{0.07 \pm 0.02}$$

Diffusion ellipsoid

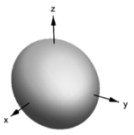

University of Southampton

2.3. Results

2.3.1. Relaxation times

Relaxation curves of longitudinal magnetization and singlet order are displayed below for sample I (Figure 2.7) and sample II (Figure 2.8), together with calculated decay constants T_1 and T_s for both samples. Data were fitted with equations (74) and (79) respectively.

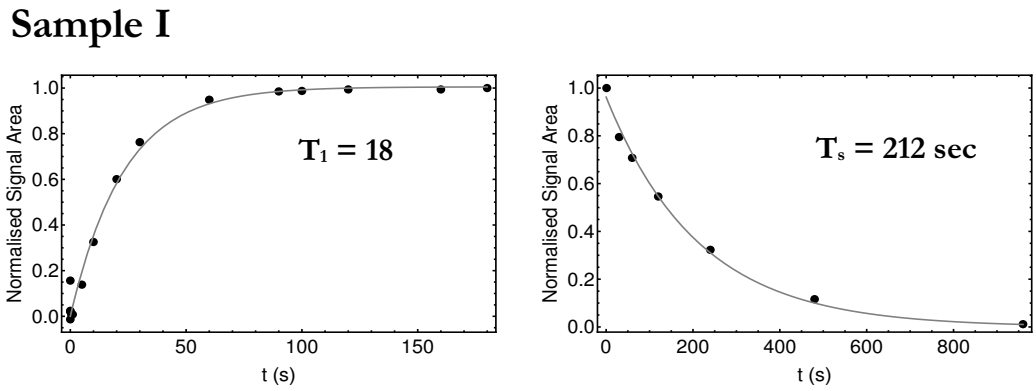

Figure 2.7 Relaxation decay curves and calculated constants of longitudinal magnetization (left) and singlet order (right) for Sample I.

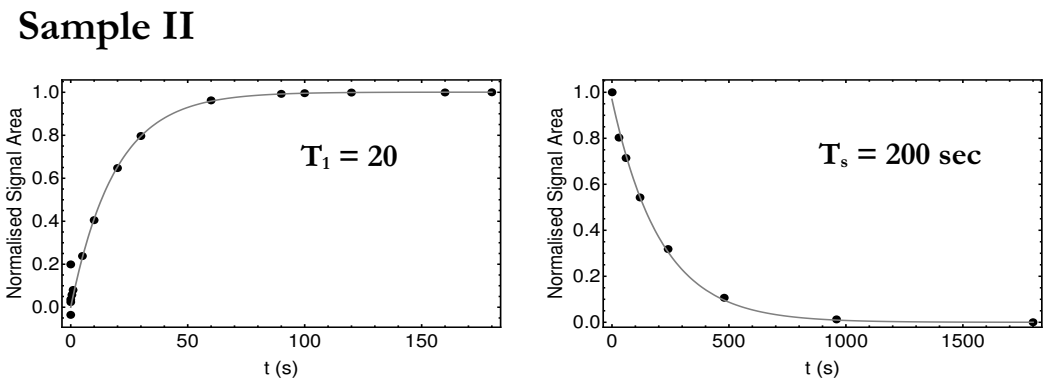

Figure 2.8 Relaxation decay curves and calculated constants of longitudinal magnetization (left) and singlet order (right) for Sample II.

Some of the acquired spectra are shown in Figure 2.9 and Figure 2.10. Figure 2.9 (a) and (b) are relative to Sample I and Sample II respectively. They were both acquired with a simple 90-degree pulse followed by acquisition. Therefore, all the ^{1}H spins present in the sample were excited, included the ones of the plastic material. In order to achieve a satisfactory line broadening, shimming automatic procedure was carried out to correct field homogeneity. Nevertheless, the spectrum in Figure 2.9 (b) appears to be of lower quality and this is probably due to channel inclination that made composition of Sample II less spatially uniform than Sample I. Lower efficiency in sample preparation might also be involved (air bubbles as a result of the degassing procedure, trapped in the structure due to channels

inclination). Figure 2.10 (a) and (b) show the spectra acquired after singlet-order preparation and selection by means of a filter.

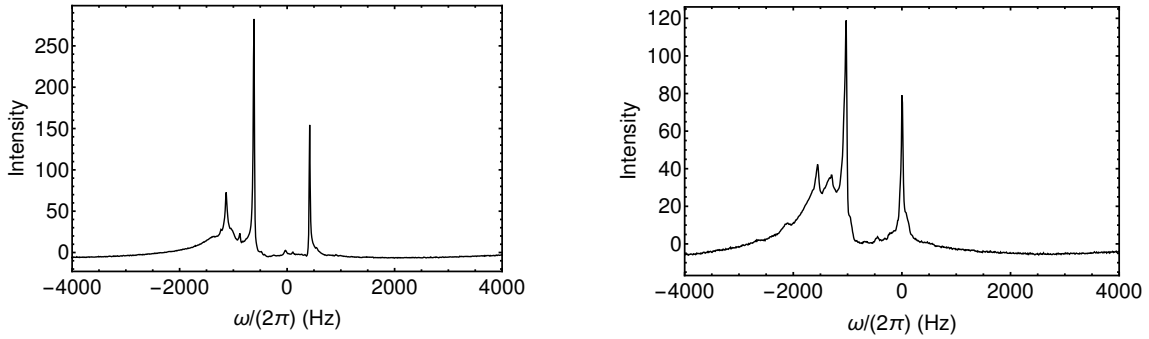

a. b.

Figure 2.9 Acquired spectra on Sample I (a) and Sample II (b) performing a simple 90-degree pulse followed by acquisition.

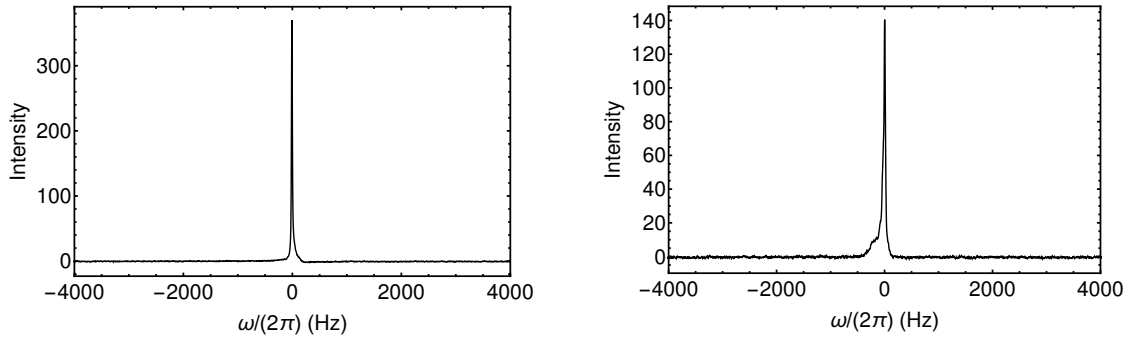

a. b.

Figure 2.10 Acquired spectra on Sample I (a) and Sample II (b) performing experiments with singlet order preparation and filtration.

University of Southampton

2.3.2. Diffusion tensor calculation

Table 2 shows the final results obtained from DTI experiments with both samples. For each diffusion time Δ and the corresponding root-mean-squared displacement (d_{rms}), the ellipsoid and the normalized fractional anisotropy (FA) are displayed. The value of θ, i.e. the angle between the eigenvector with the highest eigenvalue, and the z-axis of the LAB-frame, is also reported; the latter was calculated to evaluate the success of the technique in predicting the direction along which diffusion was unrestricted, i.e. the orientation of the channels. As it looks evident from the ellipsoids shape, DTI fails in revealing diffusion anisotropy when a short value of Δ is used, and thus no inner features of the structure can be inferred. Instead, these become evident when Δ increases: with a Δ of 4 minutes, shape and orientation of molecular displacement given by the ellipsoid match the geometry of channels in both samples. These ellipsoids appear to be slightly more flat than expected considering the cylindrical symmetry of the channels, and this might require further investigation; nevertheless, the presence and the alignment of a preferred direction of diffusion is evident and it was only observable thanks to the preparation of long-lived singlet spin order, which allowed to probe a d_{rms} up to $876\ \mu m$, thus leading to conditions of anisotropic restriction for the majority of the molecules in the sample. The results obtained with the longest diffusion times are

overall consistent with the architecture of the structures used, and within a reasonably small error. The acquisition of 8 points for each gradient direction made the experiments with long diffusion times quite time consuming, but it maximized the accuracy of curve fitting, consequently reducing the final error.

Table 2 Results of SADTI experiments. The shape of each ellipsoid derives from the corresponding tensor's eigenvalues, while the orientation reflects eigenvectors direction; FA is the fractional anisotropy, and θ is the angle between the eigenvector with highest eigenvalue and the z-axis of the LAB-frame.

		Sample I			Sample II		
Δ (s)	$d_{rms}(\mu m)$	**Ellipsoid**	**FA**	θ(°)	**Ellipsoid**	**FA**	θ(°)
1.5	70	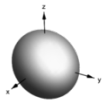	0.07 ± 0.02	51 ± 24	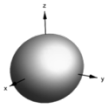	0.07 ± 0.02	36 ± 22
30	310	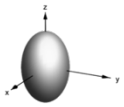	0.34 ± 0.05	6.4 ± 3.6	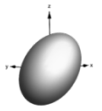	0.24 ± 0.03	27 ± 5
120	619	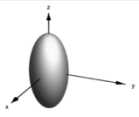	0.53 ± 0.01	1.3 ± 0.7	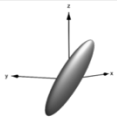	0.67 ± 0.06	29 ± 5
240	876	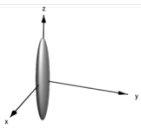	0.81 ± 0.02	2.2 ± 1.2	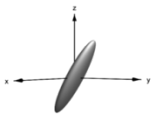	0.80 ± 0.03	31 ± 2

2.4. Conclusions

Diffusion occurring in restricted regime results in a diffusion tensor (and a corresponding ellipsoid) whose features reflect the surrounding environment. DTI routinely derives diffusion ellipsoids for each voxel in images obtained on samples where molecular motion appears restricted, even when a very short diffusion time is used. To observe diffusion in a restricted regime on timescales longer than usual, spin relaxation effects must be bypassed. In this study, preparation of long-lived singlet spin order allowed to reach relaxation times of over 200 seconds, extending the maximum temporal (and, therefore, spatial) length diffusion can be observed for. Singlet spin order preparation was combined with the DTI approach, and one average diffusion tensor was derived for macroscopic structures that are out of the reach of conventional DTI procedures. This methodology was validated using an in-house synthesised molecular probe, diffusing in structures with a known internal architecture, that was successfully re-inferred from the acquired data. Although the molecular probe used was not verified as bio-compatible, this study allowed to show that combination of singlet order preparation and DTI technique is feasible and paved the way to applications in the bio-medical field; as will be extensively described in Chapter 4, non-invasive characterization of complex samples relevant

to the field of tissue engineering was successively considered as a possible application.

University of Southampton

3. Single-scan T_s measurement

This chapter describes the principles and results of another fortunate combination of pulsed field gradients and singlet order preparation. The use of SADTI described in Chapter 2, requires that the T_s of the molecular probe in use is known, in order to determine the upper limit to the diffusion time Δ that can be set and therefore the distance that can be scoped. As described in section 1.5.4, conventional T_s measurement is not a complex procedure in that is conceptually equivalent to T_1 measurement, where the spin order is repeatedly prepared and let decay over a list of variable delays (VD). This list needs to be long enough in order to collect an amount of points that allow to display the relaxation final plateau, and can be accurately fitted to determine the decay constant. As a consequence, the measurement of very long relaxation time automatically involves much longer VD lists, leading to very time-consuming experiments. Furthermore, due to the high susceptibility of singlet order relaxation time to dissolved paramagnetic oxygen, the sample is always degassed prior to be analysed; in such conditions, longitudinal relaxation time T_1 has shown a considerable increase as well [25]; this reflects on the repetition time that needs to be set when multiple experiments are carried out in a row, which adds up to the VD list length, leading to experiments that can last many

hours. These aspects motivated the development of a faster T_S measurement procedure where the sample is transversally "sliced" by selective excitation pulses: in this experiment, singlet order preparation is incorporated in a proper one-dimensional imaging pulse sequence, where gradient pulses are placed during both irradiation and acquisition. As previously discussed in Chapter 1, a shaped radio frequency (RF) pulse sent on a sample where a distribution of precession frequencies has been created, makes possible to excite a selected portion of the sample, i.e. to "slice" it. If another pulsed gradient is sent during the acquisition, the signal becomes position-dependent and the intensity is a function of the location within the sample region. If this is done along one specific direction of the laboratory frame, the resulting spectrum is a profile of the sample along that direction, therefore representing a 1D image of it.

The combination of this procedure with singlet order preparation pulse sequence M2S2M showed Figure 1.14. has a significative effect on the duration of singlet decay constant measurement. In fact, once that singlet order has been created in one slice, the shaped RF pulse can be sent with a different offset to excite a different region, while the spin order prepared in the previous slice starts to decay. This is repeated multiple times along the sample, until the entire coil region is scanned. Then, the acquisition is carried out in a non-selective fashion and the position-

dependent signals are acquired in magnitude mode. As a result, the last excited slice will be represented in the spectrum by the less decayed signal, while the first slice will be represented by the more decayed signal, and all the slices in between will show a gradual increase of intensity which can be fitted to report on the relaxation constant.

During this part of the study, this procedure was validated and the results were published in [27] and are described in the present chapter. The effect of phenomena such as molecular diffusion and thermal convection occurring in the solution is also described. Indeed, similarly to the case of SAD-NMR methodologies previously discussed, molecular diffusion played a substantial role in motivating the validation of this single-scan T_s measurement. This is due to the fact that the process of slicing implies the definition of well delimited regions, which are supposed to be excited at very specific moments during the pulse sequence. Molecular motion interferes with the separation of subsequent slices, since molecules can cross the sample longitudinally therefore being found, at the moment of acquisition, in a different slice far from where they were originally excited. This reflects on the resulting spectrum where each slice includes a contribution from spins that were supposed to be found in a different region, causing undesired line-broadening and loss of resolution of the sliced sample profile. As will be shown in the results, it appears

that thermal convection significantly imposes on diffusion, which is a random and much slower motion. Different strategies to eliminate the effect of convection were attempted, including the most effective one, where a designed plastic structure was placed inside the NMR tube to physically delimitate the regions filled with the solution, and therefore prevent the slices to merge. The results are described together with the insights these experiments provided.

3.1. Material and methods

3.1.1. Samples

Four samples were analysed: a solution 0.5 M of EPM (see Figure 2.2) in ethanol-d_6 was prepared and NMR experiments were carried out in three LVP NMR tubes of 10, 5, and 3 mm cross section respectively; the fourth sample was obtained as a 0.5 M solution of the same molecule in acetone-d_6, transferred in a 10 mm LVP NMR tube where an insert made of a solvent-resistant plastic (polyoxymethylene, or POM) was placed. The structural details of the insert are reported in Figure 3.1 (a). For the first three samples, the use of three different tube diameters was intended to investigate the effect of convection on the selectivity of the slicing process. The plastic rod in the fourth sample was added to verify if having 1 mm splits filled with

the solution and separated by 1 mm thick plastic gaps, could physically prevent any translational motion of molecules from a slice to the adjacent one. Table 3 summarises the composition of the four samples.

Table 3 Specifications of the four samples prepared to test single-scan T_s measurement procedure and to verify the effect of convection on the resulting spectra.

name	tube diameter (mm)	solvent	conc. (M)	plastic insert
S_{10}	10	ethanol-d_6	0.5	NO
S_5	5	ethanol-d_6	0.5	NO
S_3	3	ethanol-d_6	0.5	NO
S_{POM}	10 + POM	acetone-d_6	0.5	YES

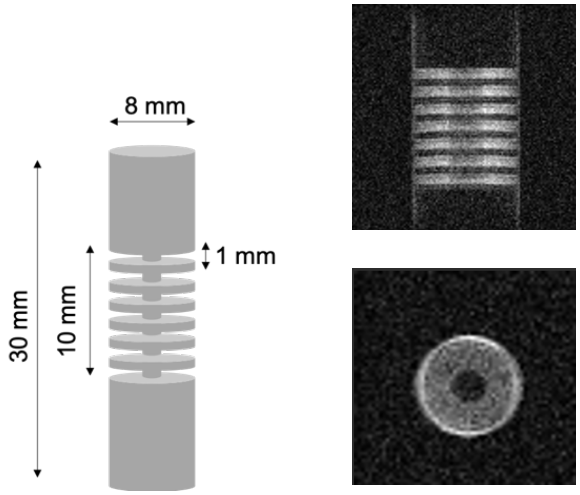

a. b.

Figure 3.1 a. graphic representation of the plastic insert used to reduce convection; **b.** MRI scans of the tube containing the solution and the plastic insert.

All experiments were run on a 7.04 T magnet coupled to a Bruker Avance III console fitted with a 3-axis gradient system for micro-imaging experiments able to deliver a maximum field gradient of 1.5 T m-1 and a Bruker MICWB40 microimaging probe equipped with a 1H/13C 10 mm resonator. The degassing procedure necessary to remove paramagnetic oxygen was carried out in all four samples: S_{10}, S_5 and S_3 were all degassed through inert gas purging carried out for 5 minutes using a capillary bubbling from the bottom of the solution. Due to the presence of the plastic insert, S_{POM} was instead degassed using the freeze-and-thaw procedure described in 2.1.2.

3.1.2. Shaped pulse optimisation

Many shaped pulses are available which allow to target a well-defined portion of the sample during selective excitation. Figure 3.2 shows the comparison of three different RF pulses as functions of time, with the corresponding excitation profile obtained through Fourier transform. It is possible to notice how different functions allow different precision when defining the range of frequencies to be excited, providing a different control of the excitation that occurs outside the region of interest.

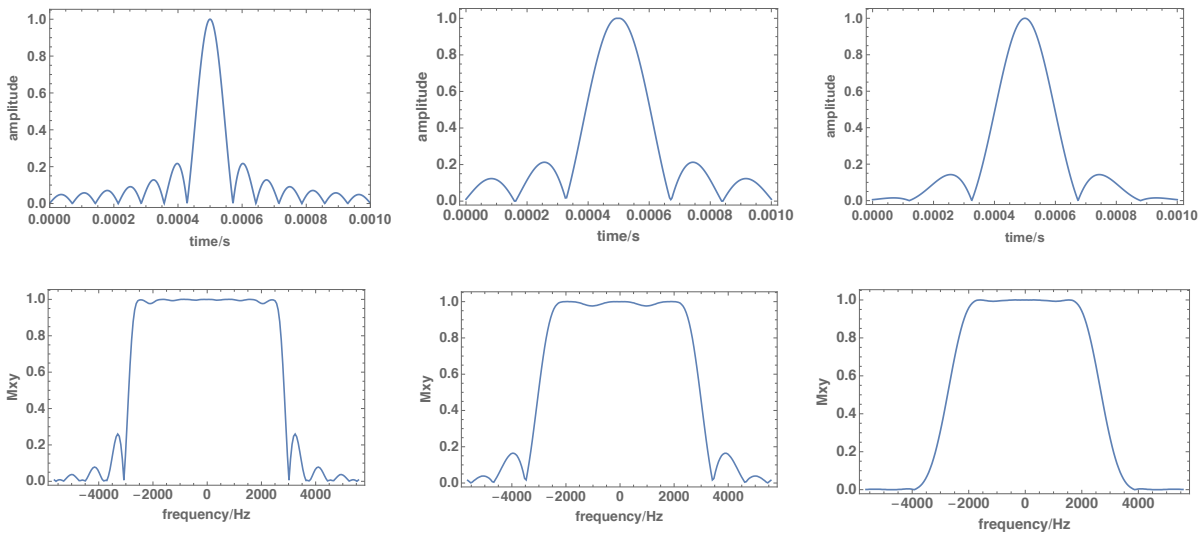

Figure 3.2 Shaped pulses tested for the selective excitation: **a.** Sinc7 pulse in the time domain (top) and corresponding excitation profile; **b.** Sinc3 pulse in the time domain (top) and corresponding excitation profile; **c.** Shinnar-Le Roux (SLR) shaped pulse (top) and corresponding excitation profile. Each excitation profile was obtained through the Fourier Transform of the pulse in the time domain, and it is expressed as fraction of magnetization created on the x-y plane. The picture shows, from left to right, the increased precision at the edges of the excitation profile.

The requirement of an accurate selection with no excitation occurring outside the desired region had to be combined with the need of not too intense currents, in order to avoid overheating that might lead to temperature gradients and consequently to further thermal convection. The function SLR (Shinnar-Le Roux [28]) was chosen as the best fit for purpose because provides a neat excitation profile with less power.

The duration of the selective 90-degree and 180-degree pulses were set according to the chosen bandwidth $\Delta\omega$ of 9 kHz. In order to calculate the power needed for an exact 90 and 180 flip-angle, Topspin simulator was used: once that the shape was set to the desired function, and the duration of the pulse was specified as the one corresponding to 9 kHz of bandwidth, the simulation provided the maximum pulse amplitude γB_1 necessary to make the area under the curve the same as the non-selective 90-degree pulse previously used and optimised. The conversion of this value into power (measured in Watt) is done by the software, considering the specifications of the instrument. Table 4 reports on the details about the pulses used in the experiments described in this section.

Table 4 Optimised parameters for the high-power excitation, the shaped excitation and the shaped refocussing pulses. The corresponding range of excited frequencies is also reported.

Pulse	**Shape**	**Duration (μs)**	**Power (W)**	**Bandwidth (kHz)**
non-selective 90	rectangular	10	95	100
shaped 90	SLR	590	1.06	9
shaped 180	SLR	635	18.75	9

3.1.3. Pulse sequence

As thoroughly discussed in Chapter 2, when the sample is an ensemble of nearly-equivalent coupled spin pairs, singlet state can be populated by using special echo trains that are synchronised with the J-coupling constant of each isolated spin pair. As previously seen, in traditional T_s measurement, the M2S block is followed by a delay T during which singlet order starts decaying. At the end of this delay, the same block reversed in time (called S2M) is then applied to the ensemble in order to transform singlet order into detectable magnetization whose signal can be acquired. In traditional T_s measurement, this procedure is repeated multiple times with a different delay T, and a list of signals is collected to be fitted with the suitable function. The entire duration of this experiment depends on the expected T_s and it can be estimated as

$$3\mathrm{n}T_1 + \sum_{i=1}^{\mathrm{n}} d_{v_i} \tag{80}$$

where n is the number of experiments (i.e. the number of variable delays in the list), T_1 is the longitudinal magnetization decay constant to be waited before each new experiment of the list (pre-delay) and d_{v_i} is the duration of the i^{th} variable delay expressed in seconds. As the goal of singlet order preparation is usually to exploit

its longer decay, a drawback of T_s measurement is a longer duration of the experiment, which can require a few hours. In order to perform a faster T_s measurement, the pulse sequence in Figure 1.14 had to be modified to make the singlet order preparation selective for specific sections of the sample region. This was achieved by exploiting the interplay of pulse field gradient and shaped RF pulses.

Figure 3.3 a. and b. show the selective M2S block (dubbed sM2S) of the modified pulse sequence, compared with the unmodified block presented in Chapter 2.

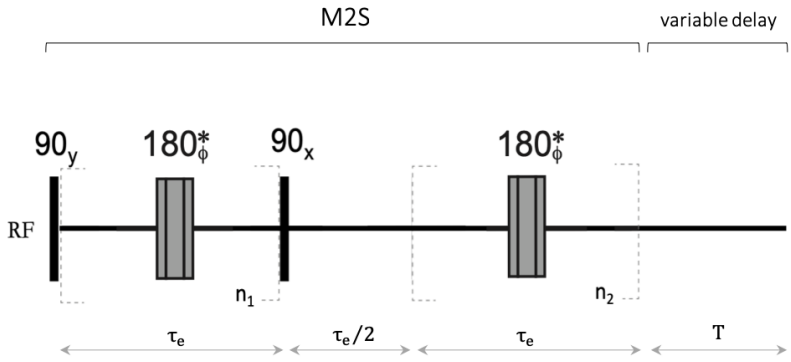

a.

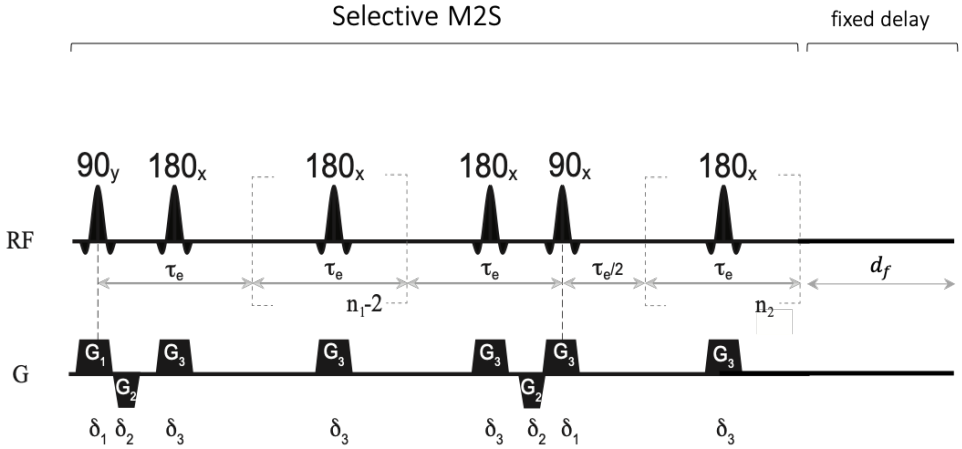

b.

Figure 3.3 a. Non-selective M2S block used to prepare singlet order in the whole coil region. * indicates a composite 180° pulse built as $90_x180_y90_x$ and with overall phase ϕ cycled within each echo train as $[x, x, \bar{x}, \bar{x},\ \bar{x}, x, x, \bar{x}, \bar{x}, \bar{x}, x, x, x, \bar{x}, \bar{x}, x]$; the block is followed by a variable delay T which can be incremented in subsequent experiments to derive the relaxation profile, as described in 1.5.3. **b.** Selective block sM2S used in single-scan T_s measurement. The duration δ_1 is set equal to the length of the 90-degree selective pulse. The gradient G_2 has equal but opposite strength to G_1 whereas the duration δ_2 is adjusted so that the total area of G_2 is equal and opposite to the area of G_1 so to cancel the phase distortion induced by G_1 during the selective excitation. The gradient G_3 makes the 180-degree pulses space selective; the intensity G_3 is set equal to G_1 while the duration δ_3 is adjusted to match the length of the 180-degree shaped pulse. This block is followed by a fixed delay d_f that does not need to be incremented to observe a relaxation decay (see text).

Analogously to the conventional T_s measurement, the sM2S block is followed by a delay during which the slice where singlet order has been created can start its decay. However, differently from the non-selective M2S block, this delay, here called d_f, is fixed. In fact, d_f does not need to be increased, as each excitation is carried out on a different portion of the sample while the previous ones are still decaying, and therefore the time for the i^{th} slice to decay naturally changes with the proceeding of the scanning, according to $d_f + (n - i)d_f$ where n is the total number of slices the sample has been divided. At the end of the series, the selective pulses have scanned the entire length of the sample. The overall duration of this experiment corresponds to $n\, d_f$. It is important to notice that no repetition time is necessary, as the same region is never excited twice. Each slice can continue its decay while the subsequent one is excited, so that, at the end of the series, the slice that was excited first has relaxed for nd_f seconds while the last one has relaxed for d_f seconds only. This way, the list is created in one single experiment instead of repeating the same experiment multiple times on the whole sample. Once that the sample has been sectioned in singlet-bearing slices, a gradient-based filter is applied to de-phase any residual magnetization and allow singlet order only to reach the singlet-to-magnetization (S2M) block; S2M block is applied to the whole coil region in a non-selective fashion, so that the decaying singlet order in all slices is converted to

magnetisation simultaneously. Finally, during acquisition, gradient pulses are also used but with a different purpose compared to the gradients used during excitation: in order to create a 1D image of the sample, the signal acquired needs to be collected and displayed as a function of the position along the z-axis of LAB-frame. This is done by applying a z-oriented gradient during the acquisition, with an intensity that has been adjusted according to equation (25) so that the overall section Δz corresponds to the entire coil region. The resulting block is dubbed SEI (spin echo imaging). Figure 3.4 summarises the last two blocks of the pulse sequence (S2M and acquisition through SEI) described above.

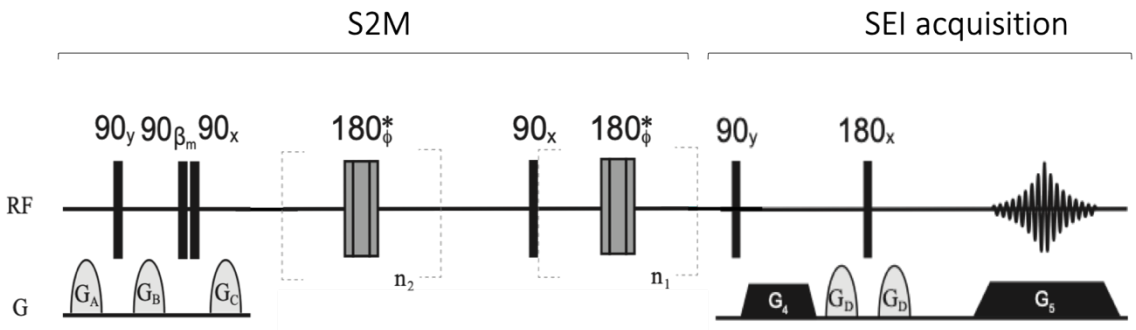

Figure 3.4. The non-selective S2M block (plus initial filter) is the M2S reversed in time. The filter is placed before the S2M to exclude possible by-products and allow pure singlet order to reach the conversion to magnetisation. S2M block is followed by the spin echo imaging (SEI) acquisition, where $G_5 = 2G_4$. The entire echo is carried out in the presence of a gradient in order to compensate the de-phasing effect of G_5 during the acquisition.

The resulting pulse sequence was dubbed sM2S2M-SEI (selective M2S2M spin echo imaging), and will be referred to as such throughout this chapter. Figures 3.5 (a) and (b) summarise the difference between the conventional variable-delay T_s measurement and the slice-selective T_s measurement; each block in both sequences has been simplified to highlight the concept of variable delay T and fixed delay d_f.

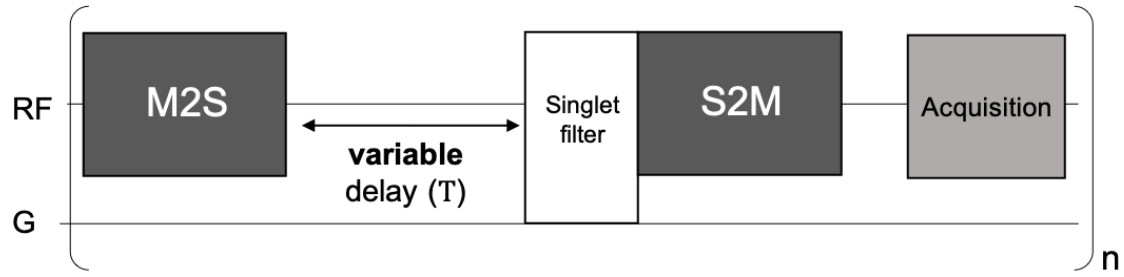

a.

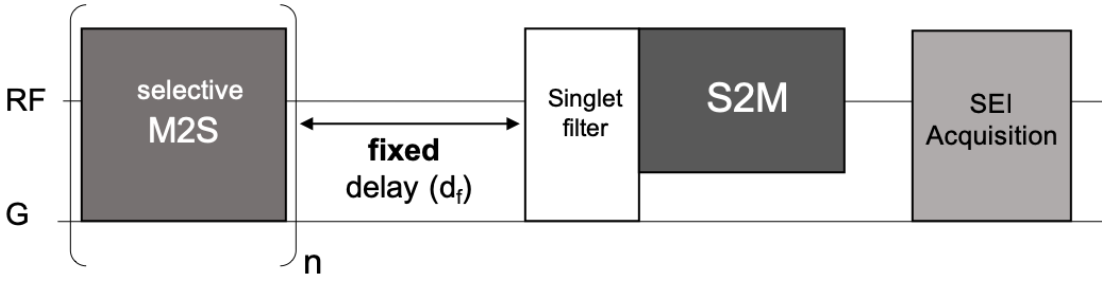

b.

Figure 3.5 a. Overview of the pulse sequence used in conventional measurement of T_s, where a list of experiments is carried out with different variable delays T (see section 1.5.3 for details); **b.** overview of the pulse sequence used in the single-scan experiment; selective M2S block is described in details in Figure 3.3 b.; S2M and spin-echo imaging (SEI) acquisition block are described in detail in Figure 3.4.

In all samples, seven slices were selectively excited. Seven different offsets were set in such a way that the centre of each excitation was distant $1.7\ mm$ from the next one in samples S_{10}, S_5 and S_3. The offsets for sample S_{POM} were chosen in order to coincide with the centre of the gaps in the plastic insert. The parameters used for singlet order preparation as well as the gradient intensities used during excitation and acquisition, are reported in Table 5.

Table 5 Optimised parameters for singlet order preparation and gradient strengths set in the selective block (G_1, G_2, G_3) and in the spin echo imaging block (G_4, G_5). In the sample S_{POM} it was possible to excite a larger section, thanks to the insert that limited the errors of an inaccurate slicing.

sample	n_1	n_2	τ_e (ms)	G_1, G_2, G_3 (mT m^{-1})	G_4, G_5 (mT m^{-1})	Δz (mm)
S_{10} S_5 S_3	18	9	41.8	420	75	0.5
S_{POM}				180		1.2

Variations of sM2S2M-SEI pulse sequence were also used, including M2S2M-SEI, a non-selective pulse sequence where singlet is prepared in the entire coil region and re-converted to magnetization providing a complete 1D singlet-profile of the whole sample; the pulse sequence dubbed SEI solely consisted of the block presented in Figure 3.4, where no selective pulse and no singlet order preparation is carried out and the spectrum is a simple 1D image of transverse magnetization. The profiles of

both singlet order and magnetisation were important to assess the amount of singlet that was possible to obtain compared to the transverse magnetisation, and were also used as a reference to choose the position and the thickness of the slices before carrying out the selective experiments.

University of Southampton

3.2. Results and discussion

T_s measurement was firstly carried out following the conventional procedure. The values obtained for each sample are reported in Table 6 together with the corresponding T_1.

Table 6 Relaxation time constants for longitudinal magnetization and singlet order for the four samples. T_s values here reported were measured with the conventional procedure. Samples S_{10}, S_5 and S_3 were prepared in ethanol-d_6, while sample S_{POM} was prepared in acetone-d_6.

sample	T_1 (sec)	T_s (sec)
S_{10}	10.1 ± 0.2	174 ± 3
S_5	10.0 ± 0.3	259 ± 7
S_3	9.8 ± 0.3	283 ± 7
S_{POM}	18.1 ± 0.2	208 ± 6

Discrepancies in the values can be ascribed to differences in the conditions of sample preparation, such as the degassing procedure. If samples S_{10}, S_5 and S_3 are compared, T_s seems to increase with the decrease of the tube diameter. This can be justified with the reduced volume above the solution in thinner tubes, which result easier to saturate with inert gas, or to vacuum when the freeze-thaw process is carried out. S_{POM} sample was prepared in a 10 mm tube but was the only sample in acetone-d_6, and despite showing a higher T_s compared to S_{10}, a much longer value was

expected due to the lower viscosity of the solvent [25]. In fact, the longer T_1 in $\mathbf{S_{POM}}$ clearly shows the effect of the solvent's lower viscosity. For T_s in $\mathbf{S_{POM}}$, the effect of the larger tube diameter compromising the degassing procedure seems to prevail on the solvent effect, and it could be further exacerbated by the presence of the solid insert which hinders the movement of gas bubbles from the bottom of the solution. This could explain why $\mathbf{S_{POM}}$ presents a T_s only slightly higher than $\mathbf{S_{10}}$ and still lower than the other samples prepared in ethanol-d_6. Nevertheless, in this case the focus was not on obtaining the longest T_s achievable but rather to verify that the value obtained through the single-scan experiment resulted comparable to the one obtained through the conventional experiment based on a variable-delay array.

Figure 3.6 shows the 1D profiles obtained on the sample $\mathbf{S_{10}}$ with the use of non-selective pulse sequences. Figures (a) and (b) display the profiles of magnetisation and singlet order obtained with SEI and M2S2M-SEI pulse sequences respectively. The amount of singlet order appears to be slightly lower than the $2/3$ expected from theory [29]. $\mathbf{S_5}$ and $\mathbf{S_3}$ provided analogous results, although requiring a larger number of scans to obtain a comparable signal-to-noise ratio, due to the reduced amount of sample present in the coil region.

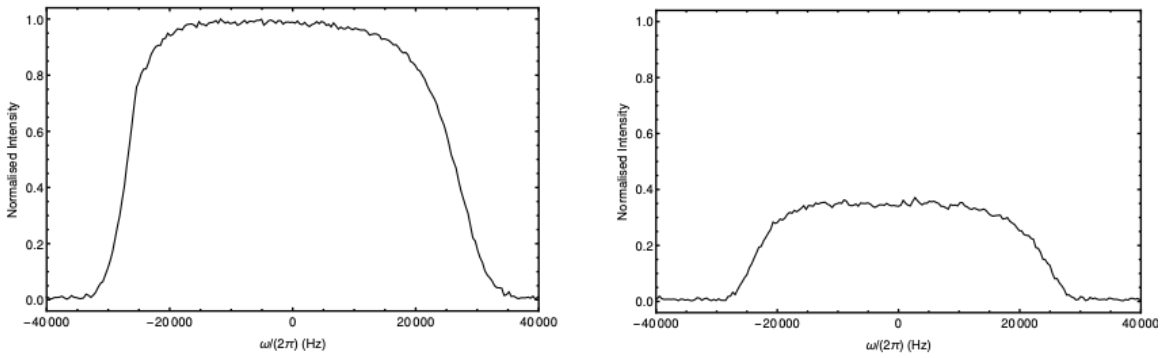

a. b.

Figure 3.6 a. Magnetisation profile obtained with the pulse sequence SEI; **b.** singlet order profile obtained with the pulse sequence M2S2M-SEI. Both spectra were acquired on the sample S_{10} with one scan; the difference in intensity is due to the loss of magnetization inherent in the conversion of longitudinal order into singlet order; the width of both spectra reflects the extent of the whole coil region: the range of frequencies each spectrum is comprised of, and the thickness of the coil region ($\sim$20 mm), are linked through the applied gradient as stated in equation (25).

Figure 3.7 shows the results for the sample containing the plastic insert S_{POM}. The magnetisation and the singlet order profiles are displayed in a. and b. respectively. The separation realised by the splits filled with the solution is evident, but Figure 3.7 a. shows that a contribution from outside the slices is also present. It is reasonable to believe that the protons present in the plastic resonated during the SEI sequence, as the overall width of the signal is compatible with the length of the insert as shown in Figure 3.1 (a); indeed, no contribution is observed in Figure 3.7 (b), were the signal has been filtered and only singlet order generated by the singlet-bearing spin system is detected.

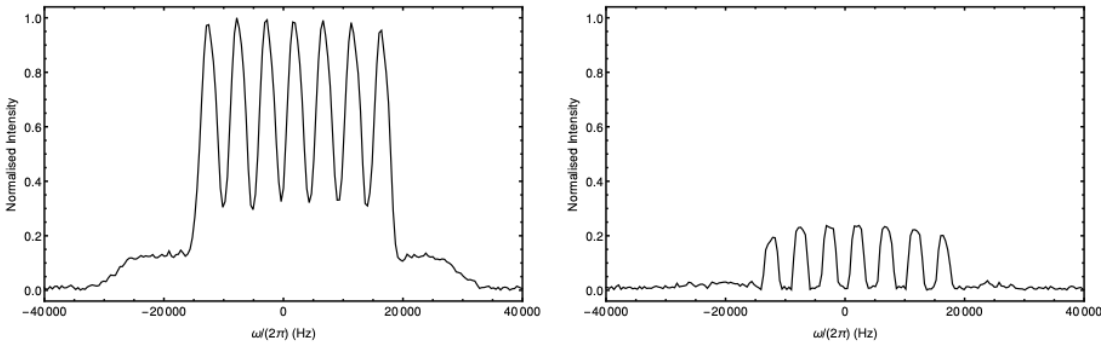

a. b.

Figure 3.7 a. Magnetisation profile obtained with the pulse sequence SEI; **b.** singlet order profile obtained with the pulse sequence M2S2M-SEI. Both spectra were acquired on the sample S_{POM}

In Figure 3.8, the results of all the selective experiments carried out on sample $\mathbf{S_{10}}$ are presented. Each spectrum of the series was acquired with a different value of the fixed delay d_f placed in between the selective block sM2S and the non-selective block S2M (see Figure 3.5 b.). The intensity of all spectra was normalised to 1 to better appreciate the comparison. It is evident how the definition of the slices worsens with the time allowed for the singlet order to decay (i.e. d_f increases): not only molecular motion promotes the mechanisms responsible for the loss of spin coherence, but it also transports molecules across the sample, thus affecting the separation that the selective pulses are intended to create. In fact, spins located in a slice that has been selectively converted into singlet order can travel across the

sample until they reach a different slice; consequenlty, at the moment of acquisition, spins excited in a section of the sample with a specific Larmor frequency will be found in a different region, resulting in the broadening of the slice they originally belonged to. This effect becomes more evident with the increase of the time d_f, which in turn allows more time for the spins to travel across the coil region ultimately merging the signal from different slices. The loss of intensity primarily due to relaxation can be appreciated by focusing the attention on the signal from the slice that was excited last in each series (first slice on the left in each spectrum of Figure 3.8). In each spectrum, this slice was excited right before the acquisition and only had d_f to relax (equation (80) with $i = n$). Therefore, this slice is the least affected by molecular motion and can be used to qualitatively estimate relaxation. In the experiment with $d_f = 0\ sec$ (Figure 3.8 (a)) the last excited peak at about -16 kHz could solely relax for the duration of one pulse sequence; in Figures 3.8 (b),(c), and (d) the same peak had the time to decay for a d_f equal to 10, 30 and 60 seconds respectively. Although molecular motion can play a part in the peak broadening, this peak is the most representative of the loss of signal due to singlet order relaxation.

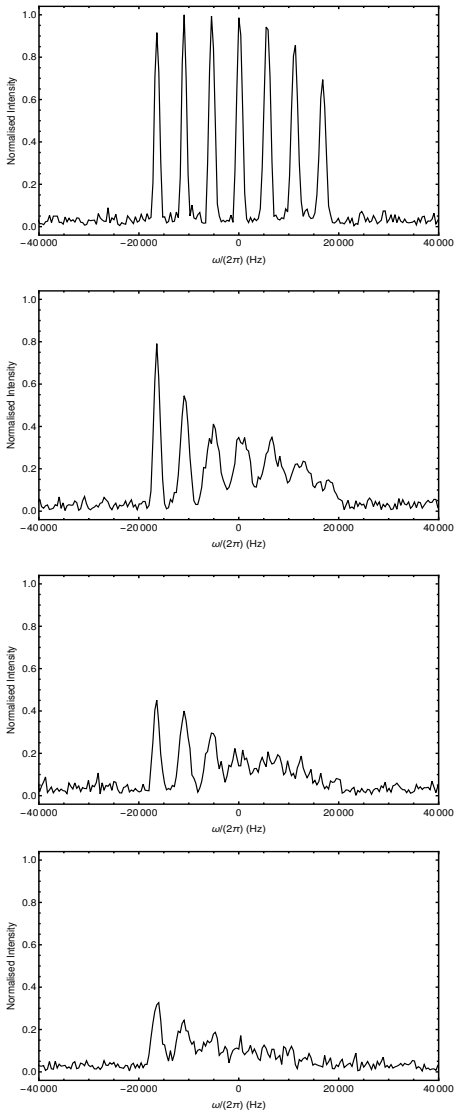

(a) $d_f = 0\ sec$

(b) $d_f = 10\ sec$

(c) $d_f = 30\ sec$

(d) $d_f = 60\ sec$

Figure 3.8 Results obtained on sample S_{10} with selective pulse sequence sM2S2M-SEI. Different d_f in between sM2S and S2M blocks were used (see Figure 3.5 b.). In each spectrum, first peak on the right was excited first and it is the most influenced by molecular displacement (see text); this effect results in peak broadening and increases with the increase of d_f; first peak on the left was the last to be excited in each series and therefore the least affected by displacement, as the time available for the spins to migrate to different slices was minimised. Intensity was normalised to 1 to appreciate the comparison.

The effect of diffusion was considered as a possible cause of the loss of definition. However, the measurement of the diffusion coefficient D carried out through traditional PGSTE pulse sequence resulted in a value of $7 \cdot 10^{-10}\ m^2/s$. Through the use of equation (1), it was possible to derive the average distance travelled by the molecules, which resulted in $d_{rms} = 0.3\ mm$ when considering a time interval $\Delta = 70\ sec$. This value of Δ corresponds to the time available for the first excited molecules to diffuse in the experiment with $d_f = 10\ sec$. Although not very far from the thickness of the slice ($0.5\ mm$) this value is not sufficient to justify the observed merging of the slices showed in Figure 3.8 b.

The results obtained from the four samples with a d_f set to $10\ sec$ are shown in Figure 3.9. Each spectrum was obtained using the pulse sequence sM2S2M-SEI. These results also clarify the reason why different tube diameters were used and compared: thermal convection in solution is known to depend on the dimensions of the vessel, as these in turn determine the entity of the temperature gradients, which represent the driving force of convection itself. Considering the cylindrical shape of the sample, it is to be expected that the z-axis represents the main direction of convection. However, it is also well known how the diameter of the tube has a role in determining the entity of convection [30]. Experiments presented in Figure 3.9

confirmed that, by reducing the diameter of the tube, the interference of longitudinal motion crossing the sample through the different sections is reduced, thus allowing a better resolution of the slices. The result obtained with the POM insert acting as a physical barrier for such motion is also shown. Indeed, this represented the most effective alternative to appreciate the selectivity of singlet order preparation.

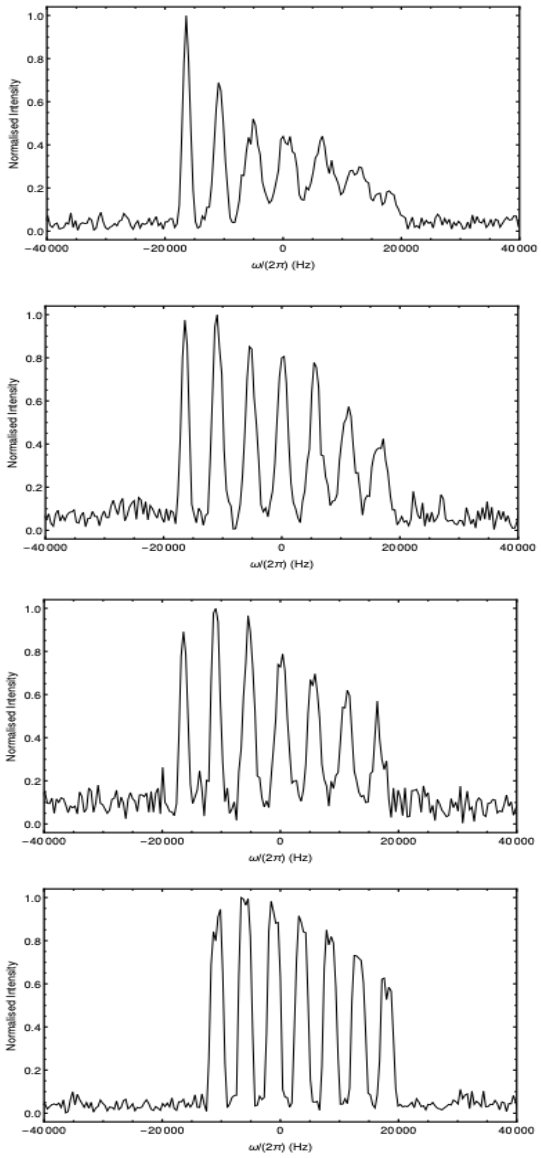

(a) Sample S_{10}

(b) Sample S_5

(c) Sample S_3

(d) Sample S_{POM}

Figure 3.9 Results obtained on the four samples with the selective pulse sequence sM2S2M-SEI, where a fixed delay of 10 sec was used between the sM2S and the S2M blocks. The best resolution is obtained when convection is inhibited by the POM insert (d). Signal intensities were normalised to 1 to appreciate the improvement in resolution.

Once determined the effect of convection on the efficiency of the slicing process, the sM2S2M-SEI experiment was carried out on sample $\mathrm{S_{POM}}$, which had shown to mitigate this effect. The results obtained with different values of the delay d_f are reported in Figure 3.10. Differently from the series shown in Figure 3.8, where the sample with the larger diameter $\mathrm{S_{10}}$ was used, the plastic insert allowed to push the delay to $60\ sec$ without losing resolution in the slices. The loss of intensity only depends on singlet order relaxation, as it is desired for the calculation of the relaxation constant.

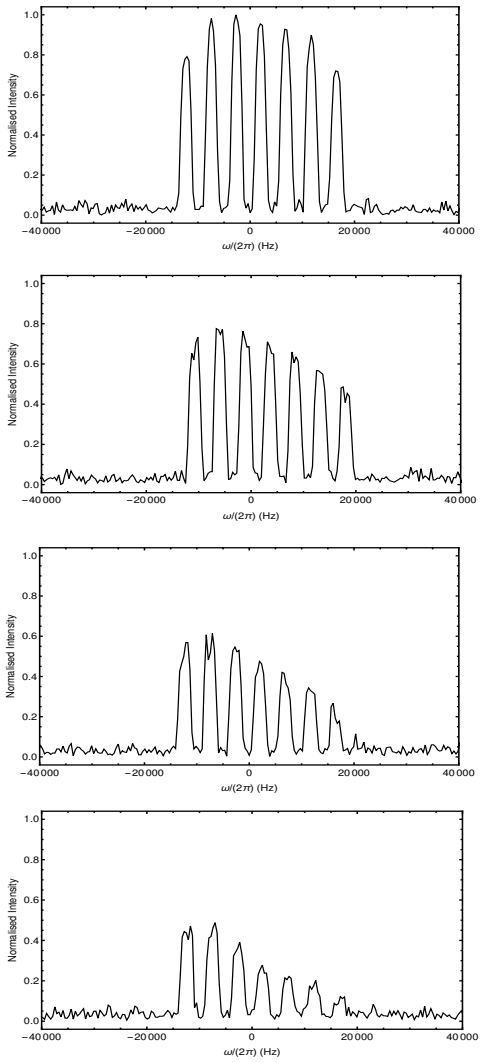

(a) $\boldsymbol{d_f = 0\ sec}$

(b) $d_f = 10\ sec$

(c) $d_f = 30\ sec$

(d) $d_f = 60\ sec$

Figure 3.10 Results obtained on the S_{POM} sample with the sM2S2M-SEI experiment, with different values of the fixed delay. The insert allows to appreciate the decay due to the relaxation, without the interference of molecules crossing the slices due to convection.

The result of sM2S2M-SEI experiment with a fixed delay of $70\ sec$ carried out on the S_{POM} sample is shown in Figure 3.11. The first selected slice appears at about 16 kHz in the spectrum and relaxed for $490\ sec$. The last selected slice appears at -12 kHz and relaxed for $70\ sec$. No interference of convection is observed and the peaks present the resolution necessary to proceed with the plot of the areas (Figure 3.12), to fit with equation (79). A value of $252.28 \pm 43.60\ sec$ was obtained, which can be considered in good agreement with the value in Table 6, obtained from the same sample. The duration of the experiment was under 8 minutes, to be compared with the 2.5 hours of the conventional procedure.

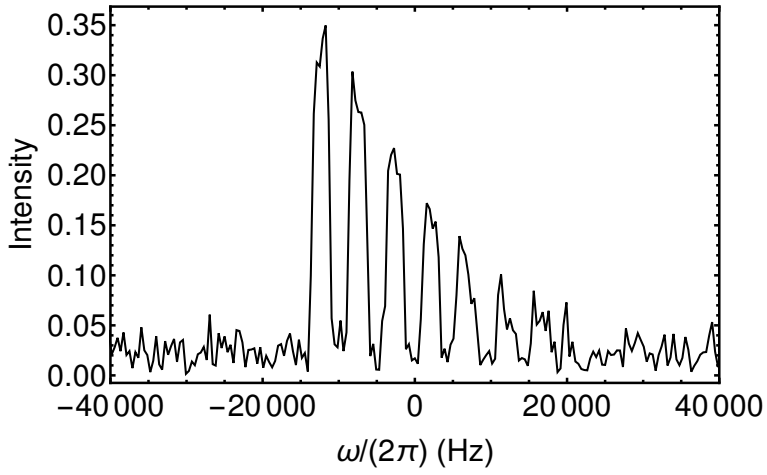

Figure 3.11. Results obtained on the S_{POM} sample with the sM2S2M-SEI experiment, with a fixed delay of 70 sec.

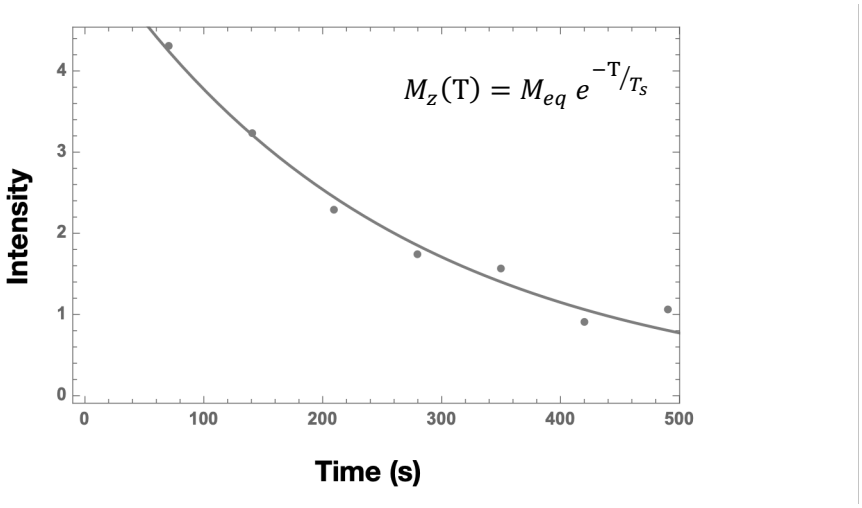

Figure 3.12. Plot of the areas of the peaks obtained from experiment in Figure 3.11. The curve was fitted with the function in presented in Chapter 2 (equation (79)).

University of Southampton

3.3 Conclusions

Single-scan measurement of singlet order relaxation decay constant was successfully realised by exploiting space-selective RF pulses with the aid of pulsed magnetic field gradients. The value obtained was reasonably close to the result of conventional relaxation decay measurement where a pseudo-2D experiment is conducted, requiring multiple acquisitions with an increasing variable delay. The procedure developed in this Chapter can potentially be applied to systems where singlet relaxation time of a few hours has been observed [31]. These include systems where the spin pair consists of two ^{13}C nuclei, whose low signal-to-noise ratio has been successfully enhanced through hyperpolarization techniques [32]. As the single-shot nature of experiments based on the use of hyperpolarized samples is not compatible with the reiterated excitations and acquisitions of conventional relaxation decay measurements, the procedure here proposed is a step towards a faster T_S measurement on samples requiring signal enhancement.

University of Southampton

4. Towards SADTI application to tissue engineering

Tissue engineering is at the hearth of regenerative medicine, which represents an excellent option for patients in need of tissue transplant [33]; growing cells in vitro on 2D surfaces such as dishes and culture flasks has become a standard procedure and has allowed biologists to develop extensive knowledge on cell behaviour and cell manipulation [7]; however, flat substrates generally used for 2D cultures present crucial differences from real extracellular microenvironments, which has a profound impact on cells development [34]; in particular, flat culture surfaces can only allow monolayered proliferation, and have an effect on cell morphology which has shown to be significantly different from what observed in vivo [34]; cell morphology can in turn influence many cellular processes, therefore the interest has grown for culturing techniques that replicate the conditions of natural tissue [7]. 3D tissue engineering is based on the use of three-dimensional scaffolds made of natural (collagen, chitosan, fibrin, elastin etc) or synthetic, biocompatible materials (such as poly-glycolic acid or hydrogels) on which healthy, expandable cells are seeded and maintained over a period of time in a favourable physiological environment which includes suitable conditions and nutrients supply. The higher level of complexity of

3D tissue cultures compared to the 2D ones, has the merit of providing a more realistic framework for cell proliferation and differentiation, but it also presents the challenge of a higher number of factors that can potentially affect the development of the culture. Structural properties of the scaffold (such as diffusivity, porosity, interconnectivity, pore size and pore size distribution) have a significative impact on the fate of the culture, as they not only determine the accessible space for the cells but also the efficiency of nutrients distribution and waste products disposal [33]; for this reasons, extensive interest and effort has been directed towards effective scaffold characterisation, as this allows a greater control on crucial variables that affect the culture. At the same time, the success of a tissue culture is based on optimal cell growth, which needs to be regularly assessed by the tissue engineer through a number of non-destructive tests; while a great part of the information on 2D cultures development can be provided by optical and fluorescence spectroscopy, 3D cultures present the challenge of a thicker volume to be inspected, which can consist for the most part of a material that does not allow light to penetrate. Confocal microscopy, particularly confocal laser scanning microscopy, is an imaging technique that has been widely used to monitor tissue growth and is capable of high-resolution optical sectioning in relatively thick samples, but its penetration depth is limited to roughly less than 100 μm [35]. Although there is no standard thickness for scaffolds

used in 3D tissue engineering (and this varies greatly depending on the intended use of the scaffold and the tissue), a study by Bryant at al. on the effect of scaffold thickness in tissue engineered cartilage, considered a range of scaffolds from 2 to 8 mm [36], while a study by Walles included bioartificial scaffolds in between 0.35 and 3.8 mm [37]. Confocal microscopy can provide insights on the upper layers of thick scaffolds, but it is not suitable to image the whole structure unless this is sectioned. Multiphoton Microscopy is a high-resolution fluorescence imaging technique that offers at least a twofold improvement in penetration depth compared to confocal microscopy [38] but it is based on the use of focused ultra-short laser pulses that could possibly damage the specimen through different mechanisms [35]. Micro-Computed Tomography (micro-CT) has been successfully used to characterise scaffolds intended for cell seeding [39]; micro-CT offers the advantage of rendering accurate 3D images of non-transparent structures, although it is not standard practice to use micro-CT for cell visualisation, as this requires chemical labelling of the cells and the resolution is nearly sufficient to render a good cell-to-scaffold X-ray contrast [40]; in 2018, a study by Shepherd et al. described the use of a desktop X-ray micro-CT to track barium sulphate labelled cells on collagen scaffolds [41]; although the study successfully reported contrast between the cells and the scaffold at the first stages of the culture, it was also noticed that less cells were observed after

a few days, which was ascribed to damage of the cells by the contrast agent or the agent concentration being reduced with each cell division. Optical-coherence tomography is a technique capable of obtaining high resolution images of thick tissue samples based on the light-scattering properties of the object; results on 1 mm thick cell-seeded scaffolds were reported where cell migration was tracked for the whole depth of the structure [35]; however, cell imaging was possible due to the natural contrast between the highly scattering tissue and the chitosin scaffolds used, which appeared transparent due to its low scattering properties. Other polymers frequently used for scaffold preparation, such as biocompatible polycaprolactone, present high light scattering properties [42] and would therefore not offer such contrast. Finally, MRI represents a valid alternative for 3D imaging of complex structures in a non-invasive way, and it is capable of reflecting changes in tissue hydration and macromolecular content, happening during the tissue growth [33]; however, paramagnetic contrast agents such as gadolinium-based formulations are generally used to enhance the positive signal of cells, and the requirement for gadolinium to interact with free water for altering the image contrast makes distinguishing the intracellular from the extracellular environment still a challenge [6]; label-free MRI on cells has been reported where contrast between cells and medium was obtained through the use of an optimised echo-time in high-resolution

proton density-weighted images [6]; in the same study, diffusion MRI was performed on PCL scaffolds and it was observed how the signal of water in cells and in the medium were affected differently by the increase of the diffusion gradient intensity [6]. Although presenting a sensitivity disadvantage compared to other techniques, these results motivate the interest for further investigation on how diffusion NMR and diffusion MRI can provide a contribution to the non-invasive, label-free monitoring of cells on scaffolds.

The interest of our group was sparked by our contacts with the Centre for Advanced Imaging in Brisbane (University of Queensland, Australia) who raised the issue of imaging the inner core of tissue culture on 3D polycaprolactone (PCL) scaffolds with pores of the order of hundreds of micrometres, for which long-lived singlet order appeared to be a promising resource. Indeed, it is not uncommon for cell density to decrease at the centre of the scaffold, compared to the boundary: this is usually the result of nutrients being absorbed by the cells in the external region, which creates resistance to the transportation of such nutrients to the core of the structure, thus causing detrimental conditions for the cells in the central part of the tissue [43]. The idea was to apply singlet-assisted diffusion tensor imaging approach to seeded scaffolds with cavities of 300 μm, which is currently not possible with routinely used DTI molecular probes. This idea was encouraged by the possibility

of determining changes in diffusion anisotropy as the tissue develops on the scaffold, due to the fact that the growing cells represent a time-dependent constraint to molecular mobility.

In-house electro-spun PCL scaffolds seeded with MC3T3-E1 (murine osteoblastic) cells were imported from Brisbane by Research Fellow Monique Tourell, together with the expertise and knowledge in conventional DTI. This collaboration and the encouraging results in applying singlet-assisted diffusion NMR to biological samples, consolidated the interest of the group in application to seeded scaffolds. Contacts with Brisbane when heavily affected by the pandemic in 2020, which made difficult to rely on the provision of custom made, cultured scaffolds, tailored to the NMR experiments being designed in this group. Different alternative collaborations were attempted: The Department of Materials Science and Engineering of University of Sheffield (UK) was initially involved to provide the scaffolds while the Centre for Human Development, Stem Cells and Regeneration (Institute of Developmental Sciences, IDS, University of Southampton, UK) was contacted to assist with the cell culture protocol. PCL scaffolds with fibre thickness and porous size comparable to the ones provided from Brisbane and previously used for singlet-assisted NMR experiments, turned out to be hard to produce and the structures supplied from Sheffield did not meet the criteria, particularly on the pore size and the fibre

thickness that could be achieved, which were excessively large for the intended purposes. In the absence of a source of custom-made structures, alternatives available on the market were considered and PCL scaffolds produced by 3D Biotek LLC based in New Jersey (US) resulted to be a suitable choice, although sample preparation had to be adapted to the size of these structures (i.e. multiple scaffolds had to be stacked in order to fill the coil region and provide sufficient NMR signal). Regarding the cell seeding, it proved to be difficult to find a collaboration that would take charge of the culture; however, great availability was granted by Prof. Nick Evans and his group from the IDS to provide training on general techniques for 2D cell culture and advice on scaffold seeding; although the entire process was slowed down by the multiple lockdowns, the knowledge acquired by hands-on experience at the IDS was transferred to our facilities in Chemistry, where Prof. Marcel Utz from Magnetic Resonance Group kindly allowed access to his microfluidics lab and the use of necessary equipment. This scenario meant that a very important component of the sample preparation was carried out with limited experience which undoubtedly impacted on the timescale of the project. By combining first-hand knowledge obtained during my training with a thorough literature review regarding cell culture techniques on 3D supports, it became clear how cell seeding protocols vary greatly depending on the purpose of the study and can be subject to adjustments

based on the scientist's expertise and insights; the wide range of scaffold materials and architectures available, together with the type of cells chosen to conduct the study, make very challenging to simply apply a general protocol to samples with unique structural and biological features. Finally, regardless of the scaffolds used, scientific literature does not seem to provide a standard protocol to ensure that the entire volume of the scaffold is uniformly seeded. A specific requirement for applying singlet-assisted diffusion tensor measurement (see Chapter 2) to 3D tissue engineering, is that the cell culture is uniform in three dimensions, meaning that the cells have evenly infiltrated the structure and there are no large areas left unpopulated while other get overcrowded. This is highly dependent on the efficiency of the seeding process, which is a crucial step to have a high number of cells attached to the support from the start of the culture [44,7]; to the best of our knowledge, an optimised procedure to ensure that cells are evenly seeded on the structure such that a gradual growth, uniform (in space and time) throughout the support is initiated, is not available and it is currently a challenge open to different suggestions for improvement. This is also confirmed by studies aiming to predict the success of scaffold seeding through mathematical simulations: in 2020, Liu Z. et al. published a study on the variables affecting cell attachment and distribution during the seeding process[44]; they reported of the experimental injection of a cell suspension on

scaffolds made of titanium alloy; the suspension was injected along the wall of the well where the scaffold was placed and cell density was assessed on a transverse plane of the structure through confocal microscopy; these results were then compared to simulations based on a mathematical model that considered various mechanisms of cell-material interaction; simulations agreed with the experiments in showing that most of the cells concentrated at the injection site as a gradual decrease of cell distribution from this region was observed [44]. This effect was considered a consequence of insufficient force of the liquid to transport cells from one side of the scaffold to the other. In this regard, diffusion bioreactors are designed to provide a continuous flow of fresh nutrients through 3D culture and to enhance mass transfer rate throughout the scaffold [45]. Perfusion can be used in the seeding process and has shown to improve cell distribution homogeneity [46]; Olivares and Lacroix [7] simulated cell seeding process on porous scaffolds under perfusion conditions using a multiphase model which accounted for the fluid dynamic of the culture media and the forces to which cells (treated as spherical particles) were subject; the model, which agreed on experimental results obtained in the same conditions [47], predicted that cell distribution was uniform through the scaffold except for the region closer to the injection site; in 2019, Magrofuoco et al. also reported inhomogeneous cell distribution through collagen scaffolds after seeding,

and indeed used the uneven distribution as initial condition for their model to predict successive stages of cell growth on the scaffold [34]; other authors have extensively investigated the experimental conditions that effect cell distribution in 3D cell cultures [48, 49].

Indeed, the lack of a reliable, non-invasive technique to monitor cell growth throughout the scaffold over time, mentioned at the beginning, appears to be intertwined with the lack of standard protocol to produce uniform cell cultures, as no imaging technique is currently able to provide information on the whole scaffold so to confirm the success of a specific seeding procedure in terms of even cell distribution.

The present chapter is presented with the only purpose of describing the challenges encountered and the ideas developed to overcome those, highlighting the areas of improvement and providing a contribution to a work that proved to be extremely complex and in need of interdisciplinary insights. Reported results are not to be considered conclusive and are showed as an example of a procedure whose development is currently in progress. Human bone-marrow stem cells were purchased and expanded on 2D supports before being seeded on PCL scaffolds; the 3D tissue culture fixed after 6 days was immersed in a solution of a singlet-bearing molecular probe, EPM (Figure 2.2) in deuterated ethanol, and the sample was

degassed to remove paramagnetic oxygen using an air-tight setup made in-house; a single diffusion tensor for the whole sample was determined using singlet-assisted DTI pulse sequence described in Chapter 2 to derive the spatial profile of diffusion in seeded scaffolds through the calculation of the average diffusion tensor; results were compared to what obtained for a sample of un-seeded scaffolds analysed in the same conditions.

4.1 Materials and Method

4.1.1. Molecular probe

A solution 0.5 M of EPM (Figure 2.2) in ethanol-d_6 was prepared to fulfil the criteria required to support long-lived singlet order preparation. The solution was degassed and successively combined with the 3D culture in the final sample assembly, as discussed in the following sections.

4.1.2. 3D structures

Polycaprolactone (PCL) scaffolds, PCL 3D Insert™, were purchased from 3D Biotek. Details of the structures are summarised in Figure 4.1.

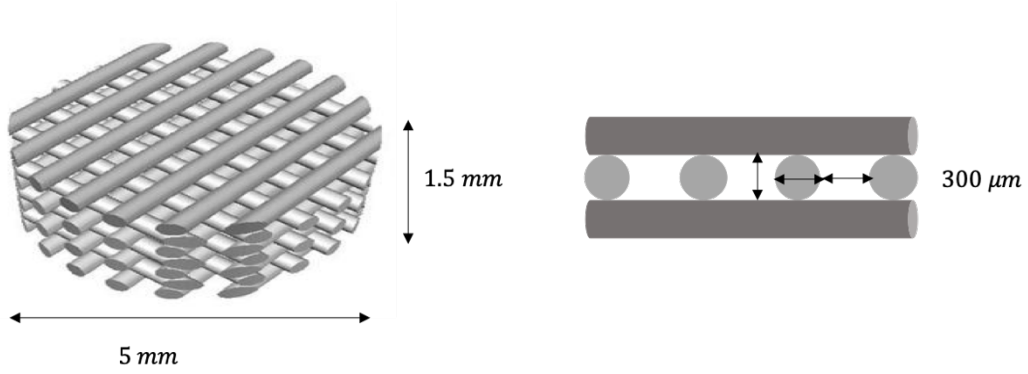

Figure 4.1 Polycaprolactone 3D Instert™ structure used in the present study (image provided by 3DBiotek LLC). Fibre's thickness 300 μm; pore diameter 300 μm.

PCL is a US Food and Drug Administration-approved material, and it was selected due to the great interest it has attracted in tissue engineering, and for consistency to the previous study on seeded scaffolds. Each structure was of cylindrical shape, 1.5 mm tall and with a diameter of 5 mm; the scaffolds were characterised by round fibres of 300 μm in diameter, spaced 300 μm. SEM images of a clean scaffold were taken and are reported in Figure 4.2 a. The size of each scaffold was such to fit a 96-well tissue culture plate.

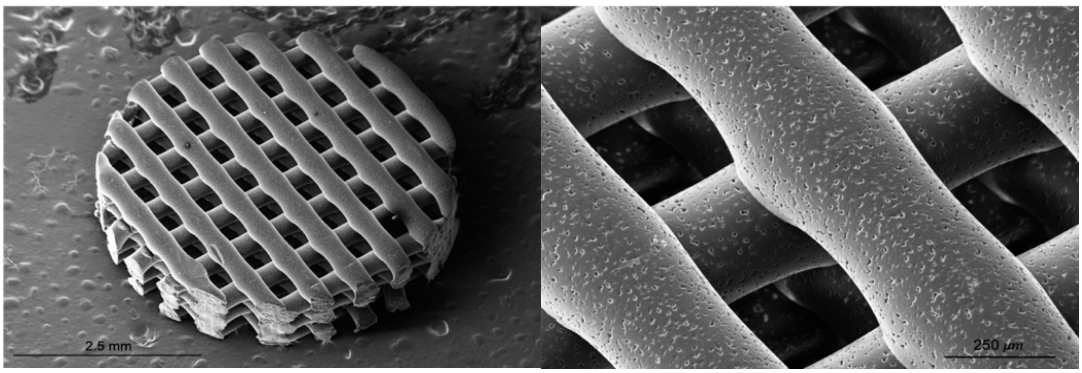

a.

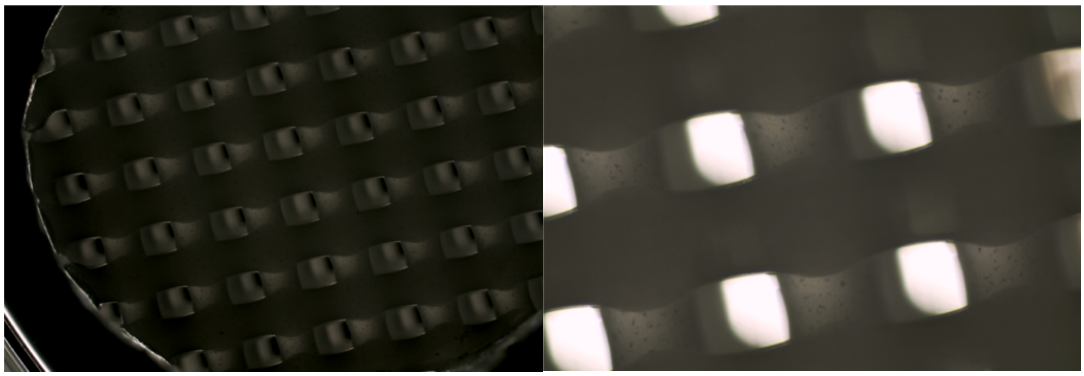

b.

Figure 4.2 a. SEM images acquired on a PCL scaffold after purchase using a Zeiss Leo1450VP instrument (tungsten filament); **b.** optical microscopy images of the same scaffold obtained with an inverted microscope Nikon Ti at 4x (left) and 10x (right) magnification.

University of Southampton

4.1.3.1. 2D cell culture

Cryopreserved Mesenchymal Stem cells obtained from human bone marrow were purchased from Sigma-Aldrich and immediately stored in liquid nitrogen ($-196\ °C$) until use. Basal expansion medium, frequently referred to as "basal media", was previously prepared using Minimum Essential Medium α (αMEM) supplemented with 10% of Fetal Bovine Serum and 1% of Penicillin-Streptomycin solution. All components were purchased from Sigma-Aldrich. The media was stored at 5 °C and pre-warmed in a 37 °C water bath before use.

Cells were then thawed: the closed vial, containing $\sim 10^6$ cells, was transferred in a 37 °C water bath and monitored until complete thawing. It was then disinfected with 70 % ethanol and transferred to a laminar flow hood where it was opened and the cell suspension was transferred to a sterile conical tube; 10 mL of pre-warmed basal media were added dropwise and the suspension was centrifuged (300 g-force) for 3 minutes. The supernatant solution was removed and the cell pellet was resuspended in 10 mL of basal media. 10 μL of this cell suspension was pipetted and stained with 10 μL of Trypan blue to determine the number of viable cells; 10 μL of the dyed suspension were transferred on a Neubauer counting chamber and viable (un-stained) cells were counted through optical microscope.

Cells were then seeded on T75 tissue culture flasks at a seeding density of ~6000 cells/cm^2 (1.5 mL of cell suspension per flask, ~5x10^5 cells per flask) to which 11 mL of basal media were added. Flasks were then transferred to a 37 °C humidified incubator, equilibrated with 5% CO_2. The next day basal media was refreshed, and the refreshed every 2 days until ~80% confluency was observed.

After 4 days, cells were passaged to new flasks. Using sterile filtered 1x Trypsin-EDTA solution (Sigma-Aldrich) cells were induced to detach from the culture surface in each flask: first, the media was removed, and the adhered cells were rinsed twice with 5 mL phosphate buffered saline (PBS) solution; 2 mL of trypsin were added and the cells were incubated for 5-6 min, checking at the microscope that they appeared to be floating in the media. 8 mL of basal media were added to stop the action of trypsin, and 1/10 of the volume was pipetted and centrifuged. The cell pellet obtained was then resuspended in 1 mL media and transferred to a new flask to which 12 mL of fresh basal media was added. Cells were passaged three times before being transferred to 3D culture.

4.1.3.2. 3D culture on scaffolds

After 10 days and 3 passages, cells were transferred to the PCL scaffolds for 3D culture following the protocol provided by the supplier. Trypsinised cells from all flasks were transferred to a 50 mL sterile tube and centrifuged for 4 min to 300g. The pellet was re-suspended in 1mL of media and cells were counted with Trypan blue on the Neubauer chamber. The suspension was then re-centrifuged and re-suspended in the suitable volume of basal media, necessary to obtain a cell suspension with a density of 200k cells in every 20µL. 120 µL of this suspension were used to seed 6 scaffolds, while the remaining was diluted to obtain the suspensions of 100k/20µL, 50k/20µL and 25k/20µL density respectively. A schematic representation of the dilution process is reported in Figure 4.3. The suspensions were used to seed 6 scaffolds for each density. In the laminar flow hood, each scaffold was placed in sterile 96-well plate and seeded by laying a drop of 20µL on the surface. Prior to seeding, each suspension was gently pipetted up and down to allow for the cells to uniformly distribute in the volume. The drop was carefully laid on the centre of each scaffold avoiding any suspension to wet anything but the scaffold itself. The seeded scaffolds were maintained in the incubator for 3 hours; they were then transferred to a new 96-well plate and immersed in 1 mL of basal media, making sure each scaffold remained at the bottom of the well, completely

submersed. The next day, basal media was replaced; after 2 days, basal media was replaced with osteogenic media to induce the differentiation to osteoblasts. Osteogenic media was prepared following a standard operative procedure available online (Nathalie Bock, Queensland University of Technology). Osteo-reagents β-Glycerophosphate, Ascorbate-2-phosphate and Dexamethasone were purchased from Sigma-Aldrich and stock solutions were prepared. A suitable volume of each stock solution was added to a batch of basal media to obtain osteogenic media with concentration 10 mM, 0.2 mM and 100 nM for the three reagents respectively. The 3D cell culture monitored and osteogenic media was replaced every 2 days until cell fixation. Cells were fixed after 6 days with Paraformaldehyde (PFA, 4% in PBS, Thermo Fisher Scientific): each scaffold was removed from the well and rinsed with PBS; it was then immersed in 500 μL of PFA and incubate for 10 minutes at room temperature. The scaffolds were then left dry in the hood overnight.

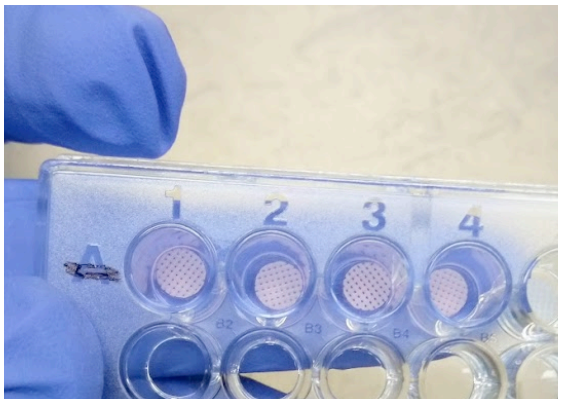

a.

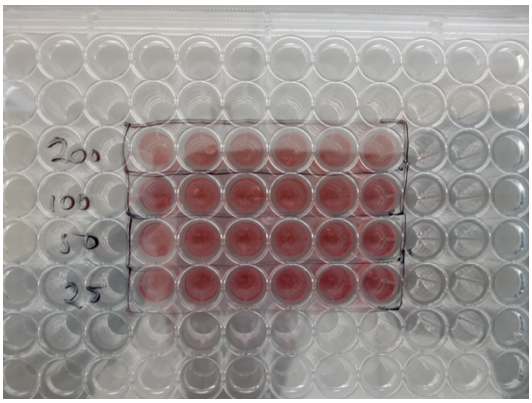

b.

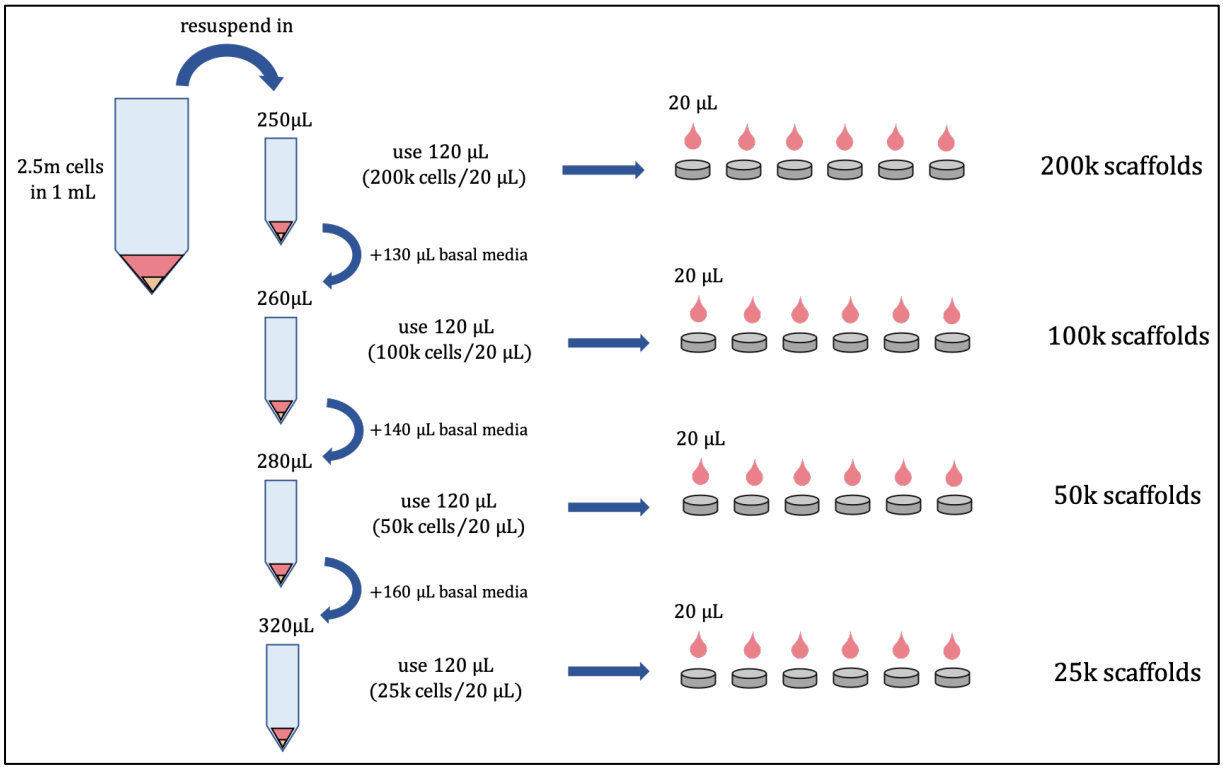

c.

Figure 4.3 a. scaffolds after 3h post-seeding with 20 μL of cell suspension; **b.** all the seeded scaffolds were then moved to a clean non-treated 96-well plate with fresh culture media; **c.** a schematic representation of the consecutive dilutions carried out from the main 2D culture to seed the scaffold with four different seeding densities.

4.1.4. Sample assembly and preparation

6 fixed scaffolds for each specific seeding density were stacked and transferred to an NMR tube to be combined with the EPM solution for diffusion NMR experiments. Two main steps were necessary for this sample assembly, due to the requirements of the specimen and the experiments to be carried out: first, a custom-made NMR tube was created of suitable size; secondly, the molecular probe solution was degassed separately in a different tube and successively poured on the scaffolds using an air-tight, custom-designed setup. The two steps of the process are described.

4.1.4.1. Sample holder

A cylindrical, glass tube of 10 mm O.D. was required due to the fixed size of the NMR probe; the I.D. of the tube was dictated by the scaffold diameter, while the wall thickness had to be such that the empty space left between the scaffolds and the wall was minimum, to avoid undesired free diffusion outside the region of interest. Moreover, the top end of the tube was required to fit a J-Young valve to allow for the air-tight transfer of the probe solution described in the degassing step. Finally, the neck of the tube should be large enough to allow the scaffolds to be inserted and possibly to be recovered without the need of breaking the tube. All

these constraints were solved by joining together two different tubes: a thick-wall, 10 mm LVP NMR tube was used due to its top end required in the solution degassing and transfer; the bottom end of this tube was replaced by the glass-blower, who instead fitted the top of a high-pressure valve as showed in Figure 4.4. The white cap of the HP valve was shortened and the space was used to arrange the 6 scaffolds, thus exploiting the glass wall thickness of that section of the tube. This arrangement allowed to have the scaffolds tightly packed together but also provided an easy access to the scaffolds for insertion and recovery. Moreover, both ends of the tube were compatible with the requirement of being air-tight.

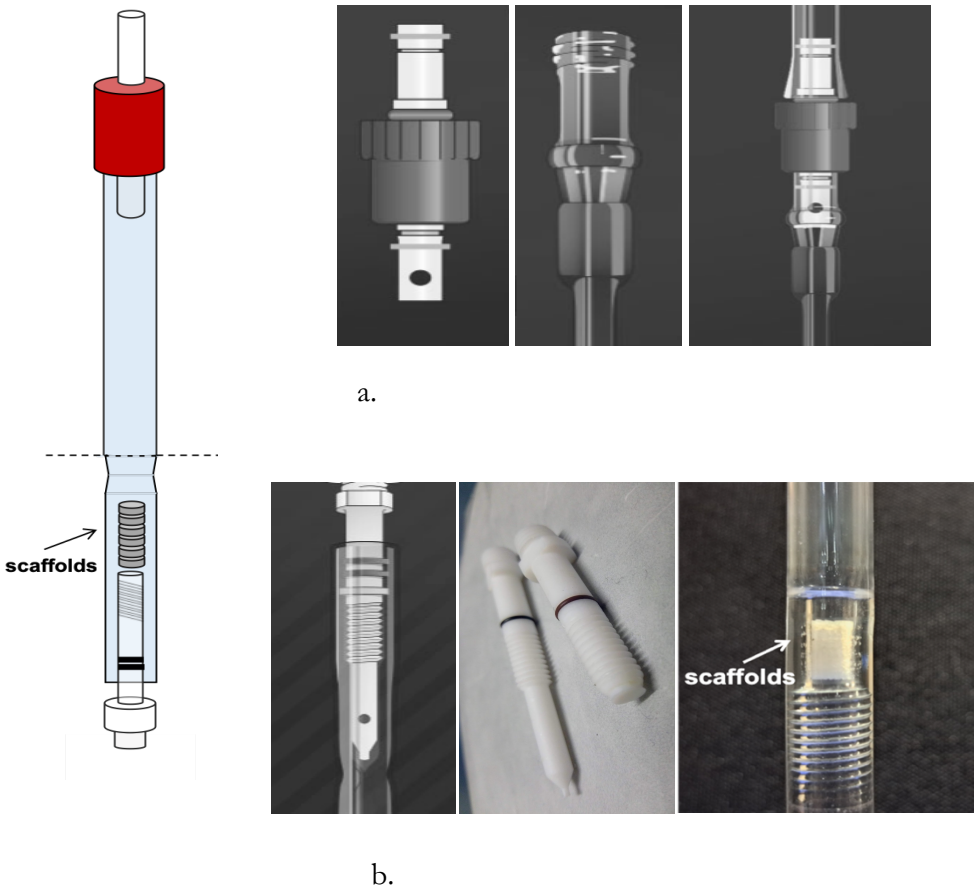

Figure 4.4 The sample holder was built from a modified LVP NMR tube to allow the easy insert and recover of the scaffolds. The top part of the tube was a J-young valve (a) while on the bottom part a high-pressure valve (b) was attached and modified to fit the scaffolds (images of valves courtesy of Norell Inc.)

University of Southampton

4.1.4.2. Solution degassing and transfer to sample holder

As anticipated earlier in this chapter, EPM solution in Ethanol was degassed to remove paramagnetic oxygen and ensure the longest relaxation decay possible was achieved for singlet order. Similarly to the samples prepared for the studies presented in Chapter 2 and Chapter 3, the degassing presented the challenge of having a solid object submersed in the solution offering little to no space for a capillary to be inserted and purge the system with inert gas. Differently from that case, however, freeze-and-thaw degassing could not be used as considered too harsh for the layers of fixed cells holding to the scaffolds, which could easily be damaged in the thawing process. In order to overcome this conundrum, a gas-tight manifold was designed and built to carry out gas purging of the solution in a separate tube, and successively transfer the oxygen-free solution to the sample holder exploiting the difference in pressure between the two parts of the system. Figure 4.5. shows the manifold in its real arrangements.

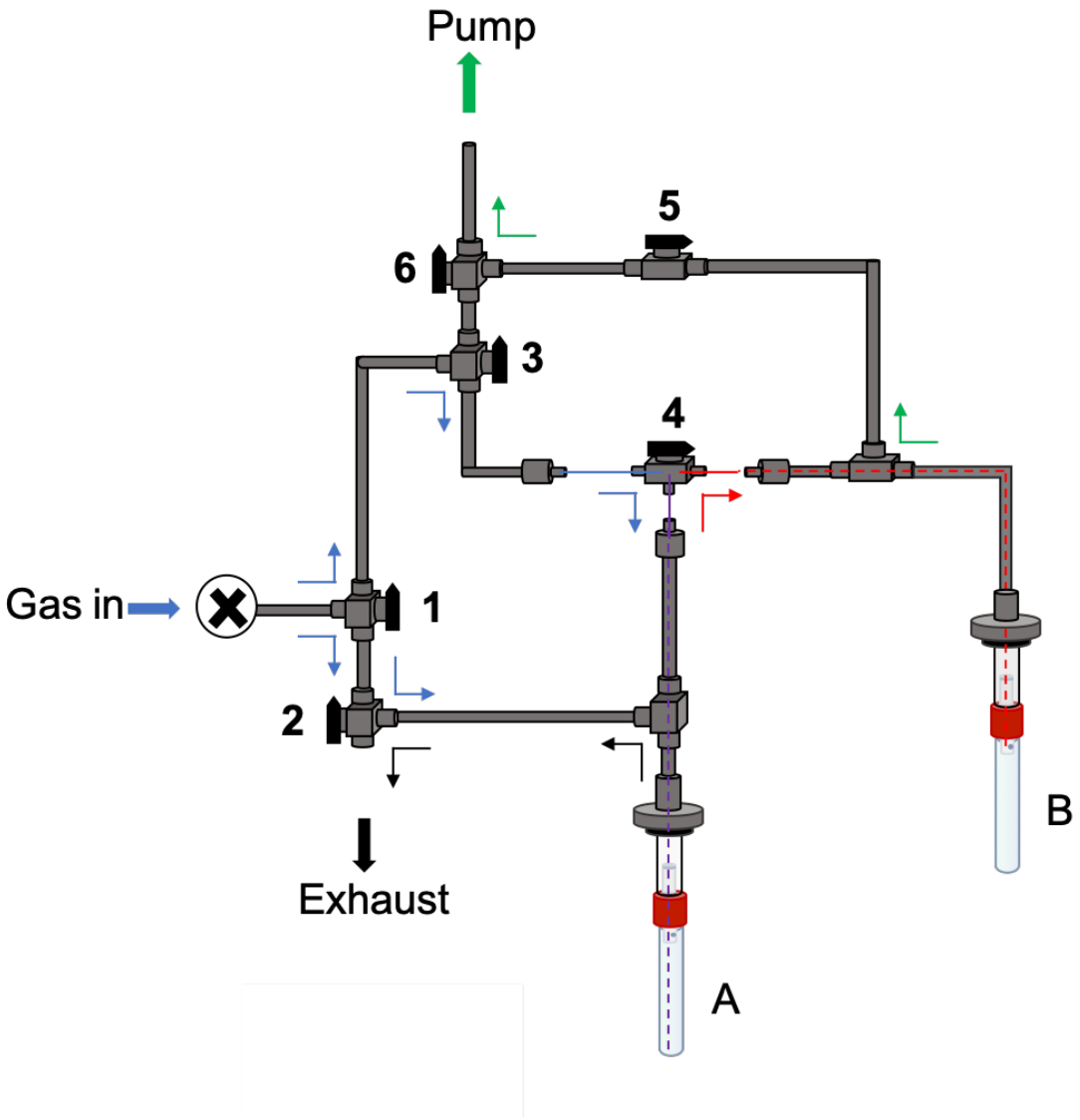

Figure 4.5 Arrangement of the setup used for solution degassing and transfer. The solution was placed in tube A while the scaffolds were in tube B. Blue arrows indicate the path of the inert gas during cleaning of the lines and during the degassing; green arrows indicate the direction of the vacuum; the inner line in purple allowed for the gas to purge the solution, while the inner line in red allowed for the solution transfer; black arrows indicate the outer line through which pressure was released during the gas purging (see text).

The tube containing 6 piled scaffolds was connected to the right side of the manifold through the J-Young valve, while the solution was place inside a 5 mm NMR tube fitted with the same type of valve. The degassing procedure was optimized and carried out as follows (Figure 4.5):

- First, the system was cleaned throughout to remove air: pure Argon was sent through valve 1, valve 3 and valve 4 to purge the lines on the bottom left area of the manifold. Gas was let flow through the inner line at 1 bar for a couple of minutes before tube A, containing the solution, was attached. Tube B and the top right area of the manifold were vacuumed through valves 5 and 6, connected to the pump. The two areas of the manifold were isolated from each other through valves 4 and 6, and were therefore cleaned separately.

- After gas purging, tube A is connected and the inner line is immersed in the solution; pressure is promptly reduced to produce a slow but steady bubbling through the solution. Pressure in the tube is released through the outer line and the exhaust (valve 2). The solution is degassed for 5 min and pressure is monitored and adjusted to maintain a steady flow. During the degassing of tube A, tube B is kept under vacuum.

- After 5 min of gas purging, the solution is sent to tube B exploiting the difference in pressure between A and B. First, the exhaust valve is closed. Then gas flow is stopped by closing the main gas valve 0. Valve 5 is also closed to stop the vacuum in tube B. Finally, valve 4 is moved to connect tube A and tube B, letting the solution flow through the inner line due to the pressure difference. The solution is sucked through the line until pressure is equilibrated. If some liquid is left in tube A, gas can be sent through valve 2 and the outer line, to increase the pressure and push the residue through the inner line. This also allows to leave tube B with a positive pressure above the liquid, thus further reducing the risk of air leak inside the tube over time.

Figure 4.6 a. shows the sample holder filled with the degassed solution. A volume of solution of around 200 μL was transferred to the tube as a free volume of 100 μL was calculated for an empty, non-seeded scaffolds considering its geometrical features; no bubbles were observed after the transfer, however the tube was gently shaken until the volume above the solution displayed a thin meniscus. The drawing in Figure 4.6 b. clarifies the arrangement of the scaffolds within the tube, showing that each scaffold fibres were not aligned to the fibres of the next one.

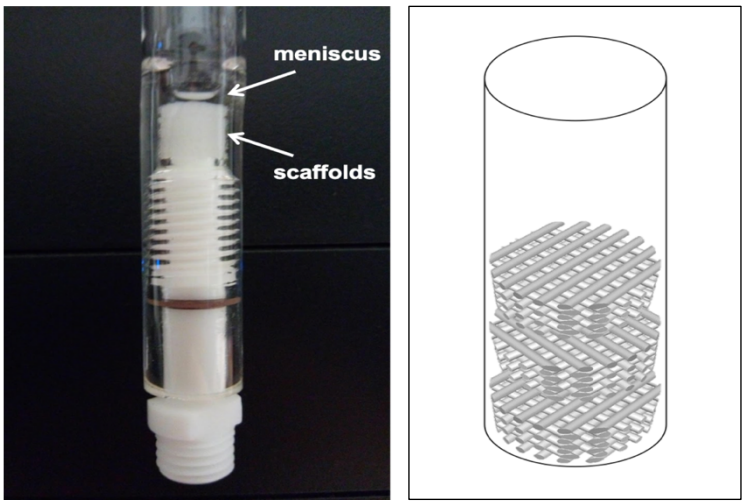

a. b.

Figure 4.6 a. Bottom part of the sample holder showing the six scaffolds immersed in the solution; **b.** the scaffolds were arranged in a stack with their fibres not aligned.

4.1.5. Experiments

Singlet order relaxation decay constant T_S and longitudinal magnetization decay constant T_1 were measured in the final samples. Pulse sequences represented in Figure 1.12 and Figure 1.14 were used respectively. Singlet-assisted diffusion tensor measurement was carried out using singlet-assisted diffusion NMR pulse sequence described in Chapter 2 (Figure 2.4).

For each sample, the derivation of the diffusion tensor was first carried out with a diffusion time Δ of 1 second, and six different gradient directions with an intensity spanning from 1 to 90% of the maximum gradient in 8 steps. Then, the experiment

was repeated on the same sample with a Δ of 90 seconds and gradient intensities gradually going from 1 to 10% of the maximum in 8 steps were used. The first experiment was used to calibrate the gradients as described in 2.2.2.3. The second experiment was used to calculate the diffusion tensor for the entire sample in restricted conditions, once that the gradient intensities had been adjusted according to the calibration.

4.2. Results and discussion

4.2.1. Cell culture

HBM cells responded well to the thawing process and were assessed as viable before each passage and prior to transfer on the scaffolds. Cells were monitored throughout the 2D culture using an optical microscope which confirmed their attachment to the culture surface and their characteristic elongated shape (Figure 4.7 a.). 3D culture was also monitored through optical microscope and cells could be observed populating the structures from the second day of culture (Figure 4.7 b.) Indeed, proliferation was fast and the culture was stopped after 6 days as most of the

scaffolds seeded with the highest density (200k cells/scaffold) looked completely infiltrated.

The 6 scaffolds seeded with the lowest seeding density (25k cells/scaffold) showed comparable levels of infiltration and each scaffold looked reasonably uniform from the top layer accessible through optical microscopy. Figure 4.8 shows one of the scaffolds of this series as representative of the 6. All 6 scaffolds seeded with 100k cells (Figure 4.9) showed little to no coverage. This had already been observed in other 3D cultures previously carried out and it was ascribed to a little number of cells in the volume pipetted at the moment of seeding; despite the care taken to pipette up and down the desired volume before placing the drop on the scaffold, the same issue was observed. A possible explanation is that most of the cells had quickly gone through the scaffold for gravity and were left on the surface of the well when the scaffold was moved to a new plate after the first 3 hours of incubation. Moreover, surface tension of the cell suspension made very difficult to control the dynamic of the drop once placed on the scaffold, although care was taken to prevent the liquid to wet the well before wetting the scaffold. The same problem was observed in the 200k and 50k cultures; interestingly, some of the 50k scaffolds were quickly covered to the point of appearing as populated as the 200k, while other were more similar to the 25k scaffolds. For these reasons, all the 25k scaffolds were used

to prepare a sample to run SADTI experiments on, while the 100k were excluded. Three of the most populated 50k scaffolds were combined with three of the 200k scaffolds due to the similarities observed (Figure 4.10 a. and b.).

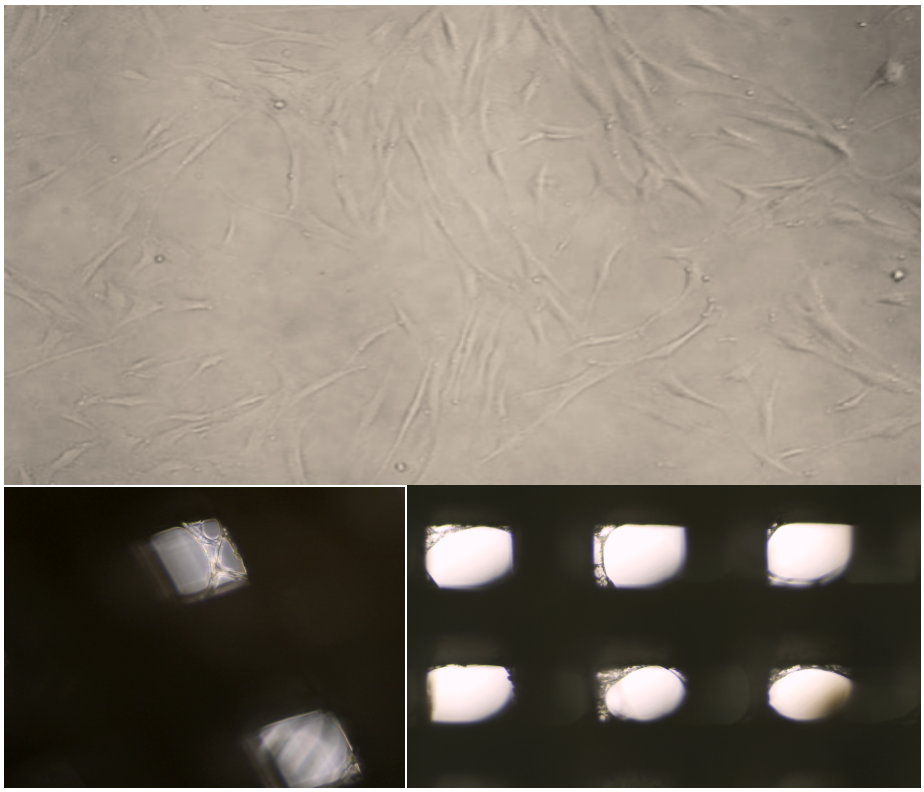

a.

b.

Figure 4.7 a. Optical microscopy image 10x magnification of the 2D culture; **b.** details of the cells populating the 3D scaffold at the second day of 3D culture

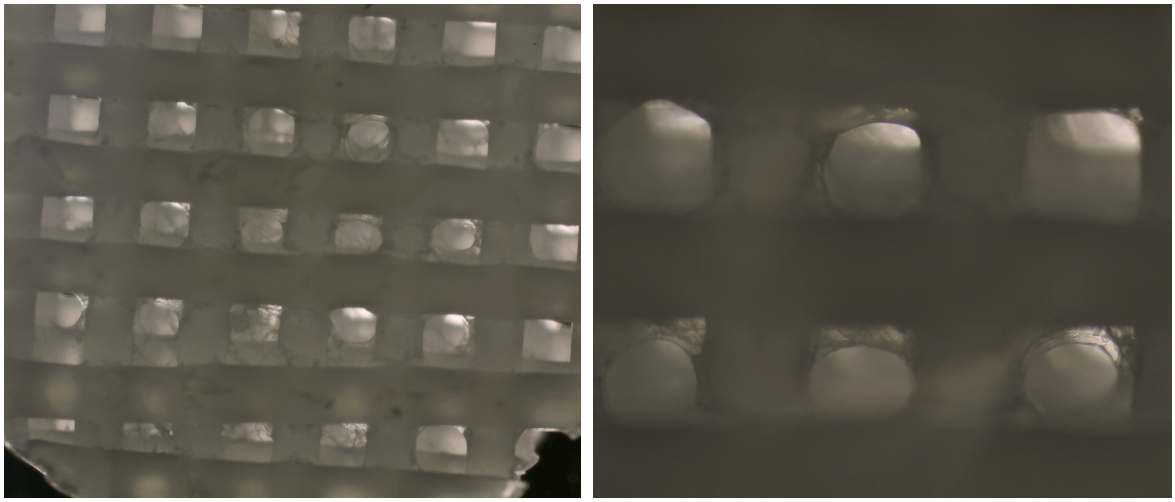

Figure 4.8 Optical microscopy images of a representative sample of the series of scaffolds seeded with 25k cell/scaffold density. The rounder edges of the pores are the result of cell growth and infiltration.

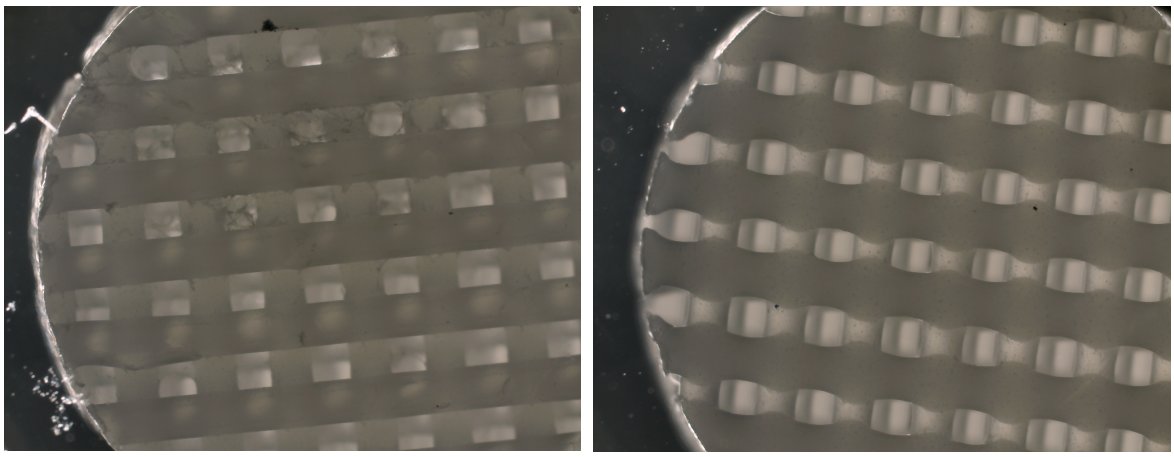

Figure 4.9 Optical microscopy images of a representative sample of the series of scaffolds seeded with 100k cell/scaffold density. The images were taken at the end of the six-days 3D culture and show little to no coverage, indicating an unsuccessful seeding.

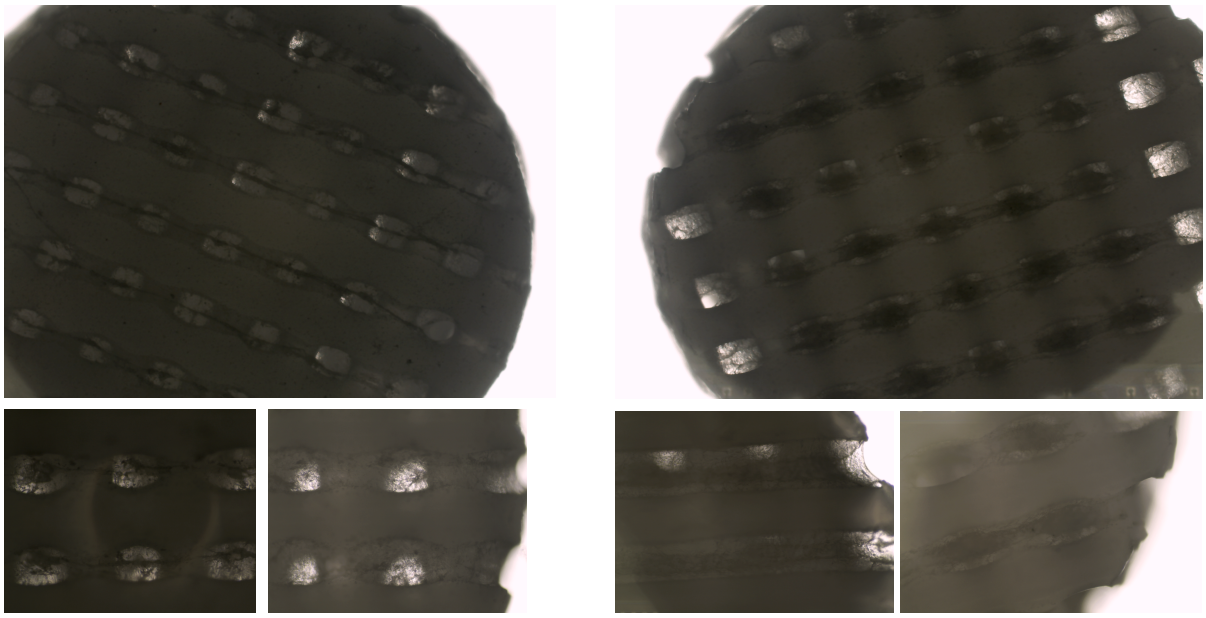

a. b.

Figure 4.10 a. Optical microscopy images on the populated scaffolds seeded with 50k cell density (a) and 200k seeding density (b); for some scaffolds of each series, the level of cell infiltration results comparable, showing the cavities closed so that light cannot pass through.

University of Southampton

4.2.2. Sample degassing

EPM solution in ethanol-d_6 was degassed through a different procedure compared to all the samples prepared in the studies previously described (see Chapter 2 and 3). The use of the setup described in 4.1.4.2 was validated prior to sample degassing. In Table 7, the results for T_1 and T_s obtained for a solution of EPM in ethanol-d_6 prepared for the setup validation are reported. The values obtained on a non-degassed solution are compared with those achieved with gas purging with and without the use of the airtight manifold.

Table 7 Relaxation decay constants of longitudinal and singlet order obtained during the validation of the degassing setup and compared with a non-degassed sample and a sample where gas purging was carried out using a simple capillary immersed in the solution.

	$T_1(sec)$	$T_s(sec)$
Not degassed	3.5 ± 0.2	7 ± 1
Degassed (setup)	9 ± 1	179 ± 3
Degassed (capillary)	9 ± 1	251 ± 12

Singlet order relaxation decay extension clearly results from dissolved oxygen removal, as shown from the values in Table 7. Through the use of the setup, it was possible to increase T_S of an order of magnitude, although gas purging through a capillary appears to be more effective. This is most likely due to imperfections in the manifold connections. As T_S lifetime can be affected by dissolved oxygen even when this is present in very small concentration (ppb, for details see [24]) a strict control of air leaks is necessary in order to ensure a complete oxygen removal. Adjustments to the first version of the setup used for these experiments are currently being implemented to improve the performance of the system.

Figure 4.11 shows the result of T_S measurement on the sample prepared with un-seeded scaffolds (control sample), while Figure 4.12 and Figure 4.13 report on the values obtained on the samples seeded with 25k and 200-50k cells per scaffold respectively. A much shorter value resulted from the degassing of the sample containing the most populated scaffolds. As the conditions of the degassing were the same for the three samples, such difference could depend on the lower quality of the data, also reflected in the higher error. Signal-to-noise issues might have arisen due to the complexity of the structure causing an inefficient perfusion of the solution

and thus creating empty areas in the sample region that compromised the quality of the data.

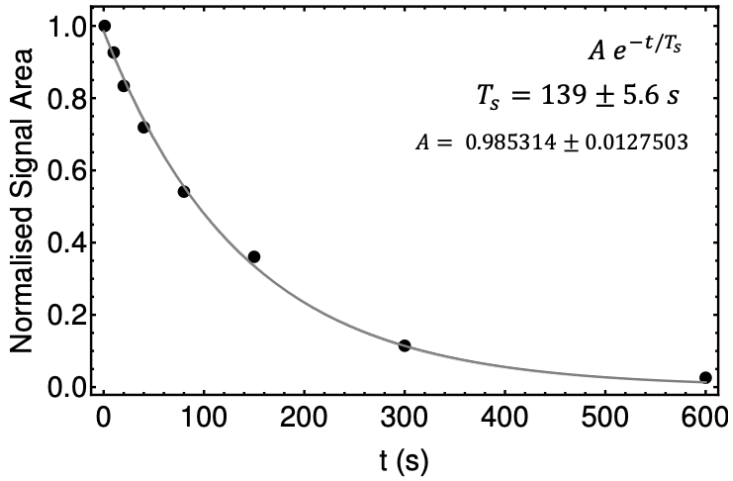

Figure 4.11 Relaxation decay of singlet order created in the sample with clean scaffolds (control)

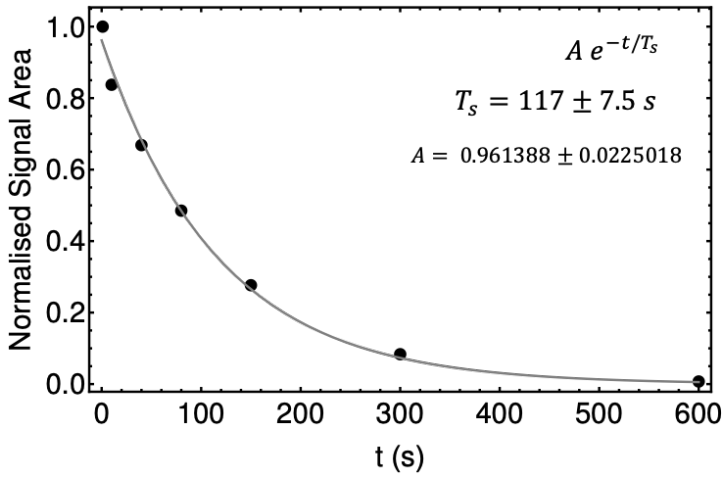

Figure 4.12 Relaxation decay of singlet order prepared in the sample with scaffolds seeded at 25k cell/scaffold seeding density.

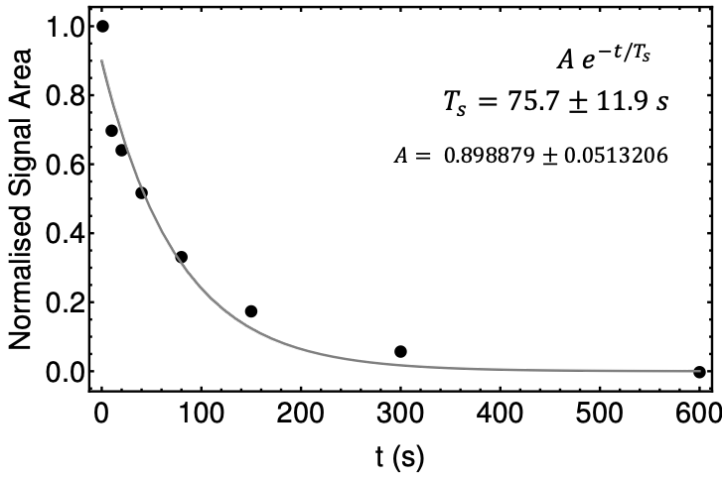

Figure 4.13 Relaxation decay of singlet order prepared in the sample with 3 scaffolds seeded at 50k cell/scaffold density and 3 scaffolds seeded at 200k cell/scaffold density.

4.2.3. Diffusion tensor measurement on scaffolds

Table 8 summarises the results obtained by applying SADTI procedure on the three samples. For each sample, the diffusion profile obtained with $\Delta = 90\ sec$ is represented through the ellipsoid (showed in three different orientations to appreciate its 3D features) resulting from the diagonalization of the diffusion tensor as described in 1.4.3.2.

University of Southampton

Table 8 Results of the application of SADTI pulse sequence to 3D tissue culture. For each sample, the ellipsoid deriving from the diffusion tensor is displayed in three different orientations. FA is the dimensionless fractional anisotropy calculated as showed in equation (65) and ADC is the apparent diffusion coefficient.

Seeding density	Ellipsoid	FA	ADC (m^2/s)
Control	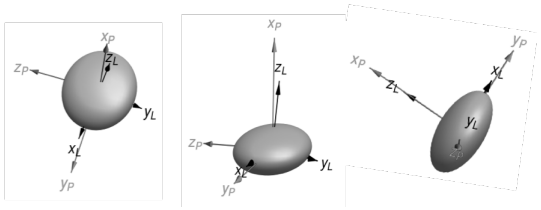	0.4 ± 0.1	$5.3 \times 10^{-10} \pm 2.8 \times 10^{-11}$
25k	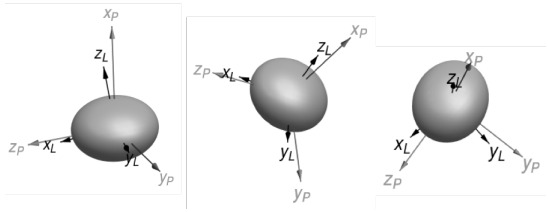	0.2 ± 0.1	$7.3 \times 10^{-10} \pm 4.5 \times 10^{-11}$
200-50k	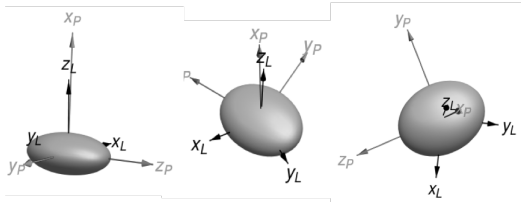	0.3 ± 0.1	$4.8 \times 10^{-10} \pm 2.7 \times 10^{-11}$

Fractional anisotropy (FA) values extracted from the tensor calculation are also reported together with the resulting apparent diffusion coefficient (ADC). For each sample, ADC was obtained by calculating the scalar value of D along each of the six gradient directions used in one SADTI experiment, and considering the average. Due to the preliminary nature of the entire experimental procedure, the reported results cannot be considered representative of the analysed structures although some considerations can be done: the control sample, made of 6 stacked unseeded scaffolds displays a diffusion profile with anisotropic features, reflected on the flattened shape of the ellipsoid; this is consistent with the fact that the scaffolds within the tube where arranged with random orientation on the x-y plane, so that the fibres of two consequent scaffolds were not aligned (Figure 4.6 b). This arrangement prevented the creation of open channels along the z-axis (LAB-frame) and therefore of a free path for the molecules along that direction; as a diffusion time of $90\ sec$ corresponds to a probed distance of about $350\ \mu m$, the conditions were such that molecules diffusing along the z-axis would experience a greater level of restriction compared to those diffusing on the x-y plane, where each scaffold presents open channels that run along the entire cross section. Indeed, the FA and the ADC values report on a degree of diffusion anisotropy, ADC being smaller than the $7 \times 10^{-10}\ m^2 s^{-1}$ previously obtained in ethanol-d_6. The diffusion pattern

displayed for the seeded samples is of more difficult interpretation: the sample with 25k seeded scaffolds shows a smaller degree of anisotropy along the z-axis compared to the control; this is consistent with the presence of cells infiltrating the structure and making the diffusion on the x-y plane gradually as restricted as what experienced by molecules moving perpendicularly to the pile of scaffolds. However, this interpretation is contradicted by the ADC value that results more similar to what obtained in unrestricted conditions, therefore further investigation is required.

University of Southampton

4.3 Conclusions

The first stage of a study aiming at characterising cell infiltration of PCL scaffolds through singlet-assisted diffusion tensor calculation was presented with preliminary results. The stages of sample preparation were described in greater detail as they represented a challenging part of the procedure validation. In particular, an even cell population throughout the scaffolds is required in order to consider the diffusion tensor representative of the constraints encountered by molecules moving through the porous structure; however, ensuring uniform cell distribution during the seeding process proved to be challenging; this problem is known in literature and has shown to have great impact on the development of the tissue during the culture [7, 44]. To perform NMR experiments, the seeded scaffolds were placed in a solution of a molecular probe that allows preparation of singlet order through the suitable pulse sequence; the use of singlet order to store information during the diffusion time Δ, allowed to track diffusion for 90 seconds, which can create the conditions for observing restriction in scaffolds with pores of 300 μm of diameter. Degassing of the solution was necessary to remove paramagnetic oxygen and achieve a long singlet relaxation decay T_S and for this purpose an equipment was designed and built to purge the solution with inert gas and transfer it to the tube containing the seeded scaffolds without damaging the specimen and in airtight conditions. The setup

allowed to achieve a decay constant one order of magnitude higher that what possible before the oxygen removal. A diffusion tensor and the ellipsoid displaying the 3D profile of diffusion was obtained for a sample made of non-populated scaffolds and two samples with lightly and heavily populated scaffolds respectively. Although results cannot be considered representative, the steps that led to their acquisition provided numerous insights for the development of a more effective procedure. Different areas of improvements were identified during this study; although initially beyond the expertise of this group, the seeding procedure was studied and different adjustments were investigated, which are currently being implemented for successive trials; among these are: the use of different techniques to lay the cell suspension's drop onto the scaffold surface during the seeding process; the treatment of PCL scaffold surface with calcium phosphate coating to improve cell adhesion [50]; the use of macromolecules to alter cell suspension density and viscosity and prevent cells from reaching the bottom of the well before adhering to the scaffold [51]. The PCL structure chosen also represents a variable which would greatly affect the procedure and the interpretation of the results: a long, cylindrical structure, a few millimetres tall would offer more signal and would be more practical in the sample preparation compared to scaffold stacking; however, the seeding protocol would have to be adapted to the thickness of the structure: in this regard,

a perfusion bioreactor has recently been purchased by the group and its use is being investigated to improve cell infiltration on thick scaffolds of a few cm of thickness (a single, long scaffold with open channels along the z-axis would determine a different free-path pattern observed in non-populated structures, compared to the piled up thinner scaffolds used in the present study, and the results of cell-infiltrated structures would have to be interpreted accordingly). Once that sample preparation is optimised, the diffusion profile obtained through diffusion tensor calculation can be considered reliable and indicative of the inner structure of samples with obvious limitations for live cells, due to the need of removing oxygen from the sample to achieve a longer T_S. In order to make this procedure applicable to live samples, the development of a new, non-toxic, singlet-bearing molecular probe should be addressed. Moreover, the molecule should be soluble in water due to the aqueous nature of the culture media, and its T_S should be less sensitive to paramagnetic oxygen. Singlet order prepared in nearly-equivalent ^{13}C spin pair ensemble is typically less sensitive to oxygen [24] but such systems provide less sensitivity which in turn requires a higher number of scans, thus increasing the duration of the experiment. Finally, the NMR measurements experiment should not cause stress to the cells, i.e. the instrumentation should be equipped to ensure that temperature and CO_2 pressure are compatible with the optimal conditions for the cells, especially for

experiments lasting a few hours. Application of the technique to live cells is currently not possible without an extended investigation on these issues.

Overall, the entire process (from cell seeding to NMR measurement) is affected by a very high number of variables and keeping only a few of them under control proved to be extremely challenging. The use of a less oxygen-sensitive molecule would also be beneficial for fixed cell samples: it would allow to skip the degassing, thus resulting in a faster and less harsh sample preparation, leaving the fixed culture in similar conditions to an un-fixed one. In fact, the use of the procedure described in this work could still be insightful when applied on fixed cells: if the culture protocol has been optimised, and once that the reproducibility of the seeding technique has been proved, it would be possible to use one fixed sample as representative for a number of live samples with the same seeding density. Since the technique is non-destructive (and if the number of steps from fixation to NMR experiment is minimised) one sample for each seeding density could be fixed and its structural properties should be considered reliable to assess the live samples cultivated in the same conditions.

University of Southampton

5. Conclusions

The use of magnetic field gradients in NMR experiments was reviewed and new possibilities offered by the combination of such gradients with long-lived singlet order preparation were investigated. Spatial selectivity provided by shaped radio-frequency pulses applied in parallel with position-encoding gradients was exploited to develop a new, faster procedure for singlet order decay constant measurement; the results, published in [27] showed that it is possible to obtain a relaxation profile by exciting different sections of the spin ensemble at the same time, and letting them decay in sequence; this strategy bypasses the need of a list of separate acquisitions where the whole sample is repeatedly excited and let relax, thus allowing to reduce the process to a single-scan measurement. These results represent an important accomplishment in the contest of exceptionally long relaxation decay constants, such as that of singlet order prepared in a system of ^{13}C spin pairs, where a T_S of a few hours has been observed [31]. Indeed, the low signal-to-noise ratio in these systems benefits from the use of hyperpolarised techniques (such as PHIP [52], SABRE [53] and dissolution-DNP [54]). As the single-shot nature of the experiments carried out on hyperpolarised samples is not compatible with a list of subsequent excitations

and acquisitions, single-scan T_S measurement represents a valuable step towards the derivation of hyperpolarised singlet-order relaxation decay constants.

Diffusion-sensitising pulsed field gradients were also studied and their use in multiple directions of space was combined with singlet order preparation. Previously in this group singlet order's long relaxation decay was exploited to run singlet-assisted diffusion-NMR (SAD-NMR) experiments with larger values of the diffusion time Δ; this led to the idea of creating anisotropic conditions within systems where common molecular probes like water would not experience any constraint, and to use such restrictions to infer three-dimensional properties of the system expressed by a diffusion rank-2 tensor. In the present work, this idea was realised by combining diffusion tensor imaging (DTI) data acquisition and processing with the pulse sequence used in SAD-NMR. The resulting SADTI experiment was developed and the diffusion tensor in restricted conditions was derived for systems with aligned channels of 1 mm cross section. The promising results encouraged the application of SADTI to 3D tissue culture characterisation; this represented a new challenge for the group, as the disruption caused by COVID-19 led us to take entirely charge of the sample preparation, and therefore of the tissue cultivation, with no background in biology or tissue engineering. The literature review that resulted from this stage of the work allowed to verify how the field of 3D tissue culture is currently in need

of a standard protocol to ensure uniform cell infiltration of the structure, and provided a stronger motivation for applying SAD-NMR and singlet-assisted diffusion tensor calculation to such samples, for which preliminary results are presented.

The development of a final protocol was mainly limited by obstacles encountered in the sample preparation, specifically in the scaffolds seeding to achieve an even distribution of cells; this is currently under further investigation in the group. Indeed, the study described in this work presents numerous areas of improvements, many of which have been highlighted in section 4.3. Although the goal of the SADTI procedure is to replace destructive techniques required to characterise the internal architecture of samples such as 3D tissue cultures, such techniques would be beneficial to support the development of SADTI. For example, histology and fluorescence microscopy on sectioned scaffolds could support the optimisation of the cell seeding protocol; the acquisition of MRI images on the sample would allow to verify the presence of air bubbles which would interfere with the derivation and interpretation of the diffusion tensor; contrast agents could be used to support this stage and confirm the perfusion of the solution throughout the porous system. The model used to describe the diffusion profile could also be revised; further studies on the structural properties of a 3D tissue culture (including mathematical simulations

to predict the distribution of cells on the support) could be used to assess if the porous structure arising from cell infiltration can actually be considered of low complexity. Hall and Barrick [55] proposed the derivation of the diffusion tensor based on the measurement of the anomalous diffusion coefficient in complex environments, which could potentially be applied to SADTI procedure without dramatic experimental differences; other parameters to describe the structural properties of the system such as porosity, tortuosity and obstruction [56] could also be investigated through singlet-assisted diffusion measurement, to determine a more accurate picture of the conditions a molecular probe experiences when diffusing through fixed cells, and the role that the extracellular matrix plays in creating a system of interconnected cavities. The use of a less oxygen-sensitive singlet-bearing molecule, previously mentioned in Chapter 4, could drastically simplify sample preparation, which would then be more representative of live cells 3D culture treated in the same conditions.

In conclusion, the combination of different fundamental concepts of NMR was studied and applied to develop new experimental strategies; the interest of the research was then extended to the field of tissue engineering, thus resulting in a wider, interdisciplinary investigation on how singlet-assisted diffusion NMR and MRI can support the bio-medical field in the effort for improving 3D tissue culture

procedures. The present study highlighted numerous challenges involved in the non-invasive characterisation of 3D porous structures, and proposed an approach based on the non-destructive diffusion tensor calculation, which is currently being further developed by the group.

University of Southampton

6. Bibliography

(1) Tayler, M. C. D.; Levitt, M. H. Singlet nuclear magnetic resonance of nearly-equivalent spins. *Physical Chemistry Chemical Physics* **2011**, *13* (13), 5556-5560.

(2) Carravetta, M.; Johannessen, O. G.; Levitt, M. H. Beyond the T1 limit: Singlet Nuclear Spin States in Low Magnetic Field. *Phys. Rev. Letters* **2004**, *92* (15), 153003.

(3) Carravetta, M.; Levitt, M. H. Long-lived nuclear spin states in high-field solution NMR. *J. Am. Chem. Soc.* **2004**, *126*, 6228-6229.

(4) Pileio, G.; Carravetta, M.; Levitt, M. H. Storage of nuclear magnetization as long-lived singlet order in low magnetic field. *Proc Natl Acad Sci U S A* **2010**, *107* (40), 17135-17139.

(5) Pileio, G.; Ostrowska, S. Accessing the long-time limit in diffusion NMR: The case of singlet assisted diffusive diffraction q-space. *J Magn Reson* **2017**, *285*, 1-7.

(6) Abarrategi, A.; Fernandez-Valle, M. E.; Desmet, T.; Castejón, D.; Civantos, A.; Moreno-Vicente, C.; Ramos, V.; Sanz-Casado, J. V.; Martínez-Vázquez, F. J.; Dubruel, P.; et al. Label-free magnetic resonance imaging to locate live cells in three-dimensional porous scaffolds. *Journal of The Royal Society Interface* **2012**, *9* (74), 2321-2331.

(7) Olivares, A. L.; Lacroix, D. Simulation of cell seeding within a three-dimensional porous scaffold: a fluid-particle analysis. *Tissue Eng Part C Methods* **2012**, *18* (8), 624-631.

(8) Levitt, M. H. *Spin Dynamics. Basics of Nuclear Magnetic Resonance*; Wiley, 2007.

(9) Mori, S.; Tournier, J. D. *Introduction to diffusion tensor imaging: And higher order models: Second edition*; Elsevier Inc. \, 2013.

(10) Minati, L.; Węglarz, W. P. Physical foundations, models, and methods of diffusion magnetic resonance imaging of the brain: A review. *Concepts in Magnetic Resonance Part A* **2007**, *30A* (5), 278-307.

(11) Basser, P. J.; Mattiello, J.; Lebihan, D. Estimation of the Effective Self-Diffusion Tensor from the NMR Spin Echo. **1994**, *103* (3), 247-254.

(12) Badii, R.; Politi, A. *Complexity: Hierarchical Structures and Scaling in Physics*; Cambridge University Press, 1997.

(13) Metzler, R.; Rajyaguru, A.; Berkowitz, B. Modelling anomalous diffusion in semi-infinite disordered systems and porous media. *New Journal of Physics* **2022**, *24* (12), 123004.

(14) Palombo, M.; Gabrielli, A.; Servedio, V. D.; Ruocco, G.; Capuani, S. Structural disorder and anomalous diffusion in random packing of spheres. *Sci Rep* **2013**, *3*, 2631.

(15) Pierpaoli, C.; Jezzard, P.; Basser, P. J.; Barnett, A.; Di Chiro, G. Diffusion tensor MR imaging of the human brain. *Radiology* **1996**, *201* (3), 637-648.

(16) Alexander, D. C. An Introduction to Computational Diffusion MRI: the Diffusion Tensor and Beyond. In *Visualization and Processing of Tensor Fields*, Weickert, J., Hagen, H. Eds.; Springer Berlin Heidelberg, 2006; pp 83-106.

(17) Pileio, G.; Lindon, J. C.; Tranter, G. E.; Koppenaal, D. W. Nuclear Singlet Spin States. Academic Press, 2017; pp 456-462.

(18) Pileio, G. Singlet NMR methodology in two-spin-1/2 systems. *Prog Nucl Magn Reson Spectrosc* **2017**, *98-99*, 1-19.

(19) Pileio, G.; Dumez, J. N.; Pop, I. A.; Hill-Cousins, J. T.; Brown, R. C. Real-space imaging of macroscopic diffusion and slow flow by singlet tagging MRI. *J Magn Reson* **2015**, *252*, 130-134.

(20) Stevanato, G.; Hill-Cousins, J. T.; Håkansson, P.; Roy, S. S.; Brown, L. J.; Brown, R. C.; Pileio, G.; Levitt, M. H. A Nuclear Singlet Lifetime of More than One Hour in Room-Temperature Solution. *Angew Chem Weinheim Bergstr Ger* **2015**, *127* (12), 3811-3814.

(21) Hall, A. M. R.; Cartlidge, T. A. A.; Pileio, G. A temperature-controlled sample shuttle for field-cycling NMR. *J Magn Reson* **2020**, *317*, 106778.

(22) Callaghan, P. T. *Translational dynamics & magnetic resonance*; Oxford University Press, 2011.

(23) Tourell, M. C.; Pop, I. A.; Brown, L. J.; Brown, R. C. D.; Pileio, G. Singlet-assisted diffusion-NMR (SAD-NMR): redefining the limits when measuring tortuosity in porous media. *Phys Chem Chem Phys* **2018**, *20* (20), 13705-13713.

(24) Erriah, B.; Elliott, S. J. Experimental evidence for the role of paramagnetic oxygen concentration on the decay of long-lived nuclear spin order. *RSC Adv* **2019**, *9* (40), 23418-23424.

(25) Erriah, B.; Elliott, S. Experimental evidence for the role of paramagnetic oxygen concentration on the decay of long-lived nuclear spin order. **2019**, *9*, 23418-23424.

(26) Jones, D. K.; Horsfield, M. A.; Simmons, A. Optimal strategies for measuring diffusion in anisotropic systems by magnetic resonance imaging. *Magn Reson Med* **1999**, *42* (3), 515-525.

(27) Melchiorre, G.; Nelder, C.; Brown, L. J.; Dumez, J.-N.; Pileio, G. Single-scan measurements of nuclear spin singlet order decay rates. *Physical Chemistry Chemical Physics* **2021**, *23* (16), 9851-9859.

(28) Grissom, W. A.; Cao, Z.; Does, M. D. |B1+|-selective excitation pulse design using the Shinnar–Le Roux algorithm. **2014**, *242*, 189-196.

(29) Pileio, G. Singlet NMR methodology in two-spin-1/2 systems. **2017**, *98-99*, 1-19.

(30) Swan, I.; Reid, M.; Howe, P. W.; Connell, M. A.; Nilsson, M.; Moore, M. A.; Morris, G. A. Sample convection in liquid-state NMR: why it is always with us, and what we can do about it. *J Magn Reson* **2015**, *252*, 120-129.

(31) Hall, A. M. R.; Cartlidge, T. A. A.; Pileio, G. A temperature-controlled sample shuttle for field-cycling NMR. **2020**, *317*, 106778.

(32) Pileio, G.; Bowen, S.; Laustsen, C.; Tayler, M. C. D.; Hill-Cousins, J. T.; Brown, L. J.; Brown, R. C. D.; Ardenkjaer-Larsen, J. H.; Levitt, M. H. Recycling and Imaging of Nuclear Singlet Hyperpolarization. *Journal of the American Chemical Society* **2013**, *135* (13), 5084-5088.

(33) Xu, H.; Othman, S. F.; Magin, R. L. Monitoring tissue engineering using magnetic resonance imaging. *J Biosci Bioeng* **2008**, *106* (6), 515-527.

(34) Magrofuoco, E.; Flaibani, M.; Giomo, M.; Elvassore, N. Cell culture distribution in a three-dimensional porous scaffold in perfusion bioreactor. **2019**, *146*, 10-19.

(35) Graf, B. W.; Boppart, S. A. Imaging and analysis of three-dimensional cell culture models. *Methods Mol Biol* **2010**, *591*, 211-227.

(36) Bryant, S. J.; Anseth, K. S. The effects of scaffold thickness on tissue engineered cartilage in photocrosslinked poly(ethylene oxide) hydrogels. *Biomaterials* **2001**, *22* (6), 619-626.

(37) Walles, T.; Herden, T.; Haverich, A.; Mertsching, H. Influence of scaffold thickness and scaffold composition on bioartificial graft survival. *Biomaterials* **2003**, *24* (7), 1233-1239.

(38) Rubart, M. Two-photon microscopy of cells and tissue. *Circ Res* **2004**, *95* (12), 1154-1166.

(39) Jaroszewicz, J.; Idaszek, J.; Choinska, E.; Szlazak, K.; Hyc, A.; Osiecka-Iwan, A.; Swieszkowski, W.; Moskalewski, S. Formation of calcium phosphate coatings within polycaprolactone scaffolds by simple, alkaline phosphatase based method. **2019**, *96*, 319-328.

(40) Foltán, R.; Kalbáčová, M. H. MICRO-CT IN TISSUE ENGINEERING SCAFFOLDS DESIGNED FOR BONE REGENERATION : PRINCIPLES AND APPLICATION. 2018.

(41) Shepherd, D. V.; Shepherd, J. H.; Best, S. M.; Cameron, R. E. 3D imaging of cells in scaffolds: direct labelling for micro CT. **2018**, *29* (6), 86.

(42) Park, C.; Choi, H. W.; Lee, C. H.; Lannutti, J. J.; Farson, D. F. Optical scattering in electrospun poly(ε-caprolactone) tissue scaffolds. *Journal of Laser Applications* **2014**, *26* (3), 032004.

(43) Dunn, J. C.; Chan, W. Y.; Cristini, V.; Kim, J. S.; Lowengrub, J.; Singh, S.; Wu, B. M. Analysis of cell growth in three-dimensional scaffolds. *Tissue Eng* **2006**, *12* (4), 705-716.

(44) Liu, Z.; Tamaddon, M.; Gu, Y.; Yu, J.; Xu, N.; Gang, F.; Sun, X.; Liu, C. Cell Seeding Process Experiment and Simulation on Three-Dimensional Polyhedron and Cross-Link Design Scaffolds. *Front Bioeng Biotechnol* **2020**, *8*, 104.

(45) Bancroft, G. N.; Sikavitsas, V. I.; Mikos, A. G. Design of a flow perfusion bioreactor system for bone tissue-engineering applications. *Tissue Eng* **2003**, *9* (3), 549-554.

(46) Radisic, M.; Marsano, A.; Maidhof, R.; Wang, Y.; Vunjak-Novakovic, G. Cardiac tissue engineering using perfusion bioreactor systems. *Nat Protoc* **2008**, *3* (4), 719-738.

(47) Melchels, F. P. W.; Tonnarelli, B.; Olivares, A. L.; Martin, I.; Lacroix, D.; Feijen, J.; Wendt, D. J.; Grijpma, D. W. The influence of the scaffold design on the distribution of adhering cells after perfusion cell seeding. **2011**, *32* (11), 2878-2884.

(48) Brown, D. A.; MacLellan, W. R.; Laks, H.; Dunn, J. C.; Wu, B. M.; Beygui, R. E. Analysis of oxygen transport in a diffusion-limited model of engineered heart tissue. *Biotechnol Bioeng* **2007**, *97* (4), 962-975.

(49) Grayson, W. L.; Bhumiratana, S.; Cannizzaro, C.; Chao, P. H.; Lennon, D. P.; Caplan, A. I.; Vunjak-Novakovic, G. Effects of initial seeding density and fluid perfusion rate on formation of tissue-engineered bone. *Tissue Eng Part A* **2008**, *14* (11), 1809-1820.

(50) Yang, F.; Wolke, J. G. C.; Jansen, J. A. Biomimetic calcium phosphate coating on electrospun poly(ε-caprolactone) scaffolds for bone tissue engineering. *Porous Inorganic Materials for Biomedical Applications* **2008**, *137* (1), 154-161.

(51) Cámara-Torres, M.; Sinha, R.; Mota, C.; Moroni, L. Improving cell distribution on 3D additive manufactured scaffolds through engineered seeding media density and viscosity. **2020**, *101*, 183-195.

(52) Bowers, C. R.; Weitekamp, D. P. Parahydrogen and synthesis allow dramatically enhanced nuclear alignment. *Journal of the American Chemical Society* **1987**, *109* (18), 5541-5542.

(53) Adams, R. W.; Aguilar, J. A.; Atkinson, K. D.; Cowley, M. J.; Elliott, P. I.; Duckett, S. B.; Green, G. G.; Khazal, I. G.; López-Serrano, J.; Williamson, D. C. Reversible interactions with para-hydrogen enhance NMR sensitivity by polarization transfer. *Science* **2009**, *323* (5922), 1708-1711.

(54) Ardenkjaer-Larsen, J. H.; Fridlund, B.; Gram, A.; Hansson, G.; Hansson, L.; Lerche, M. H.; Servin, R.; Thaning, M.; Golman, K. Increase in signal-to-noise ratio of > 10,000 times in liquid-state NMR. *Proc. Natl. Acad. Sci. USA* **2003**, *100* (18), 10158-10163.

(55) Hall, M. G.; Barrick, T. R. Two-step anomalous diffusion tensor imaging. *NMR Biomed* **2012**, *25* (2), 286-294.

(56) Price, W. S. *NMR studies of translational motion*; Cambridge University Press, 2009.